UNIVERSITÀ
DEGLI STUDI
DI BRESCIA

DOTTORATO DI RICERCA IN INGEGNERIA
DELL'INFORMAZIONE

Settore scientifico – disciplinare: ING-INF/07

CICLO
XXXVI

Sensing Strategies of Agri-Food: Advanced Instrumentation for Quality Assurance, Agricultural Enhancement, and Environmental Safety

Dottorando: **Egit Musaev**

Supervisore: **Dr. ssa Camilla Baratto**

Co-supervisore: **Dr. Stefano Farisè** (Oròbix srl)

Contents

List of Figures

Abstract

Questa tesi si occupa di innovazione tecnologica nel settore agroalimentare, integrando sistemi sensoriali all'avanguardia per migliorare la valutazione della qualità degli alimenti, ottimizzare la produzione agricola e potenziare la sicurezza ambientale.

La prima parte di questa ricerca segna un significativo avanzamento nel campo della valutazione della qualità degli alimenti attraverso sensori specificamente progettati per rilevare il deterioramento degli alimenti. Il sensore è a base di cellulosa, mentre la trasmissione dei dati registrati è assicurata grazie all'applicazione di un'antenna Near Field Communication (NFC) accoppiata al sensore. Il sensore così come gli elementi di comunicazione possono essere entrambi direttamente stampati sullo smart-packaging.

Dapprima ho impiegato un sofisticata tecnica di modellazione per quantificare con precisione la resistenza degli elettrodi interdigitati nei Paper Based Gas Sensor (PEGS). Ottimizzando la geometria degli elettrodi, si migliora la sensibilità e la selettività del sensore verso gli ioni NH_4^+, indicativi del deterioramento negli alimenti proteici. Ho inoltre sviluppato per questi sensori un'interfaccia per il monitoraggio in tempo reale all'interno delle confezioni alimentari, utilizzando la tecnologia NFC, che consente una trasmissione dati wireless senza problemi e facilita l'impiego da parte del consumatore. La fattibilità economica di questi PEGS migliorati amplifica ulteriormente il loro impatto potenziale, offrendo una soluzione conveniente nel settore agroalimentare. I sensori sono stati inoltre sottoposti ad una rigorosa validazione empirica, tramite esperimenti con alimenti proteici (pesce) e controllo incrociato con tecniche microbiologiche classiche, confermando la robustezza del modello nel prevedere con precisione il comportamento del sensore in condizioni diverse. L'applicazione di questa tecnologia porterà sensibili vantaggi nella lotta

alla riduzione dello spreco alimentare ed all'inquinamento dovuto all'utilizzo delle materie plastiche in questo settore.

La seconda parte della tesi si concentra sulle applicazioni ambientali di nanofili singoli di Arseniuro di Indio (InAs) come sensori di gas. Questa ricerca ha un approccio più fondamentale, perché permette, tramite di analisi comparativa, di esaminare due nanofili vicini nominalmente identici per individuare le differenze nei loro comportamenti sensoriali. A questo fine ho progettato un sistema di misurazione a due canali, per misurare in modo simultaneo con lo stesso strumento i singoli nanofili di InAs in presenza di inquinanti ambientali come NO_2 e umidità. Un elemento critico di questa ricerca è l'analisi del rumore, che fornisce indicazioni sulle differenze nelle risposte dei nanofili ai due stimoli ambientali considerati. Questa analisi è cruciale per comprendere l'affidabilità e l'accuratezza dei sensori. Esaminando le caratteristiche del rumore e la loro correlazione con le risposte di conduttanza dei due nanofili, si conclude che le differenze osservate nella rivelazione di NO_2 ed umidità relativa sono riconducibili a differenze di fabbricazione non eliminabili (come ad esempio il diametro dei fili o una differenza nei contatti elettrici).

Il terzo progetto segna un significativo avanzamento nell'agricoltura di precisione, introducendo un sistema autonomo di acquisizione dati basato su Long Range Wide Area Network (LoRaWAN) specificamente progettato per monitorare la Root Zone Temperature (RZT) nella coltivazione idroponica del basilico. Questo sistema innovativo affronta le notevoli carenze dei metodi tradizionali di monitoraggio delle serre fornendo una soluzione wireless mobile per una gestione precisa della RZT. Il nucleo del sistema, alimentato da un microcontrollore combinato con il chip LoRaWAN, garantisce un funzionamento affidabile e una comunicazione efficace con le reti LoRaWAN. L'uso della tecnologia LoRaWAN è la chiave, che consente la trasmissione efficiente dei dati su lunghe distanze all'interno di ambienti di serra estesi, facilitando così un monitoraggio dettagliato e accurato delle condizioni idroponiche. L'integrazione del sistema con piattaforme cloud avanzate come Amazon Web Services (AWS) IoT potenzia ulteriormente la sua capacità di analizzare i dati in tempo reale, contribuendo a migliori pratiche agricole e a un maggiore rendimento del basilico.

Collettivamente, questi progetti rappresentano un passo significativo in avanti nella tecnologia agroalimentare, esemplificando il potenziale sinergico dei sistemi sensoriali, della nanotecnologia e della comunicazione wireless per rivoluzionare le pratiche agricole.

Abstract

This thesis deals with technological innovation in the agri-food sector, integrating cutting-edge sensor systems to improve the assessment of food quality, optimize agricultural production, and enhance environmental safety.

The first part of this research marks a significant advancement in the field of food quality assessment through sensors specifically designed to detect food deterioration. The sensor is cellulose-based, while the transmission of recorded data is ensured through the application of a Near Field Communication (NFC) antenna coupled to the sensor. Both the sensor and the communication elements can be directly printed on smart packaging.

Initially, I employed a sophisticated modeling technique to accurately quantify the resistance of interdigitated electrodes in Paper Based Gas Sensors (PEGS). By optimizing the geometry of the electrodes, the sensitivity and selectivity of the sensor towards NH_4^+ ions, indicative of deterioration in protein foods, are improved. I also developed for these sensors an interface for real-time monitoring inside food packages, using NFC technology, which allows for trouble-free wireless data transmission and facilitates use by consumers. The economic feasibility of these improved PEGS further amplifies their potential impact, offering a cost-effective solution in the agri-food sector. The sensors were also subjected to rigorous empirical validation, through experiments with protein foods (fish) and cross-checking with classic microbiological techniques, confirming the robustness of the model in accurately predicting sensor behavior under different conditions. The application of this technology will bring significant benefits in the fight against food waste and pollution due to the use of plastics in this sector.

The second part of the thesis focuses on the environmental applications of single Indium Arsenide (InAs) nanowires as gas sensors. This research takes a more fun-

damental approach, as it allows, through comparative analysis, to examine two nominally identical neighboring nanowires to identify differences in their sensory behaviors. To this end, I designed a dual-channel measurement system to simultaneously measure single InAs nanowires in the presence of environmental pollutants such as NO_2 and humidity with the same instrument. A critical element of this research is noise analysis, which provides insights into the differences in the nanowires' responses to the two considered environmental stimuli. This analysis is crucial for understanding the reliability and accuracy of the sensors. By examining the characteristics of the noise and their correlation with the conductance responses of the two nanowires, it is concluded that the observed differences in detecting NO_2 and relative humidity are due to non-eliminable manufacturing differences (such as wire diameter or a difference in electrical contacts).

The third project marks a significant advancement in precision agriculture, introducing an autonomous data acquisition system based on Long Range Wide Area Network (LoRaWAN) specifically designed to monitor the Root Zone Temperature (RZT) in hydroponic basil cultivation. This innovative system addresses the considerable shortcomings of traditional greenhouse monitoring methods by providing a mobile wireless solution for precise RZT management. The core of the system, powered by a microcontroller combined with the LoRaWAN chip, ensures reliable operation and effective communication with LoRaWAN networks. The use of LoRaWAN technology is key, enabling efficient data transmission over long distances within extensive greenhouse environments, thus facilitating detailed and accurate monitoring of hydroponic conditions. The integration of the system with advanced cloud platforms like Amazon Web Services (AWS) IoT further enhances its capability to analyze data in real-time, contributing to better agricultural practices and a higher yield of basil.

Collectively, these projects represent a significant step forward in agri-food technology, exemplifying the synergistic potential of sensor systems, nanotechnology, and wireless communication to revolutionize agricultural practices.

Acknowledgements

In this brief acknowledgment, I extend my heartfelt gratitude to those who played a pivotal role in steering the work associated with this thesis and provided support during challenging times beyond the academic sphere. Special thanks to my supervisor, Dr. Camilla Baratto, and Prof. Constantino de Angelis, for their invaluable guidance and mentorship. I am appreciative of the Sensori Online lab for their generosity in supplying the PEGS sensors, a crucial component of my research. I am grateful to Dr. Matteo Soprani for his invaluable guidance and support during my first year. My sincere thanks to Dr. Michela Borghetti and Marco Bau' for their assistance in the manufacturing of PCB boards, a key element in my experiments. Additionally, I extend my gratitude to The Scuola Normale Superiore in Pisa for supplying Indium Arsenide nanowire samples and conducting a thorough noise analysis. My thanks also go to CNR-INO Brescia and Antares Vision Company for their financial support of my PhD studies and to the University of Brescia for making laboratory facilities available for my experimental work. I am equally grateful to Orobix company for their provision of electronic components crucial to the root zone temperature measurement project. Finally, I would like to express my profound gratitude to my family and friends, whose unwavering support and encouragement were my pillars of strength during the most trying phases of this journey.

Professional Development and Scholarly Activities

1st year of PhD

21st Geilo Winter School, January 29, 2021

In-depth exploration of explainable algorithms and their practical applications, as presented at the winter school, provided a crucial understanding of how to make complex machine learning models transparent and comprehensible. This knowledge was directly applicable to the use of Amazon SageMaker to analyze temperature data and predict environmental changes in the greenhouse. The school's emphasis on the explainability of neural networks and decision trees informed my approach to developing predictive models with SageMaker, ensuring that the models were not only accurate but also interpretable. This focus on explainability was vital in selecting and implementing machine learning techniques within the AWS suite, particularly SageMaker, enabling the development of reliable and understandable predictive analytics for optimizing plant growth conditions.

NFC RFID Tags Capturing the Essence of Industry 4.0, July 13, 2021

The insights gained from this event were particularly influential in the development of my thesis section on the "Smart Food Quality Control" device. Understanding the versatile applications of NFC technology, including its seamless interaction and energy efficiency capabilities, guided the technical implementation of NFC in my project. This knowledge was crucial in exploring NFC's role in smart packaging for food spoilage detection, demonstrating the technology's potential to enhance system functionality and sustainability.

Huawei University challenge, October 31, 2021

In the 2021 edition of the Huawei Italy University Challenge, I showcased an innovative project, "Smart Food Quality Control," a pioneering device designed to revolutionize the way we monitor food safety. This device leverages advanced sensor technology to accurately measure the spoilage levels of protein-rich foods within packaging, providing a novel approach to ensuring food quality and safety. By integrating seamlessly with smartphones, it offers users a convenient and efficient method to detect spoilage, potentially reducing food waste and enhancing consumer health.

2nd year of PhD

EMRS Conference, Fall 2022

Our research titled *Development of the data acquisition system for sensing food spoilage* was presented at the session on *Modelling and Characterization of Novel Functional Materials for Green Energy, Sensing, and Catalysis Applications* [1]. The authors of this research are Egit Musaev, Matteo Soprani, Emilio Sardini, Costan- tino de Angelis, Edoardo Cantu, Mauro Serpelloni, and Camilla Baratto, affiliated with CNR-INO, PRISM Lab, Via Branze 45, 25123 Brescia, Italy; and the Department of Information Engineering, University of Brescia, 25133 Brescia, Italy. This presentation highlights our contributions to the development of innovative sensing technologies for food safety and preservation.

3rd year of PhD

IEEE Nanotechnology Materials and Devices Conference (NMDC), October 22-25, 2023, Paestum (Salerno), Italy

Our research on InAs nanowires, entitled *Comparative Analysis of InAs Adjacent Nanowire Sensors for Humidity and* NO_2 *Detection*, was presented at the IEEE Nanotechnology Materials and Devices Conference (NMDC) in Paestum (Salerno), Italy, October 22-25, 2023 [2]. The authors of this research, Egit Musaev, Valeria Demontis, Francesco Rossella, Stefano Luin, Valentina Zannier, Lucia Sorba, Guido Faglia, and Camilla Baratto, have contributed to the advancements in the field with this study. This conference, organized by the IEEE Nanotechnology Council (NTC), is focused on the latest research and developments in nanoscience and nanotechnology. Furthermore, we are preparing the article for submission to the *Small Science* journal, with the aim of further disseminate our findings within the scientific community.

Submission to IEEE Sensors Journal

We submitted the article titled *"Paper Sensors for Advanced Smart Packaging: Route to Detection on the Shelf and in Real Ambient"* for review in the IEEE Sensors Journal. The authors, E. Musaev, E. Cantù, M. Soprani, M. Serpelloni (Senior Member, IEEE), E. Sardini (Member IEEE), A. Ponzoni, C. De Angelis (Senior Member IEEE), and C. Baratto* (Member IEEE), have collectively contributed to this work, which highlights the development and application of paper-based sensors in smart packaging. This article encapsulates our research findings on the innovative use of paper sensors for detecting food spoilage, offering a novel approach for real-time monitoring in various storage conditions.

Chapter 1

Introduction

1.1 Motivations

The modern agri-food sector is at a pivotal juncture, balancing the demands of a growing global population with the imperatives of sustainability and safety. Central to navigating this complex landscape is the deployment of advanced sensor systems. These systems, leveraging cutting-edge technology, promise not only to optimize processes but also to revolutionize our understanding and management of food quality, agricultural yield, and environmental safety.

A pressing concern in the agri-food sector is the staggering scale of food waste due to premature disposal. Traditional expiration dates, while necessary, often provide a static and potentially inaccurate representation of food quality. The introduction of cellulose-based gas sensors, designed for real-time monitoring inside food packages, can bridge this gap. By delivering a dynamic feedback loop, these sensors can drastically reduce wastage, ensuring that food items are consumed or discarded based on their actual quality rather than static estimated dates.

Complementing the drive for reduced waste is the pursuit of optimized agricultural yields. Modern agriculture faces a variety of challenges, from ensuring consistent crop yields to adapting to fluctuating environmental conditions. For example, the nexus between root temperature and plant growth speed can offer profound insight into plant health. Dedicated sensor systems, designed to monitor basil root temperatures in greenhouse conditions, pave the way for a granular understanding of plant growth dynamics. By acting on these insights, farmers can potentially enhance crop yields, maximizing every harvest cycle.

Moreover, as our world continues its rapid industrialization, the imperative of monitoring environmental pollutants becomes ever more critical, especially in relation to the agri-food sector. Gases such as NO_2, if unchecked, can deleteriously impact crop health [3, 4] and, consequently, food quality. Measuring relative humidity is crucial in agriculture, as it directly influences the efficiency and sustainability of practices in environments such as greenhouses and storage facilities and is essential to accurately predict and reduce the effects of climate change on agricultural production [5, 6]. InAs nanowires serve as versatile tools, capable of detecting NO_2 and measuring relative humidity. Their integration into agricultural systems possibly enables rapid detection of harmful gases and effective monitoring of humidity levels, thereby safeguarding crop health and ensuring the quality of our food supply. However, in this research, we focused more on the fundamental aspects by investigating two twinning nanowires

In summary, this thesis aims to traverse the multifaceted realm of sensor systems, charting their potential and tangible applications in the agri-food sector. Through meticulous research and innovation, it aspires to offer remedies for some of the industry's most pressing issues, setting the stage for a sustainable, safe, and efficient food future.

1.2 Thesis Outline

Throughout the course of this PhD journey, a series of projects were undertaken, each based on a unique facet of sensor technology and data acquisition systems. The primary contributions from these projects are detailed below.

- **Modeling Capacitance and Resistance of Paper-Based Electrical Gas Sensors (PEGS)**: Adaptation and application of a refined analytical technique [7] to evaluate the capacitance of interdigitated electrodes (IDE) in multilayered structures to model the capacitance of interdigitated sensors within cellulose fiber-based electrical gas sensors for water-soluble gases [8]. This model encapsulates geometric and material parameters along with dielectric permittivity attributes, fostering a robust tool for predicting sensor behavior under varying conditions. Through rigorous empirical validation, the efficacy of the model in enhancing sensor sensitivity and selectivity was established, paving the way for nuanced designs of low-cost gas sensors and contributing to advanced environmental monitoring solutions for food spoilage.

- **Greenhouse Data Acquisition Systems**: Introduced a customized approach to data acquisition in expansive greenhouse settings, uniquely leveraging the strengths of LoRaWAN for long-distance, scalable communication. The integrated MCU and LoRaWAN module streamline the design, reducing potential failure points. Further innovation lies in the methodical bridge between The Things Network (TTN) and Amazon Web Services AWS IoT, ensuring seamless, regionally compatible data transmission and robust system resilience. This approach not only addresses the specific demands of greenhouse environments but also sets a precedent for efficient, scalable, and reliable data acquisition systems in agritech.
- **Advancements in Nanowire Measurement Systems**: Developed a two-channel measurement system tailored for coupled nanowires, effectively addressing challenges related to the intrinsic fragility of InAs NWs. By introducing an integrated current source, signal stability was significantly enhanced, paving the way for meticulous testing with gases like RH and NO_2. Notably, compared to traditional metal oxide nanowires, the NWs showcased efficient NO_2 molecule purging at ambient conditions, underlining their potential for broader applications in chemical species detection.

This PhD thesis is structured into three main chapters, each focused on a distinct project designed to address various challenges in the agrifood sector, as outlined in the preceding section.

- Chapter 2 delves into the development of a data acquisition system for detecting food spoilage, a crucial aspect of quality assurance in the food industry. In this project, we introduced enhancements to sensor design and developed a data acquisition system. These advances serve as a proof-of-concept demonstration of the operational principle of the PEGS.

- In Chapter 3, we present a comparative analysis of individual InAs nanowires, a study with significant implications for environmental safety. The objective of this research is to explore the potential of InAs nanowires as gas sensors and to present a comparative analysis of two adjacent InAs nanowires.

- Chapter 4 introduces a data acquisition system for analyzing root temperature in basil growth, a promising solution for agricultural enhancement. This project seeks to outline a mobile temperature monitoring system within the greenhouse and elucidate the role of LoRaWAN in addressing the challenge of remote data acquisition related to parameters that influence the growth rate of basil plants.

- The thesis concludes with Chapter 5, where potential avenues for future research are discussed.

Chapter 2

Data Acquisition System for Sensing Food Spoilage

2.1 Introduction

In this chapter, we discuss the development of a specialized device designed to monitor the deterioration of protein-rich food items such as fish and chicken. Initially, we elucidate the mathematical model formulated to delineate the relationship between the conductometric parameters and the geometric attributes of interdigitated Paper-Based Electrical Gas sensors (PEGS), a core component of the device. Subsequently, we venture into the experimental phase, shedding light on the refined geometry and its impact on the sensor's responsiveness under humid conditions. We will describe the experimental setup, along with the modern technologies involved, such as near-field communication (NFC), to enhance the ease and versatility of food control. Finally, we describe experiments performed with fish fillets with the aim of exhibiting the efficacy of the newly conceived geometry in tracking spoilage within protein products in a controlled environment.

2.1.1 State of the Art

Smart packaging technologies have been increasingly developed to monitor and control food spoilage, ensuring food safety and quality throughout the supply chain. Various strategies range from traditional colorimetric sensors and time-

Approach	**Fabrication Issues**	**Measurement Complexity**	**Precision**	**Cost**
General Colorimetric Sensors [9, 10, 11, 12]	Easy to Moderate, Sophisticated for Advanced	Simple to High, Multistep for Advanced	Low to High, Trained Manpower for Advanced	Low to Medium, Maintenance for Medium
Time-Temperature Indicators [13, 14, 15]	Low Complexity, Mass Production Compatible	Simple, Consumer Understanding	Questionable Accuracy	Inexpensive
Chemical Monitors [16, 17, 18, 19]	Advanced Equipment Required	Sophisticated Techniques, Trained Personnel	High Sensitivity	High, Maintenance of Setup
Ours	Low Complexity, Mass Production Compatible	Simple, User-Friendly	Medium Sensitivity	Low Cost of the sensor

Table 2.1: Generalized characteristics of various food monitoring approaches

temperature indicators to sophisticated chemical monitors. The synthesis of the technologies is summarized in Table 2.1

Colorimetric sensors in the food industry are devices that use color changes to detect and quantify various substances or changes in food products. They operate on the principle that certain chemicals react with specific analytes in food, causing a visible color change. This change is then used as an indicator of certain conditions or the presence of specific compounds. In practice, these sensors are used for a variety of applications, such as monitoring food freshness, detecting spoilage, and identifying contaminants [20]. For example, they can detect gases emitted by spoiling food, changes in pH indicating spoilage, or the presence of harmful bacteria. This technology offers a quick, easy-to-use, and often non-destructive means of ensuring food quality and safety. However, they come with a series of disadvantages: The complexity of the process is one such drawback, where colorimetric methods are time-consuming, complicated, and often involve multistep processes that can be laborious and costly. They also require the use of sophisticated instruments and the maintenance of certain critical conditions, all of which require analysis by trained manpower[9]. Fabrication and reliability issues present another challenge. Despite the development of numerous colorimetric food sensors, few fulfill all the criteria regarding simple production, excellent sensitivity, and dependable reliability. This becomes especially critical when these sensors are exposed to spoiled food, which requires a reliable detection method to ensure food safety [10]. The constraints of machine vision in colorimetric sensor systems are a challenge, particularly in food-related scenarios such as assessing food quality and categorizing food items., and progress related to food poisoning. Although the specifics of the disadvantages were not detailed, it is suggested that there may be limitations associated with machine vision in colorimetric sensing systems[11]. Lastly, the preparation and functionalization of colorimetric sensors can be complex and may require accurate manipulation of the dimensions, shape, and surface chemistry, which can be challenging and cost-intensive [12].

Time-temperature indicators (TTIs) are used in the food industry to monitor food spoilage by tracking Monitoring the thermal past and predicting the remaining shelf life of perishable items during their storage, transportation, and use is accomplished through the permanent alteration in color caused by the combined impacts of time and temperature. [13]. TTIs play a vital role because temperature significantly affects the shelf life of food products. Variations in the temperature profile can result in the proliferation or survival of microorganisms, ultimately leading to spoilage. Additionally, improper freezing can cause protein denaturation in meat and other products [14]. TTIs provide a quantifiable visible response dependent on time-temperature like alterations in color or physical distortion, in line with standards for food quality and indirectly indicating the quality of the product [15]. However, TTIs come with a set of disadvantages. Even though these are basic and cost-effective devices that are affixed to the package to verify if the cold chain or necessary temperature is maintained correctly throughout supply chain of food, their precision may be uncertain. Color changes or mechanical deformations that they exhibit as indicators of spoilage depend on the cumulative effects of time and temperature, which may not always accurately reflect the real-time microbial conditions of the food. Furthermore, TTIs may not provide a comprehensive picture of food quality, especially if other factors, in addition to temperature, also contribute to spoilage. There is also concern about the understanding and interpretation of consumers of TTIs, which, if misunderstood, could lead to the consumption of spoiled food [14].

Chemical monitors are employed in the food industry to detect food spoilage by analyzing chemical alterations such as oxidation and lipolysis, which are indicative of food degradation[16]. However, they present several challenges. The complexity of the technology used, which often involves sophisticated spectroscopic techniques, requires a well-maintained setup and trained personnel for effective operation[16]. The sensitivity required for accurate detection can lead to the need for advanced, often expensive, equipment [17]. Although recent advances have led to the development of miniaturized wireless sensors capable of monitoring in real time volatile biogenic amines indicative of spoilage, standard laboratory tests for spoilage are not performed regularly, indicating a gap in routine monitoring [18]. Furthermore, the material and technology used, such as polymer-based gas sensors to detect meat spoilage by monitoring early stage volatile organic compound emissions, although fast and effective, depend on the maintenance of the sensing material and technological setup, which can be costly and require a certain level of expertise [19].

2.1.2 Novel Contributions

One of the novel approaches in our project lies in the utilization of Aerosol Jet Printing (AJP) for the fabrication of PEGS. The innovation of this method is twofold: first, in the choice of a moisture-retaining substrate, enhancing sensor functionality; and second, in the fine-tuning of the AJP process parameters to optimize the geometric precision of IDEs without compromising the substrate integrity. This approach, particularly the use of photonic sintering for ink curing, marks a significant advancement in the fabrication of PEGS, addressing common challenges such as oxidation and contamination, and paves the way for more efficient and cost-effective sensor manufacturing [21, 22, 23].

Another innovative aspect of our project is the integration of NFC technology within the PEGS system. This strategic choice is grounded in the widespread presence of NFC technology in modern mobile devices, making the technology highly accessible to consumers and businesses. The novelty of using NFC lies not only in its versatility, which allows for a broad spectrum of interactive capabilities, but also in its ability to power the device passively, thus eliminating the need for batteries. This battery-free operation is a significant step towards sustainability, aligning with eco-friendly practices by reducing waste associated with battery disposal. Furthermore, the self-sustaining nature of NFC-powered devices represents a breakthrough in the realm of smart packaging. It reduces the environmental footprint and resonates strongly with the growing segment of eco-conscious consumers. By employing NFC's dual capabilities of communication and power provision in our design, we have adapted an existing technology to create a unique and fitting solution for our PEGS system. This integration improves usability and contributes to the environmental sustainability of our sensors, showcasing how established technologies such as NFC can be applied innovatively in specific projects to achieve novel outcomes [24].

The challenges addressed in this chapter are twofold. First, we tackle the optimal selection of the sensor's geometric dimensions. Second, we refine the sensor signal digitization process, simplifying spoilage tracking for both consumers and vendors. Although the sensor's initial design has previously been established, this work pioneers the optimization of the PEGS geometry through conformal mapping techniques [7]. Furthermore, the practicality of the technology in tracking food spoilage has been substantiated through experiments with food samples, complemented by parallel microbiological analyses. These coordinated studies may confirm the effectiveness of the sensor in real-world applications.

In summary, the content of this chapter not only builds upon the preliminary designs but also introduces an application of conformal mapping techniques to optimize sensor geometry, coupled with the integration of a commercially viable NFC interface. These advances collectively contribute to a more sustainable, cost-effective, and user-friendly solution for food spoilage detection, marking a significant leap forward in the field of smart packaging and sustainable technology.

2.2 Impedance Characteristics and Geometrical Parameter Dependencies of Paper-Based Electrical Gas sensors

In this section, the focus is on developing a mathematical model for PEGS, with an emphasis on refining their geometrical configuration to improve the responsiveness of PEGS. Although modeling of capacitance and resistance for interdigitated sensors follows established methodologies, the unique aspects of PEGS necessitate a tailored approach. We will systematically apply conformal mapping techniques to elucidate the intricate relationship between the PEGS geometry and its electrical properties. This rigorous analysis is essential to advance the design and functionality of PEGS in practical applications.

2.2.1 Dependencies of the Capacitive Properties on Geometrical Parameters

In this subsection, we examine the capacitive properties in relation to the geometrical parameters of the PEGS. As illustrated in Figure 2.1, the sensor under discussion is an IDE array made of carbon deposited on a paper substrate [8], a configuration widely recognized for its utility in sensing applications [25, 26, 27]. Figure 2.1a illustrates the design of the electrode plane, together with an illustrative depiction of the callout of its two fingers (Figure 2.1b) with the representation of the width of the finger w and the gap between the fingers g.

The vertical cross-section of the sensor, as shown in Figure 2.1c, is particularly informative, providing a clear view of the capacitive structure of the sensor. With six fingers incorporated into the design, there are effectively ten capacitance values [28] for each of the two layers: one being air and the other consisting of electrolyte impregnated paper (EIP).

An electrolyte, in the context of this sensor configuration, refers to a substance containing free ions that makes it electrically conductive. In our specific setup, the electrolyte is integrated within the paper substrate, which aids in the conductive properties of the PEGS. This electrolyte typically consists of various salts, acids,

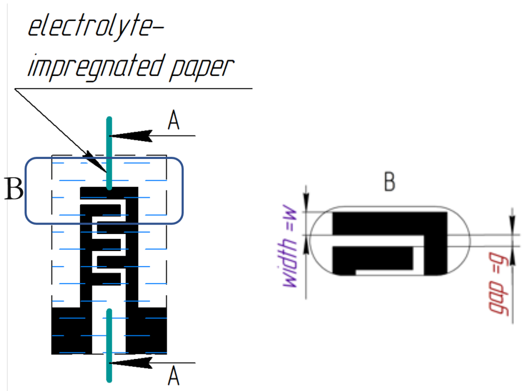

(a) PEGS layout (b) Fingers call-out

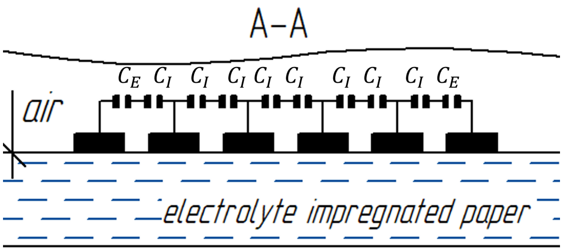

(c) Fingers cross-section. The capacities indexes represent the location of the electrodes (E - exterior and I – interior)

Figure 2.1: Interdigitated sensor layout

or bases dissolved in a suitable solvent such as water. When impregnated onto the paper substrate, the electrolyte allows for efficient transfer of electrical charge between the interdigitated electrodes, significantly enhancing the sensor's ability to detect and measure changes in capacitance and resistance as a result of multiple environmental influences.

Utilizing network analysis for assessing the equivalent circuit [28] of the PEGS shown in Figure 2.1c, the overall capacitance between the negative and positive terminals of a single layer can be determined. This total capacitance, denoted as C_{total}, is given by the formula:

$$C_{\text{total}} = (N-3) \cdot \frac{C_{\text{I}}}{2} + 2 \cdot \frac{C_{\text{I}} C_{\text{E}}}{C_{\text{I}} + C_{\text{E}}}, \tag{2.1}$$

where N represents the number of fingers, and it is assumed that $N > 3$. In this expression, C_{I} and C_{E} stand for the individual capacitances of the interdigitated and external electrodes, respectively.

The determination of the total capacitance of PEGS in this research is based on the application of the results of conformal mapping techniques, as detailed in [7]. The foundational principle of these techniques lies in transforming the sensor's capacitive geometry into an equivalent model of a parallel plate capacitor. This transformation facilitates the use of known values for capacitance, as well as established mappings of equipotential and electric field lines, thus providing a reliable basis for our calculations.

The capacitance, which is dependent on the electrode positioning, can be quantified through a formula that accounts for contributions from both the air layer and the EIP layer. This relationship is mathematically represented as follows:

$$C_X = C_{X,\mathrm{air}} + C_{X,\mathrm{eip}} = \varepsilon_0 L \left(\varepsilon_{\mathrm{air}} \frac{K(k_{X\infty})}{K(k'_{X\infty})} + \varepsilon_{\mathrm{eip}} \frac{K(k_{X,\mathrm{eip}})}{K(k'_{X,\mathrm{eip}})} \right), \tag{2.2}$$

where ε_0 is the permittivity of free space, and $\varepsilon_{\mathrm{air}}$ and $\varepsilon_{\mathrm{eip}}$ are the relative permittivities of air and EIP, respectively, L – length of the fingers . In this formulation, $K(k)$ represents the complete elliptic integral of the first kind with modulus k. The modulus k is influenced by the shape parameters, specifically the gap between the fingers g and the width of the fingers w, as detailed in [28]. The subscript X in the formula signifies the location of the electrodes, with E for exterior and I for interior, while the second subscript denotes the layer type – either air or EIP. The term $k' = \sqrt{1 - k^2}$ represents the complementary modulus.

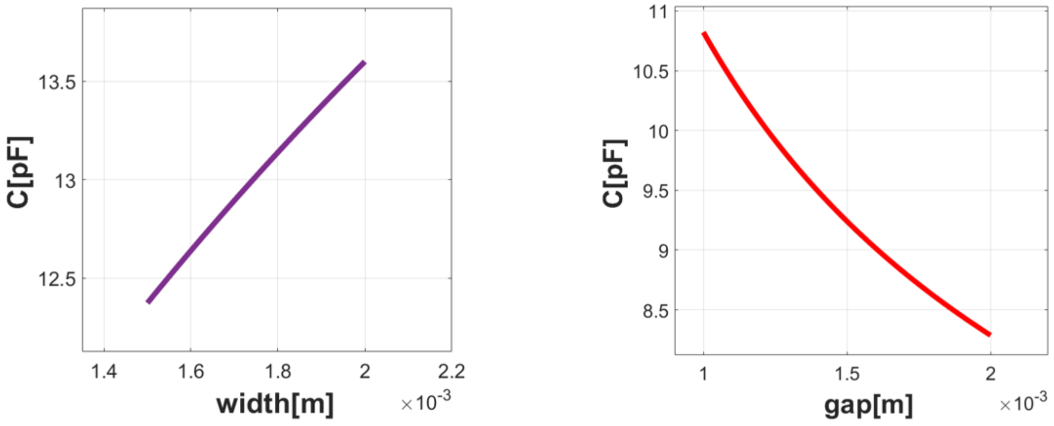

(a) $N = 6$, $g = 10^{-3}$ m, $L = 0.01$ m, $\varepsilon_{\mathrm{eip}} = 2.5 \times 10^{-12}$ F/m

(b) $N = 6$, $w = 1.5 \times 10^{-3}$ m, $L = 0.01$ m, $\varepsilon_{\mathrm{eip}} = 2.5 \times 10^{-12}$ F/m

Figure 2.2: Simulated capacitive response to variations in electrode width and gap

Furthermore, the empirical validation of the theoretical model is facilitated through simulation. Figure 2.2 illustrates the simulated impact of varying the geometrical parameters, that is, the gap between the electrodes and their width, on the overall capacitance of the PEGS. The specifics of the simulation parameters, including the permittivity values adopted from [29], are detailed within the figure captions. These simulations serve to corroborate the analytical expressions by demonstrating how alterations in the physical dimensions of the sensor influence its capacitive properties.

Figure 2.2a demonstrates the simulated relationship between the width of the electrodes and the capacitance of the EIP. The simulation plots the capacitance as the width of the PEGS fingers is varied from 1.5 to 2 mm. Despite the appearance of linearity in the plot, this is a result of the scale; the underlying relationship is governed by complex, nonlinear formulas based on the physical and electrical properties of the system, as described by the equations provided. This trend suggests that the electrode width is positively correlated with the capacitance, implying that wider electrodes can store more electric charge. This phenomenon can be ascribed to the greater surface area accessible for the accumulation of charge, which is a fundamental feature of capacitors.

Figure 2.2b illustrates the simulated effect of the electrode gap on the capacitance of the EIP. The graph shows a decrease in capacitance as the gap between the PEGS fingers widens from 1 mm to 2 mm. This inverse relationship suggests that a larger gap increases the effective distance between the plates for charge storage and, consequently, decreases the capacitance. The calculations take into account the material characteristics and the geometric configuration of the PEGS. The trend observed in Figure 2.2b confirms the expected theoretical model and highlights the influence of electrode spacing on the sensor's electrical characteristics.

The simulations conducted have indicated that the capacitance of the PEGS exhibits limited variation in response to changes in the geometrical parameters of the electrodes. Specifically, the change in capacitance is confined within a narrow range of 12.2 pF to 13.7 pF for alterations in width and a range of 8.5 pF to 11 pF for modifications in the gap. These subtle variations suggest that the capacitive properties of the sensor are relatively insensitive to geometrical changes within the ranges explored. Given these marginal differences, our research will pivot towards examining the resistive properties of the PEGS. These properties have demonstrated a more significant and responsive change to variations in both the gap and the width. The resistive aspect of sensor performance, therefore, promises a more fruitful avenue for optimization in practical applications. This shift in focus aligns with the aim of enhancing PEGS sensitivity and accuracy, which will be explored in the following subsection.

2.2.2 Dependencies of the Resistive Properties on Geometrical Parameters

To further our investigation of the resistive properties of the PEGS and its dependence on its geometric configuration, we revisit the configuration of the interdigitated sensor as shown in Figure 2.3a. The equivalent circuit model represented in Figure 2.3b has been extended to include the lead resistances in series with the intrinsic impedance of the PEGS. This model serves as the foundation for analyzing how geometric alterations impact the resistive behavior of the sensor and its overall performance.

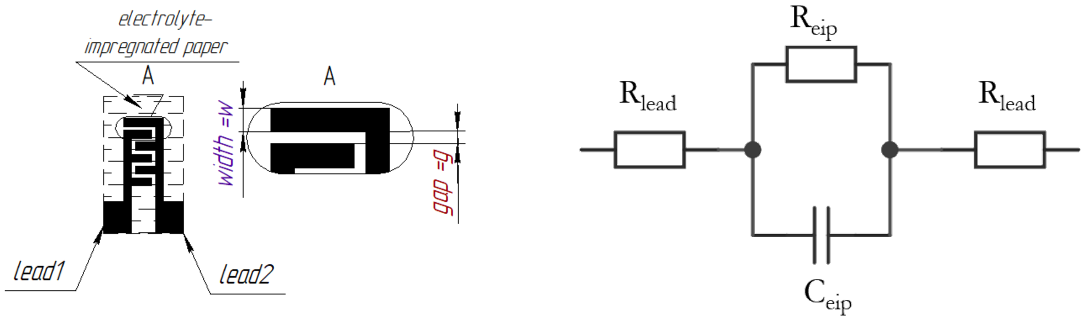

(a) Layout of the interdigitated impedance device

(b) Simplified electrical diagram of the interdigitated impedance device

Figure 2.3: Interdigitated sensor layout and its equivalent circuit

This intrinsic impedance is characterized by a parallel arrangement of the EIP resistance R_{eip} and capacitance C_{eip}, attributed to the interaction between the paper substrate and the liquid solution under test. Notably, the lead resistance, denoted as R_{lead}, aggregates the resistive contributions of the connecting wires and electrical leads. Given that these wires and leads are composed of materials with high conductivity, their resistive effect is negligible, thus allowing them to be excluded from the computational model to simplify the analysis without compromising accuracy.

The resistance R_{eip} depends on the conductivity of the electrolyte σ_{eip} and the cell constant K_{cell}. This relationship is expressed by the equation below [30]:

$$R_{\text{eip}} = \frac{K_{\text{cell}}}{\sigma_{\text{eip}}} \tag{2.3}$$

Given the sensor parameters, namely the length of the electrodes L, the number of fingers N, the gap between electrodes g, and the width of the electrode fingers w, the cell constant K_{cell} can be calculated as follows[30]:

$$K_{\text{cell}} = \frac{2}{(N-1)\cdot L} \cdot \frac{K(k)}{K(\sqrt{1-k^2})} \tag{2.4}$$

In this expression, $K(k)$ denotes the complete elliptic integral of the first kind with modulus k, defined by the equation:

$$K(k) = \int_0^1 \frac{dt}{\sqrt{(1-t^2)(1-k^2t^2)}} \tag{2.5}$$

The modulus k, which is crucial in characterizing the sensor's electrode geometry, is expressed as follows for configurations with more than two sensor fingers [31]:

$$k = \cos\left(\frac{\pi}{2} \cdot \frac{w}{w+g}\right) \tag{2.6}$$

In summary, the overall resistance of the PEGS is primarily determined by the EIP resistance, which depends on the sensor's geometric configuration and the conductivity of the EIP. By fine-tuning the geometric configuration – specifically, the electrode gap g and width w – we can optimize the PEGS resistive response. Figure 2.4 shows the simulated effects of varying the electrode gap and width on the PEGS resistance. Water was chosen as the electrolyte for simulation purposes because of its predictable properties and the ease of creating a controlled environment for subsequent experimental verification. These simulations serve as a precursor to the experimental phase, which aims to confirm the optimal sensor geometry predicted.

Figure 2.4a illustrates the simulated relationship between the width of the elec-

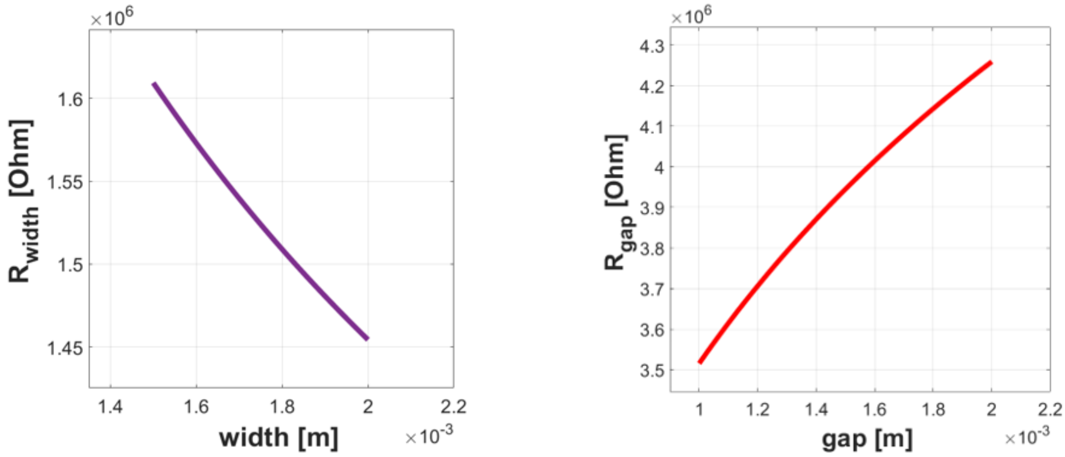

(a) $N = 6$, $g = 10^{-3}$ m, $L = 0.01$ m, $\sigma_{\text{eip}} = 2.15 \times 10^{-5}$ S/m

(b) $N = 6$, $w = 1.5 \times 10^{-3}$ m, $L = 0.01$ m, $\sigma_{\text{eip}} = 2.15 \times 10^{-5}$ S/m

Figure 2.4: Simulated resistive response to variations in electrode width and gap

trodes and the resistance of the EIP. The simulation parameters are mentioned in the caption. As the width of the sensor fingers increases from approximately 1.5 to 2 mm, the plot indicates a decrease in resistance. This change is not directly proportional, reflecting the nuanced physical and electrical interplays dictated by the PEGS geometry and the electrical properties of the materials involved. Resistance is calculated on the basis of the cell constant and conductivity, which are influenced by the width and geometry of the fingers.

Similarly, Figure 2.4b shows the simulated correlation between the gap between the electrodes and the EIP resistance. The plot shows a positive correlation, where resistance increases as the gap between the sensor fingers widens. This relationship is exhibited over a gap range from 1 to 2 mm. The upward trend suggests that the resistance of the PEGS is sensitive to changes in the gap, possibly as a result of the increased distance for charge carriers to traverse between electrodes. The resistance is influenced by both the physical separation of the electrodes and the electrical characteristics of the medium, in this case the EIP. As in the previous simulation, the resistance is a function of the cell constant and the conductivity, with the gap directly affects the cell constant in this configuration.

Drawing on these insights, it becomes evident that sensor performance can be optimized through careful design adjustments. According to the simulated results, for a better resistive relative response, an effective approach would be to refine the PEGS layout. Specifically, reducing the width of the fingers and increasing the gap between them emerges as a favorable design strategy. This conclusion is visually represented in Figure 2.5, which contrasts the original sensor layout with the newly proposed design, highlighting the modifications that are predicted to enhance the resistive response of the sensor.

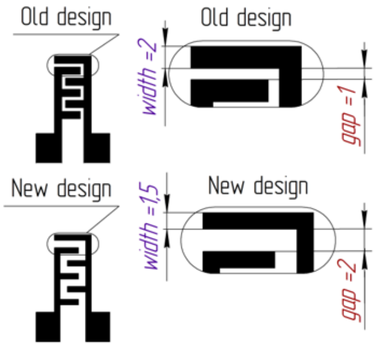

Figure 2.5: Comparative layout of the original and optimized PEGS designs

The relative resistance response due to design modifications can be quantitatively expressed as:

$$\Delta R_{\mathrm{rel}}(sim) = \frac{R_{\mathrm{new}} - R_{\mathrm{old}}}{R_{\mathrm{old}}} \times 100\% = 30.1\% \tag{2.7}$$

where R_{new} and R_{old} are the resistances of the PEGS after and before the design changes, respectively. The subscript rel denotes the relative change, and sim indicates that these values are obtained from simulation.

Based on these calculations, we expect that experiments comparing the new and old sensor designs will show about a 30.1% increase in resistance performance. This estimate assumes that the conditions of the experiment will match the simulation settings. If the experiments give results close to this prediction, it will confirm the accuracy of our simulation and the benefits of the design changes we made.

2.3 Materials and Methods

To validate the simulation outcomes, it is essential to create the sensor and develop a tool for assessing its resistance..

2.3.1 Introduction to Paper-Based Electrical Gas Sensors Manufacturing

The field of PEGS manufacturing encompasses a variety of fabrication techniques, each with its unique advantages and limitations. These include wax printing [32], which is valued for its simplicity, but is limited by the lower resolution and instability at higher temperatures. Photolithography [33] offers high-resolution capabilities, yet is flawed in its complexity and cost, making it less viable for quick and economical sensor production. Similarly, Polydimethyl-Siloxane (PDMS) [34] printing, while flexible, struggles to achieve high-resolution results and requires modifications of specialized printing equipment. These methods, despite their individual merits, present certain limitations that make them less suitable for projects demanding precision, scalability, and efficiency in sensor fabrication. For our specific project needs, these methods are not entirely suitable due to limitations in precision, scalability, or complexity.

In the previous approach to the manufacture of PEGS , a method was used using a cutter plotter and a ballpoint pen , as elucidated in [8]. This technique provided a straightforward and environmentally friendly means of printing carbon electrodes onto cellulose paper. Although it enabled easy prototyping and the creation of basic sensor designs, this method was limited by its lack of fineness and scalability, making it less suitable for the development of more complex and advanced sensor applications. AJP, in contrast, excels in precision and versatility. This advanced technology, which is capable of printing intricate and consistent patterns, allows digital adjustment of parameters like electrode surface area and ink deposition, which is crucial for enhancing sensor sensitivity and specificity. The AJP process, which involves controlled toolpaths and optimized process parameters, ensures uniformity and repeatability in sensor fabrication, making it an ideal choice for producing high-quality scalable PEGS.

In summary, while the various methods discussed offer insight into the broad potential of paper-based sensor fabrication, for our project's goals, focusing on high sensitivity, precision, and scalability, AJP emerges as the most suitable technology, addressing the limitations of other methods and aligning with the demands of advanced PEGS applications.

2.3.2 Paper Electrical Gas Sensors Fabrication Process

In our project, the manufacturing of PEGS was carried out using an aerosol jet printer [21, 22]. The fabrication process was carried out with the Sensori Online group of the University of Brescia. It was chosen Whatman™ chromatography 1 cellulose paper as the substrate, which is known for its high purity and minimal chemical additives [23]. The hygroscopic nature of this paper ensures that the cellulose fibers retain a significant amount of moisture, which is beneficial for sensor functionality. The carbon ink EXP 2652-28 was used to create the electrodes, preferred for its cost-effectiveness and suitable properties in moisture-rich environments such as food packaging. This choice was critical in avoiding issues such as oxidation and contamination, which are more common with other conductive inks, such as silver. For the production of PEGS, the research team employed an Optomec AJ300 printer. They meticulously designed specific toolpaths to print carbon IDEs, ensuring precise overlap in each run. Process parameters, such as sheath, atomizer, and exhaust gas flows, were carefully set to achieve the desired geometrical finishes. The printer plate temperature was maintained at 50 °C, and the printing speed was regulated at 4 mm/s across three runs, resulting in a total of 50 sensors, produced in batches of ten. To optimize the sintering process without damaging the paper substrate, they used photonic sintering (Pulseforge 1300 - Novacentrix), applying a single pulse at 250 V for 1750 µs. This methodical approach led to the successful fabrication of PEGS with precise specifications and layouts (Figure 2.6).

2.3.3 Board Components Selection

Resistance Measuring Device Selection

To validate the performance of the fabricated PEGS, it is imperative to develop a reliable and accurate resistance measurement system. Traditional methods for resistance measurement, including direct current measurement techniques [35] and Wheatstone Bridge configurations [36], offer certain benefits but also possess lim-

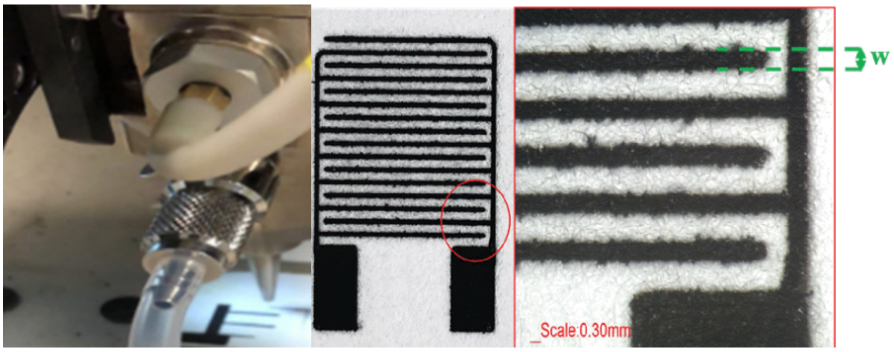

Figure 2.6: AJP printing an intial design (left); a produced sensor in its ultimate design (right)

itations in terms of resolution, noise susceptibility, and complexity for integration into compact sensor systems.

In this project, we have chosen to implement an Analog-to-Digital Converter (ADC) for the resistance measurement of our paper gas sensors. This decision is based on several key advantages that ADC offers, which are particularly aligned with the requirements of our application [37].

ADCs are known for their high resolution and accuracy. This characteristic is essential to detect small changes in resistance, which are indicative of the presence of gas. Such high-resolution output is crucial in gas sensor applications where the precise detection of gas concentrations is needed. The enhanced noise immunity of ADCs, afforded by their oversampling and noise-shaping features, is another significant advantage. This capability ensures reliable sensor readings, particularly in environments with high electrical noise, a common challenge in field applications. Additionally, the low power consumption of ADCs is a vital attribute, aligning well with the requirements of portable and battery-operated gas sensing systems. This feature enables the development of sensors that are not only efficient, but also suitable for long-term field deployment without frequent power replenishments. Furthermore, the ease of integration offered by these ADCs into microcontroller-based systems facilitates compact and efficient board design. This aspect is of paramount importance in modern sensor technology, where miniaturization and integration are key factors.

Finally, the wide dynamic range of ADCs complements the variable nature of the gas sensor resistance in response to different gas concentrations. The ability to handle a broad range of resistance values without compromising accuracy or resolution is particularly beneficial for gas sensors, as it ensures a consistent and reliable response across various detection scenarios. Thus, the ADC emerges as a superior choice for this application, addressing the need for precision, miniaturization, and efficiency in the resistance measurement of PEGS. This approach not only complements the advanced fabrication techniques employed in sensor production, but also ensures high fidelity in sensor response analysis, which is crucial for the development of reliable and sensitive gas detection systems.

Microcontroller Family Selection

The selection of a microcontroller family is a pivotal decision in the design of any advanced sensor system. This decision impacts not only the performance and efficiency of the system, but also its scalability and adaptability to diverse applications. For our sensor system, the STM32 microcontroller was chosen after a thorough comparison with other popular microcontrollers, including the Arduino, PIC, and Atmel AVR series.

The Arduino series, widely acclaimed for its user-friendly interface and extensive community support, is short in terms of processing power and flexibility compared to the STM32 [38]. While suitable for basic applications and prototyping, Arduino microcontrollers often lack the necessary computational capabilities and advanced integrated peripherals required for complex sensor systems.

Similarly, PIC microcontrollers, known for their simplicity and cost-effectiveness, are limited by their lower processing speeds and less sophisticated ADCs [39]. This makes them less suitable for applications that demand high-speed data processing and precision, such as in our gas sensor system with a sigma-delta ADC.

Atmel AVR microcontrollers, although comparable to STM32 in terms of processing capabilities, often have higher power consumption and a more limited range of integrated peripherals [40]. This can lead to increased system complexity and reduced energy efficiency, particularly in portable or battery-operated applications.

On the contrary, the STM32 microcontroller offers several advantages over these alternatives. It boasts a high-performance ARM Cortex-M core, offering superior computational capability crucial for precise and fast data processing [41]. The wide range of integrated peripherals, including advanced ADCs and communication interfaces, simplifies board design and enhances system reliability [41]. Furthermore, its low power consumption is essential for long-lasting, energy-efficient sensor applications [42].

Additionally, the STM32 is supported by an extensive software ecosystem, which facilitates the development process, particularly for complex algorithm implementations [43]. Its scalability, with a wide range of variants, ensures flexibility and adaptability to specific project needs.

In conclusion, the STM32 microcontroller emerges as the most suitable choice for our gas sensor system. Its balance of processing power, energy efficiency, peripheral integration, complex ADCs, software support, and scalability distinctly outperforms those of Arduino, PIC, and Atmel AVR microcontrollers in meeting the specific requirements of our application.

2.3.4 Board Schematic Description

Buffer Integration for ADC Optimization in Resistance Measurement

A pivotal aspect of this development is the integration of various components, notably the measuring devices and the microcontroller unit. A significant design element in this context is the incorporation of a buffer. The primary role of this buffer is to address the interaction between the high resistance inherent in the voltage divider setup and the input characteristics of the ADC. In systems using a voltage divider for resistance measurement, the high resistance can adversely affect the ADC's performance because of its input impedance. By including an operational amplifier with a low input bias current, the circuit minimizes the loading effect on the voltage divider, ensuring that the voltage fed to the ADC remains accurate and stable.

The AD8615 operational amplifier was chosen for the PCB design primarily due to its suitability for high-precision resistance measurement in electronic systems [44]. Its low offset voltage (typically 80 µV, max 300 µV) is crucial for minimizing measurement errors (Figure 2.7). The amplifier's single-supply operation within 2.7 V to 5 V range simplifies the power supply design. It also features a low noise level (8 nV/Hz) and a wide bandwidth (20 MHz), ensuring signal stability and fi-

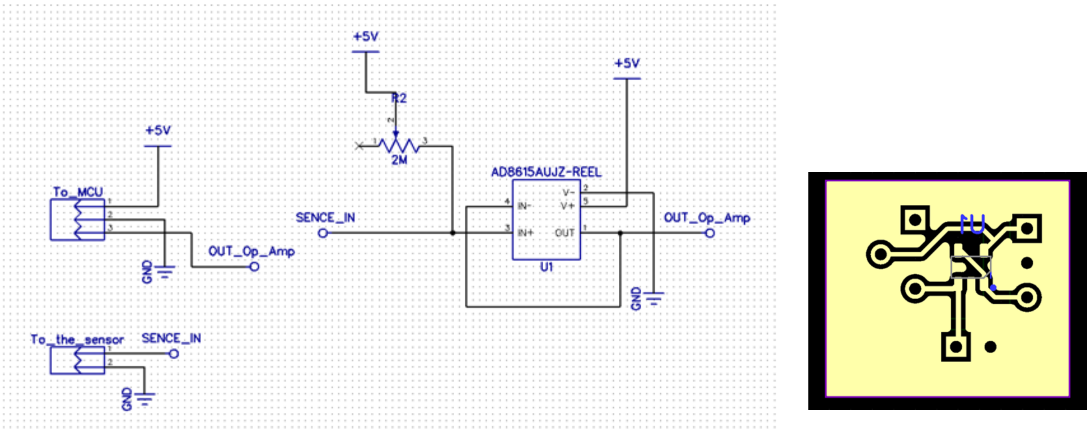

(a) AD8615 schematic view

(b) AD8615 layout view

Figure 2.7: AD8615 in the buffer scheme

delity across a range of frequencies. The AD8615's capability for rail-to-rail input and output maximizes the dynamic range of the ADC, enhancing measurement accuracy. In addition, its low input bias currents and a fast slew rate (12 V/µs) contribute to the precision and responsiveness of the circuit. Moreover, a reference resistor has been added to the amplifier's input, laying the groundwork for future resistance measurements of PEGS using a voltage divider setup. This addition further refines the circuit's ability to accurately measure resistance, demonstrating a thoughtful approach to design that anticipates and accommodates future experimental requirements.

Microcontroller Selection in Resistance Measurement Systems

Next stage is to select the concrete MCU among the STM32 MCU family. When selecting an MCU for a resistance measurement system, several characteristics are of paramount importance. First, ease of programming is crucial, as it directly impacts development time and efficiency. An MCU that offers a user-friendly programming environment can significantly accelerate project development, especially during the prototyping phase.

Another critical factor is the ability to test the system without the need to develop a new board. This requirement calls for an MCU that can be integrated into existing development boards or platforms, facilitating immediate testing and iteration. Such integration not only saves time, but also reduces the resources required for the development process.

Furthermore, compatibility with Near Field Communication (NFC) technology is essential. NFC capabilities enable the system to communicate wirelessly, expanding its potential applications and making it more versatile in various operating environments.

Taking into account these key characteristics, the microcontroller unit selected for the resistance measurement system is the STM32L053R8 and its dedicated development board Nucleo L053R8 (Figure 2.8).

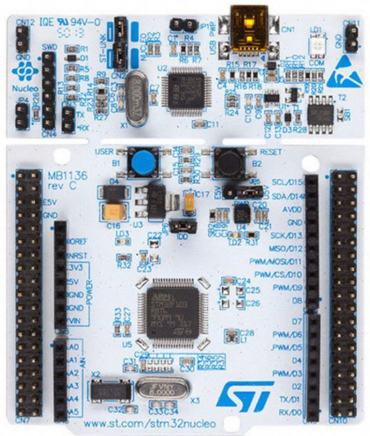

Figure 2.8: Photoimage of STM32 Nucleo L053R8

This MCU aligns well with the specified requirements. It is known for its ease of programming since it can be used in both the Arduino and Mbed environment [45], a vital feature that streamlines the development process. The Nucleo L053R8 can be utilized with existing development platforms, eliminating the need for a custom board for initial testing and development. Moreover, its direct hardware and software compatibility with NFC modules [46] adds a significant dimension of wireless communication and battery-less powering abilities to the system. The Nucleo L053R8, with these attributes, is an ideal choice, meeting all the necessary criteria for efficient and versatile operation in a resistance measurement system.

Integrating the Sensor for Ambient Control in PCB Design

When designing a PCB for resistance measurement, controlling the ambient temperature and humidity is crucial to achieve accurate results. The system requires a sensor that can operate in a wide range of environmental conditions, maintain high accuracy, and integrate seamlessly with the chosen MCU. The SHT33-DIS sensor meets these requirements with its broad operating range (-40 to 125°C, 0 to 100% RH), high accuracy (±2.0% RH, ±0.48 °C), and low drift [47]. Its certification to the ISO 17025:2017 standards ensures reliability and precision, crucial for sensitive measurements.

Additionally, the SHT33-DIS's compatibility with I2C communication allows for easy integration with the STM32 NucleoL053R8 MCU used in the PCB. This integration is vital for real-time monitoring and control of ambient conditions within the experimental setup. The compact size and flexibility of the SHT33-DIS, along with its robustness certification in various environments, render it a perfect selection for this particular use. The decision to incorporate SHT33-DIS into the custom developed PCB (Figure 2.9) aligns with the project's need for precise environmental control in resistance measurement experiments.

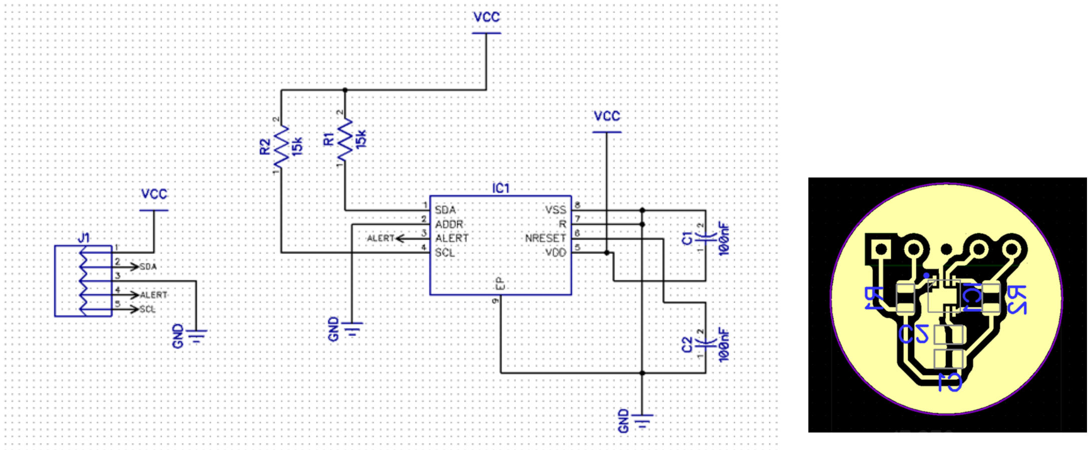

(a) SHT33-DIS schematic view

(b) SHT33-DIS layout view

Figure 2.9: SHT33-DIS PCB board design

2.3.5 Processing of ADC Readings in STM32 MCU

This code snippet is designed to process ADC readings in a microcontroller environment, to filter out noise, and obtain a more stable reading from the PEGS. Here is a breakdown of its functionality:

- **Nested Loops for Data Collection:** The code uses two nested loops. The outer loop iterates six times, probably for six different sensors or ADC channels. The inner loop collects several readings from each sensor.

- **Reading ADC Values:** Within the inner loop, a 16-bit unsigned integer from each sensor is read and stored in a two-dimensional array.
- **Finding Minimum and Maximum Values:** For each reading, the code checks if the current value is the new maximum or minimum for that sensor and updates accordingly.
- **Summing up the Readings:** Each sensor's reading is added to a cumulative sum.
- **Time Delay:** A 100-microsecond delay is introduced between each reading.
- **Pseudomedian Filtering:** After collecting all readings, a 'pseudomedian' value for each sensor is calculated by subtracting the minimum and maximum values from the sum and then dividing by the number of iterations minus 2.

The following is the code snippet used for this process:

Listing 2.1: ADC Reading and Processing

```
for (u_int8_t p = 0; p < 6; p++)
{
    for (u_int8_t j = 0; j < iter; j++)
    {
        buf[p][j] = Sens[p].read_u16();
        if (max_buf[p] <= buf[p][j])
            max_buf[p] = buf[p][j];
        if (min_buf[p] >= buf[p][j])
            min_buf[p] = buf[p][j];
        sum_buf[p] += buf[p][j];
        wait_us(100);
    }
    // Using pseudomedian to filter data
    pseumed[p] = (sum_buf[p] - min_buf[p] - max_buf[p]) /
    (iter - 2);
}
```

The full code can be found in Appendix A.

2.4 Experimental phase and results

2.4.1 Investigation of Sensor Geometry Influence: Experimental Configuration

The experimental setup involves a comprehensive system integrating various components for precise measurements. Two PEGS, featuring both old and new geometric designs (Figure 2.5), are placed inside a centrifugal test container filled with distilled water. Within this container, a dedicated PCB, which houses the SHT33-DIS sensor, monitors ambient temperature and humidity (Figure 2.10).
The container is then placed in a climatic chamber, with the temperature maintained at 25 °C. The PEGS are connected to the data processing board through buffer amplifying boards which have selected AD8615 chips. This setup ensures the integrity and accuracy of the sensor signal. The STM32 Nucleo board, which is noted on the scheme as a data processing board, equipped with the dedicated ADC, measures the voltage outputs from the sensors. These voltage readings are then converted into resistance values, using the reference resistor of the voltage divider of the buffer amplifying board as a baseline. Finally, the resistance values were sent to the PC by USB protocol for visualization and further analysis.

2.4.2 Investigation of Sensor Geometry Influence: Results and Discussion

The duration of the experimental observations was set for two hours, during which the conditions within the test container were closely monitored. The humidity levels achieved 100% RH approximately one hour into the experiment, a saturation point that was visually confirmed and documented in Figure 2.11b. This saturation is critical because it represents the environmental equilibrium point at which the resistance response of the PEGS is expected to stabilize.
Subsequent to reaching full humidity, the PEGS exhibited a delay before their resistance response stabilized, as indicated in Figure 2.11a. This delay can be attributed to the time required for the sensors, being in the same saturated environment, to equilibrate with the water content in the paper sensor. Given that

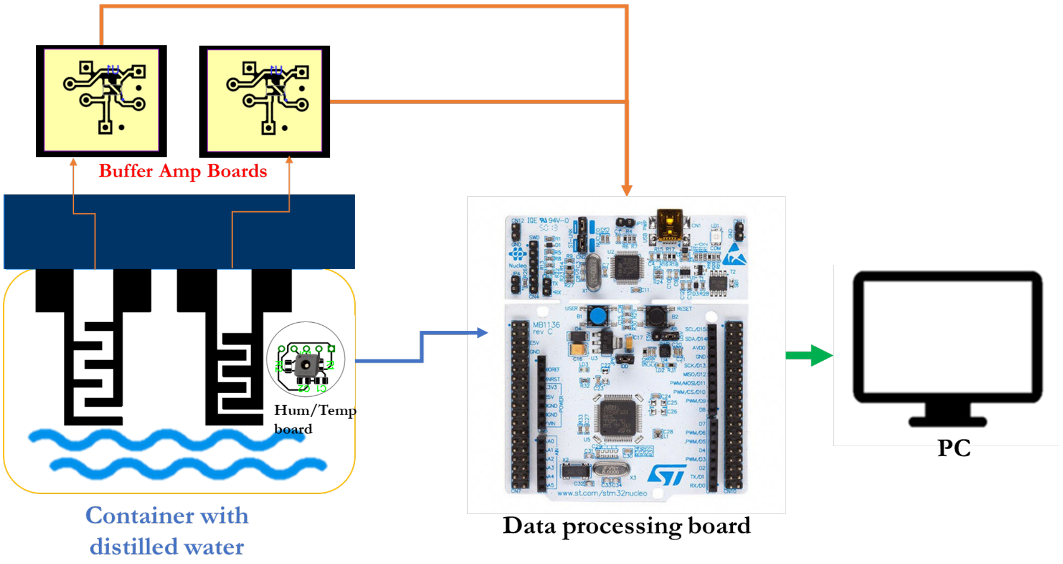

(a) Schematic of the the principal components of the experiment with PEGS design improvement

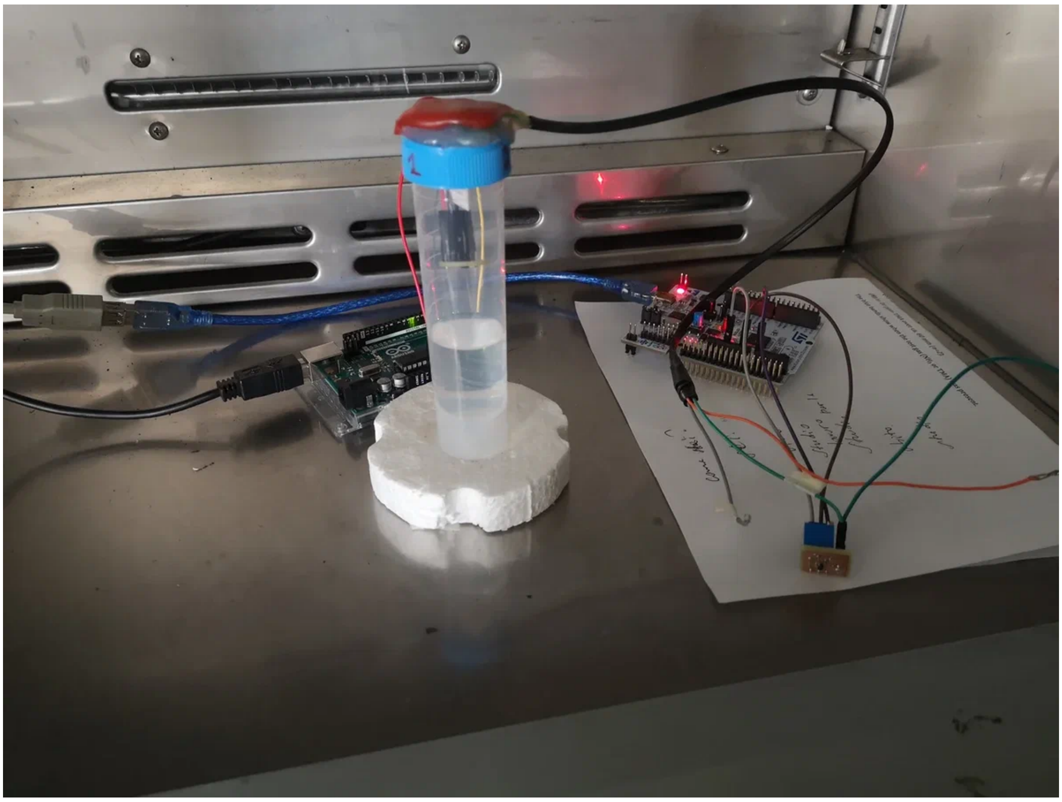

(b) Showcasing of the principal components location for the experiment with PEGS inside climatic chamber

Figure 2.10: Optimization of PEGS geometry: experimental setup

the resistance of PEGS is highly sensitive to moisture content, this stabilization phase is key to understanding the response dynamics.

The experimental data showed a notable increase in the relative resistance of the

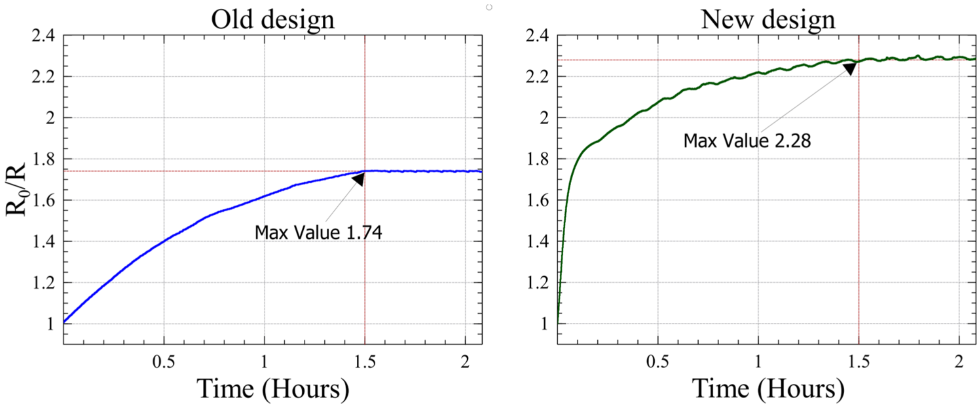

(a) Relative resistance response of PEGS

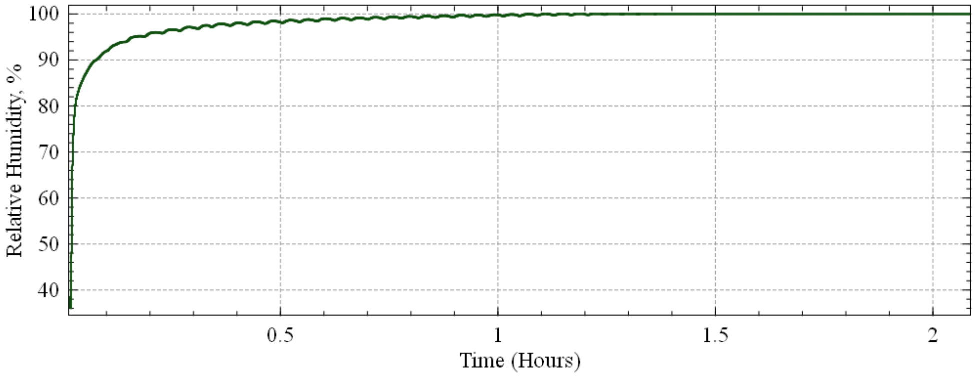

(b) Humidity levels inside the experimental container

Figure 2.11: Comparative results of PEGS geometry optimization

new PEGS design compared to the old, with the new design reaching a plateau of approximately 2.28, a 30% increase over the plateau of the old design of 1.74. This empirical finding is in strong agreement with the simulated prediction of a 30.1% enhancement in resistance response due to the design changes, as formulated in Equation 2.7. The experiment thus validates the simulation's hypothesis that the geometric modifications would amplify the sensor's response, particularly in a high-humidity environment. The additional time required for the resistance to stabilize after reaching 100% RH underscores the sensor's dependency on the moisture equilibrium within the paper, reaffirming the design's efficacy in moisture-sensing applications.

2.4.3 Paper Electrical Gas Sensors System Design for Food Spoilage Detection

An experimental system was devised to evaluate the efficacy of PEGS for detecting changes in food spoilage. The setup, as illustrated in Figure 2.12, consisted of two sealed containers, one containing distilled water and the other containing fish fillets. Both containers were equipped with a humidity and temperature sensor to monitor ambient conditions. The distilled water container served as a control to isolate the humidity variable, while the container with fish fillets represented the variable environment in which the sensor response to potential spoilage was evaluated.

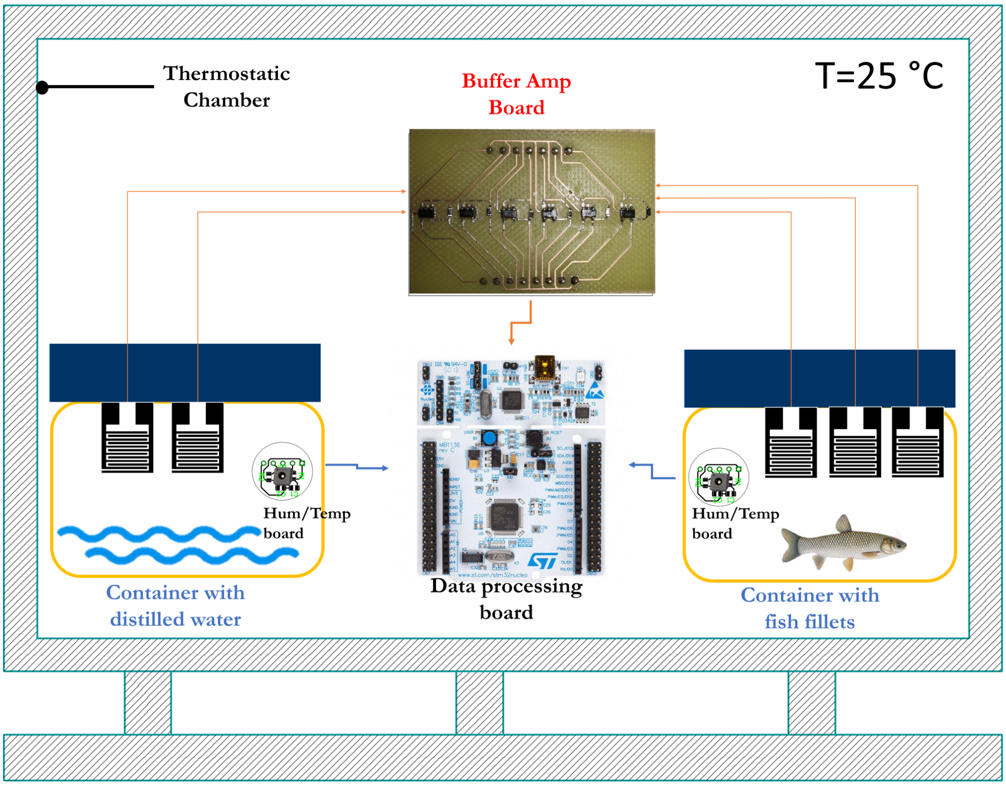

Figure 2.12: Schematic representation of the experimental setup of food spoilage detection.

The core of the data acquisition system consisted of a custom-designed PCB that utilized a voltage divider architecture integrated with six AD8615 buffer amplifiers. This design aimed to measure the high impedance of the PEGS with precision. The signals from the PEGS in both containers were first conditioned by the buffer amplifier board before being transferred to the STM32 Nucleo board. The Nucleo board processed these signals using a custom filter (see code 2.1) and then transmitted the data to a PC for further analysis. The objective was to discern whether the PEGS could detect specific signs of fish spoilage as opposed to simply responding to changes in humidity. Should the sensors in the fish fillet container exhibit a signal pattern distinctly different from that of the control container, it would indicate the sensors' potential to identify spoilage-related changes, thereby demonstrating their applicability in food freshness monitoring.

2.4.4 [Results and Discussion of the Paper-Based Electrical Gas Sensors Experiment

The experiment was carried out in a controlled environment at a temperature of 25 °C, which is known to accelerate the spoilage process in fish fillets. Both the test and control boxes reached 100% humidity after 2 hours, ensuring a saturated humid environment for the progression of spoilage, tracked concurrently through a microbiological study.

Figure 2.13 displays the resistance readings of the PEGS in the fish fillet box, which show a significant deviation from the control water box. This distinction in sensor output, coupled with the logarithmic increase in the count of CFU beyond the safety limit of 10^7 CFU/g set by the ICMSF [48], indicates effective detection of spoilage. Rapid increase in CFU provides a microbiological basis for the sensor response, affirming the role of controlled temperature in microbial growth and spoilage.

Traditional microbiological culture methods served as the standard for comparison in our tests. Each experiment utilized a 10 g portion of fresh codfish fillet. This sample was transformed from solid to liquid form, making it suitable for application on brain heart infusion agar culture media (BHIA). Using a stomacher instrument (Intescience Microbiology, Saint Nom, France), the sample was dispersed in physiological saline at a starting dilution of 1:10. The resulting mixture was serially diluted, was then spread on the surface of the agar plates, and incubated at 37 °C for a duration of 24 hours. Colony counts on each plate were determined using ImageJ software [49], allowing for an assessment of the microbial load. These evaluations were conducted at the onset (T0), as well as after 6 and

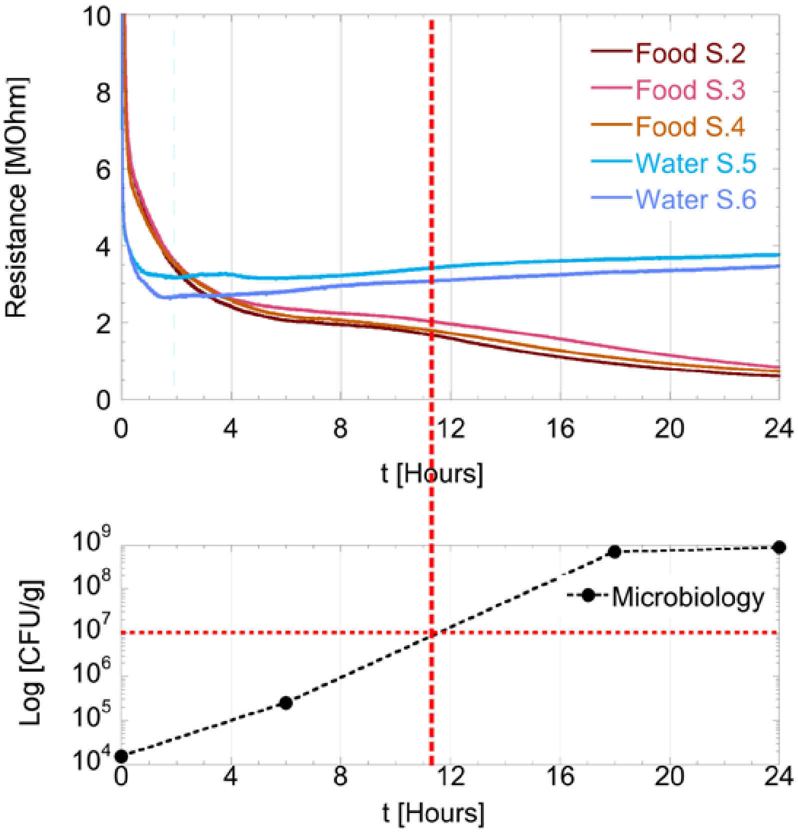

Figure 2.13: Resistance measurements of PEGS in the presence of fish spoilage and the corresponding CFU growth over time.

18 hours (T6, T18) and at the conclusion of the experimental period (T24). These results demonstrate the potential of PEGS in food quality monitoring applications, which are capable of differentiating between humidity and spoilage. The ability of these sensors to detect spoilage through resistance measurement could lead to the development of smart packaging that alerts consumers to food quality, improving food safety protocols. Further research could expand on these findings to refine the sensors for various types of food and levels of spoilage.

2.4.5 Implementation of NFC Technology for Communication and Powering the Device

The integration of NFC technology is critical to the advancement of smart packaging systems for the detection of food spoilage. The ubiquity of NFC in consumer devices, such as smartphones and tablets, makes it a versatile tool for seamless and user-friendly communication [24]. The ability to power devices via NFC eliminates the need for conventional batteries, paving the way for more sustainable and eco-friendly food packaging solutions. This battery-less approach not only reduces waste, but also simplifies the system, enhancing the overall user experience. The choice to utilize NFC is underpinned by its growing application in various domains, as evidenced by the widespread adoption and versatility of this technology in the consumer market [50].

The versatility of NFC technology lies in its dual-functionality; it enables both data transmission and energy harvesting. This duality is particularly beneficial in food packaging, where the ease of scanning an NFC tag with a mobile device facilitates real-time monitoring of food quality [51].

By drawing power from an NFC-enabled reader, the sensor system avoids the need for batteries on board, which is consistent with current trends in environmental sustainability [52, 53, 54]. The removal of batteries from the equation not only reduces the environmental impact but also reduces the bulk and cost associated with the packaging, making it more practical and appealing to both manufacturers and consumers.

In the subsequent section, we will dive deeper into the technical implementation of NFC in our sensor system and discuss its implications for the future of smart food packaging.

Selection Criteria for NFC Module in Smart Packaging Project

In the development of an NFC-enabled smart packaging system, the selection of an appropriate NFC module is critical. The criteria for this selection are multifaceted, focusing on compatibility, memory capacity, dual-interface functionality, and ease of integration with existing microcontroller units (MCUs).

Compatibility with widely used MCU architectures, such as STM32 and Arduino UNO R3, is essential for ensuring seamless integration and flexibility in development. Furthermore, substantial EEPROM memory is crucial for data storage and retrieval processes integral to smart packaging applications. Dual-interface functionality, incorporating both NFC and RFID capabilities, broadens the scope of communication and enhances the system's versatility. Furthermore, the module

must support a range of libraries to facilitate custom application development, allowing for specific customization to project requirements.
Given these criteria, the STMicroelectronics X-NUCLEO-NFC01A1 (Figure 2.14) emerges as an appropriate choice for our project. This NFC evaluation board is created based on the M24SR64-Y chip, a dynamic NFC/RFID tag IC that meets all the criteria outlined [55].

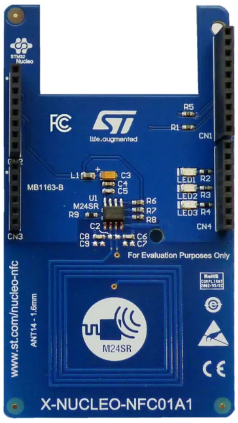

Figure 2.14: X-NUCLEO-NFC01A1 board: Top view, highlighting compatibility with STM32 and Arduino UNO R3 MCUs

The X-NUCLEO-NFC01A1 board features the M24SR64-Y chip, which offers a dual interface and incorporates a 64-kbit EEPROM memory. Its compatibility with versatile Arduino platforms ensures that the board can be easily integrated into our existing system architecture. The dual interface capability of the M24SR64-Y chip is particularly advantageous for smart packaging applications, enabling NFC and RFID communication modes [55]. This feature aligns with the project's goal of creating a versatile and user-friendly smart packaging system. The onboard 64-kbit EEPROM provides sufficient memory for data storage, a key requirement for tracking and monitoring in smart packaging.

Design and Implementation of the Custom PCB

The development of a custom PCB compatible with the Arduino UNO format is a crucial part of this project. This PCB incorporates the Attiny85 MCU, chosen for its ability to communicate with the M24SR64-Y chip via the I^2C protocol. The key factors influencing the selection of Attiny85 include its compact size, low power consumption, and sufficient capability to handle the required communication and processing tasks.

The Arduino framework was utilized to program Attiny85, providing a familiar and versatile development environment. This approach allowed for rapid development and testing, using the extensive libraries associated with Arduino. The code developed for the Attiny85 MCU, which facilitates the operation of this custom PCB, is included in the Appendix A.2 for reference.

An integral feature of the Attiny85 MCU is its internal ADC. This ADC was used to measure the resistance of the PEGS, which is essential to determine the state of spoilage of the monitored food products. The use of the MCU's built-in ADC simplifies the circuit design and reduces the overall footprint of the PCB, making it more suitable for integration into smart packaging systems.

The schematic in Figure 2.15a illustrates the connection between the Attiny85 microcontroller (U1) and the M24SR64-Y NFC module, integral for the NFC tag X-NUCLEO-NFC01A1. The Attiny85 is interfaced with the M24SR64-Y chip via the I^{2}C protocol, enabling communication with the NFC module. The choice of the I^{2}C protocol facilitates a simple two-wire interface, minimizing the required connections and preserving the MCU's I/O pins for other functions or sensors.

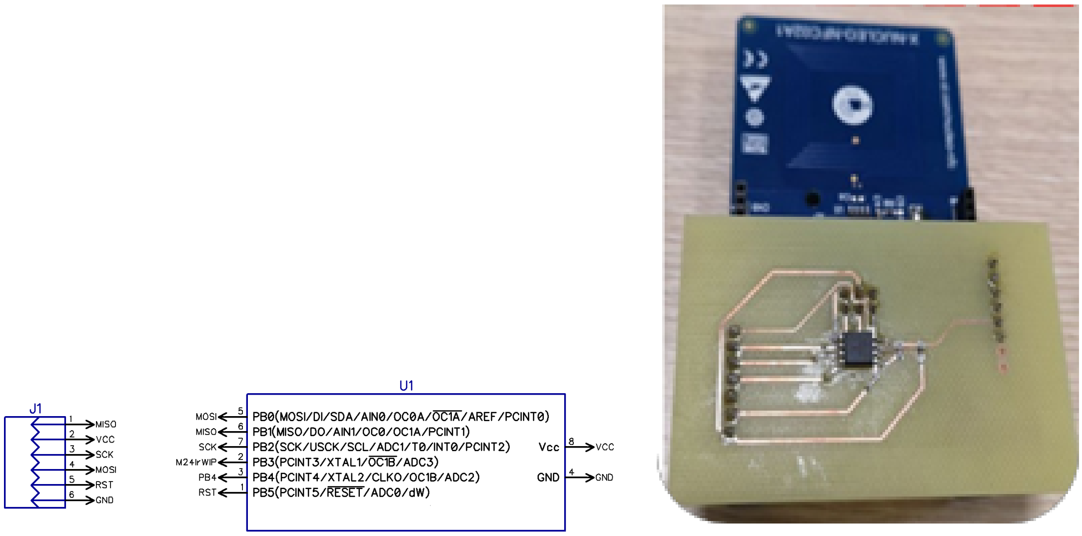

(a) Schematic of NFC PCB expansion board

(b) Photo of NFC PCB expansion board

Figure 2.15: NFC PCB expansion board layout and schematic

The programming connector (J1) serves as an interface to program the Attiny85 microcontroller. The power supply to the Attiny85 is provided through the SPI connector or through the M24SR64-Y chip, which has an energy harvesting feature

that allows it to process the energy from NFC.
This configuration enables the Attiny85 to control the NFC functionality provided by the M24SR64-Y chip, leveraging the nonvolatile memory and wireless communication capabilities for smart packaging applications.

Integration of PEGS with NFC Technology in Smart Food Packaging

The PCB was developed to integrate the Attiny85 microcontroller with the X-NUCLEO-NFC01A1 and the innovative PEGS for smart food packaging applications. In a practical application, the PEGS was embedded in a food package, with the Attiny85 microcontroller that facilitates the readout of sensor data through the NFC communication link (Figure 2.16).

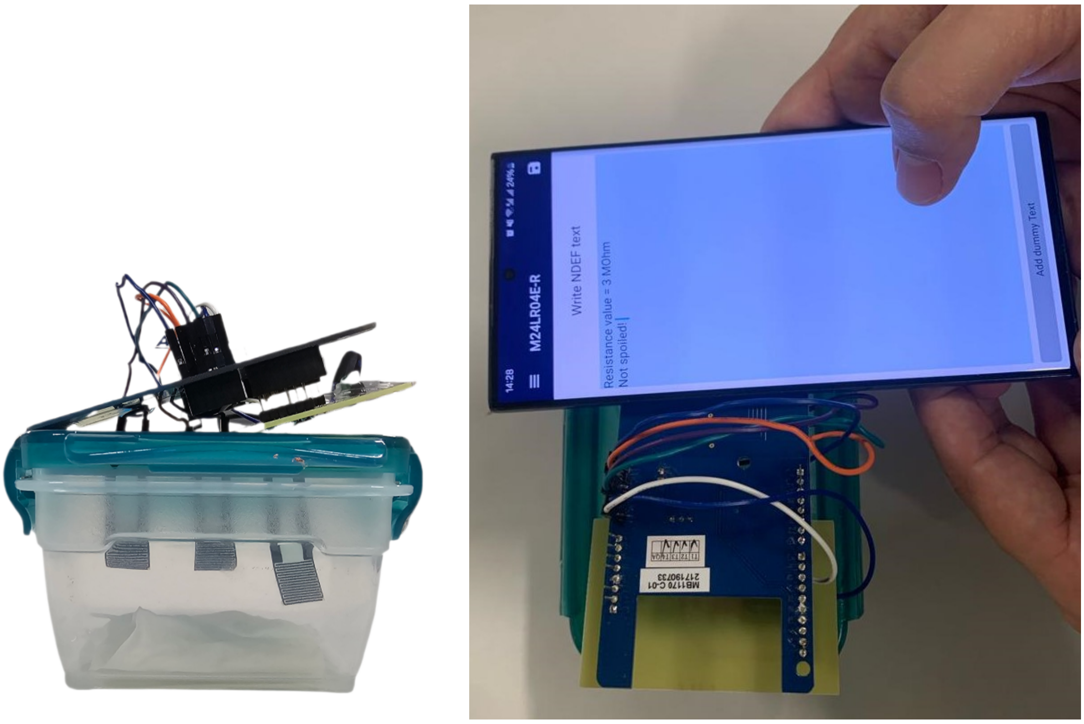

Resistance value = 3 MOhm
Not spoiled!

(a) Assembly prototype of the food spoilage system

(b) Scanning the spoilage information using a smartphone powered by NFC

Figure 2.16: Proof of concept showing the implementation of NFC in the food spoilage measurement

This setup allowed for the detection of trace spoilage gases quickly and accurately. Furthermore, the system was tested using a mobile phone with NFC capability to power the PCB and read the sensor resistance, demonstrating the potential of consumers to easily monitor food safety. Figure 2.16b shows a hand holding a smartphone above a custom electronic device setup that is designed to measure food spoilage. The smartphone runs an NFC-based application that is used to power the setup and read data using NFC technology. The application screen indicates a resistance measurement of "3MOhm" from the PEGS, with the clarification that the food is "not spoiled." This suggests that the resistance value is within an acceptable range that corresponds to unspoiled food. Below the smartphone, there is an NFC PCB expansion board (Figure 2.15). This PCB is connected to an NFC module or antenna, which is used to communicate with the smartphone and draw power. There are three paper sensors within the food package, which are visible in Figure 2.16a, whose resistance is measured by the Attiny85 MCU (Figure 2.15a). These sensors change resistance as food spoils, providing a means of monitoring food freshness. The wires in various colors are for electrical connections related to this functionality. The system is an innovative application of NFC technology for food safety, where the smartphone not only reads the data from the PEGS but also provides the necessary power to the PCB, making it a portable and convenient tool for food quality monitoring. The integration of these technologies into the custom PCB paves the way for reducing food waste and improving consumer interaction with smart packaging.

Chapter 3

Comparative Analysis of Individual InAs Nanowires for Environmental Safety

3.1 Introduction

The advancement of semiconductor NWs, particularly InAs NWs, marks a significant era in the evolution of gas sensing technologies. These NWs are increasingly recognized for their high electron mobility and surface sensitivity [56], making them promising candidates for environmental monitoring applications. This chapter presents a comprehensive comparative analysis of individual InAs NWs, exploring their efficacy and potential in the realm of environmental safety, especially in gas detection.

This chapter starts with a review of current advancements in gas sensing technologies, emphasizing the pivotal role of semiconductor NWs. This is followed by a detailed description of the synthesis, fabrication, and characterization methods used for InAs NWs. The experimental section then presents findings on the sensitivity and performance of the NWs in detecting relative humidity (RH) and nitrogen dioxide (NO_2). A thorough analysis of these results is provided, including a noise analysis and a comparative study of the NWs' responses to environmental stimuli.

The chapter concludes by summarizing the key findings and their implications for the development of high-performance gas sensors. It also outlines recommendations for future research in this domain, underscoring the significance of this study in the broader context of environmental monitoring and safety.

In my research on InAs NWs, I have made several key contributions to their characterization. Firstly, I developed a PCB tailored for InAs NWs. This PCB was not only designed to achieve high precision in data collection, but also meticulously engineered to prevent damage to the NWs from excessive current, by avoiding Joule heating effects that could lead to their breakage. This involved both the design and fabrication of the PCB. Secondly, I programmed the firmware for microcontrollers, which included a specialized data acquisition algorithm aimed at enhancing measurement accuracy. Additionally, I conducted electrical experiments with neighboring NWs, collecting vital data to further our understanding of the NWs. Finally, I utilized Python to plot the experiment results and perform initial data processing, thereby laying the foundation for more in-depth analysis. Collectively, these steps played a crucial role in advancing the characterization techniques for InAs NWs.

3.2 State of the Art

Sensors play a pivotal role in numerous modern technologies, becoming increasingly vital in a wide array of applications. Among these, environmental gas detection stands out as an area where sensors provide critical functionality. The demand for low-cost, easily integrable solutions in this domain has been steadily rising.

Conductometric sensors, known for their operation based on current modulation due to surface interactions between gases and semiconductors, have emerged as a cost-effective and reliable option in this context [57]. These sensors offer a straightforward yet efficient method for detecting various gases, making them highly sought after for environmental monitoring and other applications.

The rapid advancement of nanotechnology and nanofabrication techniques has been instrumental in the creation of innovative instrumentation. This progression in technology has facilitated the creation of nanostructured-based sensors, which exhibit enhanced performance characteristics compared to their traditional counterparts [58].

Among the various nanostructures, nanowires have garnered particular interest in the field of gas sensing. Due to their distinctive physical properties, such as an optimized volume-to-surface ratio [59, 60], nanowires provide increased sensitivity in gas detection. Moreover, their well-defined crystalline facets contribute to the stability over time [61, 62, 63], a crucial factor in sensor reliability and longevity. Nanowires thus stand out as especially suitable for applications in gas sensing, combining enhanced sensitivity with structural stability.

Recent advances in nanowire-based sensing systems, particularly those using semiconductor nanowires, have shown significant potential in the field of chemical sensors. The use of semiconductor nanowires allows direct electrical reading, improving sensing capabilities [64, 62, 63]. These developments underscore the growing interest in nanowire-based technologies for next-generation chemical sensors. In gaseous environments, semiconductor-based sensing is primarily facilitated by charge transfer processes involving adsorbed molecules or by changes in the Schottky barriers at their contacts [65, 66, 67]. Most experimental studies focus on the collective performance of an ensemble of nanostructures, which presents challenges in accurately assessing individual nanowire properties [64, 68]. Research into single nanowire sensors, particularly for metal oxides like SnO_2 and ZnO, has been crucial in understanding the underlying sensing mechanisms [69, 70, 71, 67].

Although metal oxide sensors are widely researched, they typically require high-temperature operation, presenting a significant drawback [72]. Alternative methods such as UV-induced adsorption and desorption allow operation at room temperature, mitigating this problem [71].

InAs nanowires have shown promise due to their high electron mobility and presence in the surface state, adapting them for gas detection purposes [56, 73, 74]. These sensors have demonstrated effectiveness in detecting gases like ethanol and NO_2 at low concentrations and in various environments [56, 75, 76].

Despite the progress in sensing in inert atmospheres, there is a growing need for devices that can operate effectively in real environments, such as air [77]. Our previous work has focused on exploring InAs nanowire sensors in air, studying different architectures and their impact on gas sensing [78]. This research high-

lights the need for further investigation into the robustness and reliability of InAs nanowire devices in varying environmental conditions.
In this work, we extend this research by conducting a direct comparison of two nominally identical nanowires positioned near. This study aims to unravel the physics underlying their sensing behavior and to examine if variations in individual behavior affect their sensing capabilities. To achieve this, we engineered a device featuring several individually contacted nanowires on the same chip. In addition, we developed a custom readout interface that enables the simultaneous reading of two proximate nanowires. Our approach involves applying noise analysis to the data obtained from the devices when exposed to humidity and NO_2 pulses within the test chamber.

3.3 Materials and Methods

The work presented in this section revolves around the fabrication and precise electrical characterization of InAs NWs. A specialized circuit was created and put into effect to precisely gauge the resistance of the NWs. Circuit design emphasized minimizing self-heating effects in NWs, a significant challenge in accurate resistance measurement.

3.3.1 Sample Fabrication

The sample fabrication was significantly improved through a collaborative effort with the Scuola Normale Superiore Pisa, Italy.

Substrate Preparation and Nanowire Synthesis

Wurtzite n-type InAs NWs were synthesized using gold-assisted Chemical Beam Epitaxy (CBE) [79] on InAs$\{111_B\}$ substrates. The InAs$\{111_B\}$ substrate, particularly in its Wurtzite form, is favored due to its low stack fault density [80]. These structural properties, combined with specific surface states and Fermi-level positioning, make InAs nanowires highly sensitive to chemical vapors [81]. The growth process employed gold nanoparticles as catalysts under the Vapor-Liquid-Solid (VLS) mechanism. Trimethylindium (TMIn) and tertiarybutylarsine (TBA) were selected as indium and arsenic sources, respectively, for their suitability for nanowire growth [81].

Gold Nanoparticle Catalyst Formation

Gold nanoparticle catalysts were created by dewetting a 0.5 nm thick gold film, evaporated onto InAs substrates. Dewetting was carried out at 540 ± 10 °C under a TBA flow for 20 minutes, facilitating the breakage of the gold film into nanoparticles. These nanoparticles are crucial for the growth of VLS in NWs [82, 81].

Nanowire Growth Conditions

The actual growth of NWs was carried out at 465 ± 10 ° C to balance the decomposition of TMIn and TBA with the stability of the gold nanoparticles. The pressures for TMIn and TBA were approximately 0.9 and 0.3 Torr, respectively, controlled to influence the stoichiometry and growth rate of the nanowires. The duration of growth was approximately 45 minutes, optimized to achieve the desired length of the nanowire while preserving structural and electrical integrity [81].

N-Doping and Detachment

Ditertiarybutylselenide (DtBSe) was used at a line pressure of 0.10 Torr as an n-doping source during the growth. The effectiveness of DtBSe in modifying the electrical properties of the nanowires is crucial for applications like field-effect transistors. Post-growth, the NWs underwent a gentle mechanical detachment process from the growth substrate to preserve their structural integrity. The detached NWs were then dispersed in isopropyl alcohol (IPA) by sonication, an effective method for uniform dispersion [83].

Nanowire Deposition and Device Integration

For device integration, a droplet of the IPA / NW solution was deposited onto a pre-patterned degenerately doped p++Si/SiO_2 substrate using the dropcasting technique. The substrate had a 0.5mm Si layer with a 280nm SiO_2 layer. This method is crucial for aligning the nanowires with the device's architecture [12].

Contact Electrode Patterning

The patterning of the contact electrodes in the InAs NWs is achieved by electron beam lithography (EBL). This high resolution technique is essential to define the nanoscale features of the contact electrodes.The SEM image in Figure 3.1 shows the intricate electrode layouts and highlights two selected InAs nanowires, which underscore the precision of the EBL process in defining these features. Following EBL, a passivation step is performed using an ammonium polysulfide $(NH_4)_2S$ solution is performed to eliminate indigenous oxides from the surface of the NWs. This step is crucial in promoting the formation of low-resistance ohmic contacts [84, 85]. Finally, a bilayer metal contact consisting of chromium (Cr) and gold (Au) is evaporated onto the patterned areas to complete the contact electrode formation process.

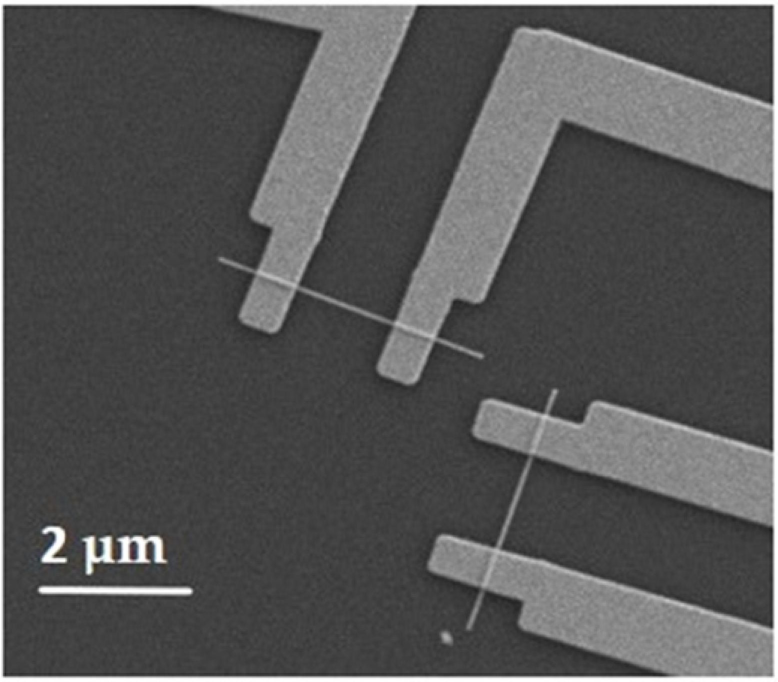

Figure 3.1: SEM image showing electrode layouts and two selected InAs nanowires, highlighting the nanoscale features achieved through EBL.

Chip Carrier Attachment and Wire Bonding

The chip was then attached to a standard Dual-in-Line (DIP) chip carrier using a conductive silver paste. This type of paste is commonly chosen for its high electrical conductivity [86], which is crucial to maintaining a reliable electrical connection in chip packaging. Additionally, the conductive silver paste often exhibits strong adhesive properties, ensuring a secure mechanical bond between the chip and the carrier [86, 87]. The specific choice of this material aligns with industry standards in electronic device fabrication, where maintaining both electrical and mechanical integrity is paramount. Once the chip was securely attached, the devices were wire-bonded to the carrier, completing the process of integrating the nanowire-based devices into a functional unit(Figure 3.2).

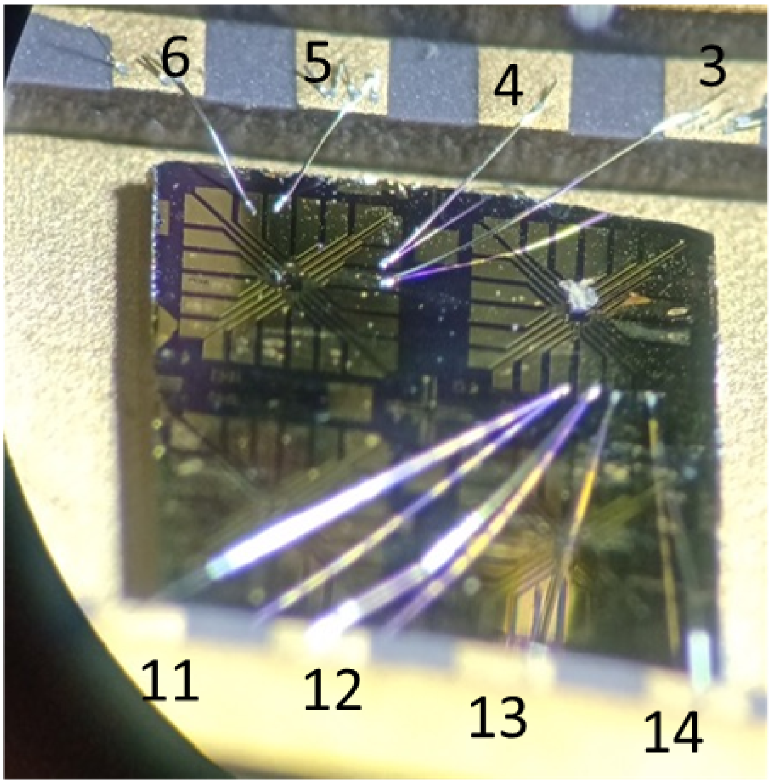

Figure 3.2: Close-up of the electronic chip attached to a Dual-in-Line chip carrier using a conductive silver paste, showing numbered electrodes.

This final step is vital for establishing a connection between the nanowire devices and the external circuitry, allowing for subsequent testing and application.

3.3.2 Development of the Measuring Device for InAs Nanowires Characterization

In this subsection, we explore the development of an advanced measurement device tailored for the characterization of two selected neighboring InAs NWs. This development was primarily driven by the goal of investigating similarities and differences in the signals obtained from two closely positioned NWs under identical conditions. The critical aspect of this study was the ability of the new device to measure the resistance of two NWs simultaneously, providing information on their collective electrical responses. The previous work was performed with an individual InAs NW [78] by a picoammeter at constant voltage. In the development of an advanced measurement device for simultaneous characterization of two neighboring InAs NWs, several key factors underpin its necessity and advantages over the use of individual commercial picoammeters. Primarily, simultaneous measurements under identical conditions are crucial, as they ensure that both NWs are subjected to the same experimental parameters, enabling a controlled and accurate comparison. This approach is critical to observe real-time data synchronization and comparison, particularly for detecting subtle differences. Moreover, using a single device enhances resource efficiency and simplifies the experimental setup, thereby reducing potential setup-related discrepancies. Customizing our device to measure multiple nanowires simultaneously is an essential step in developing a smaller, commercially viable version for broader use.

A significant challenge in this effort was the inherent fragility of InAs NWs, which necessitated a current limitation to prevent damage. As previous studies show [88], InAs NWs are prone to breakdown under high current densities, leading to substantial changes in their composition and structure. This fragility required careful consideration in the design of the measuring device to ensure stable and accurate readings without compromising the integrity of the NWs. The following sections detail the design considerations, challenges encountered, and innovative solutions implemented to develop a reliable and effective system for nanowire characterization.

Impact of Joule Heating in Constant Voltage Measurements

In the initial stages of our experiment, we employed a constant voltage method to measure the resistance of InAs NWs. This approach involved applying a consistent voltage across the nanowires and measuring the resultant voltage drop, thereby allowing us to calculate their resistance. The circuit was based on a simple voltage divider architecture which, while effective in maintaining a constant voltage,

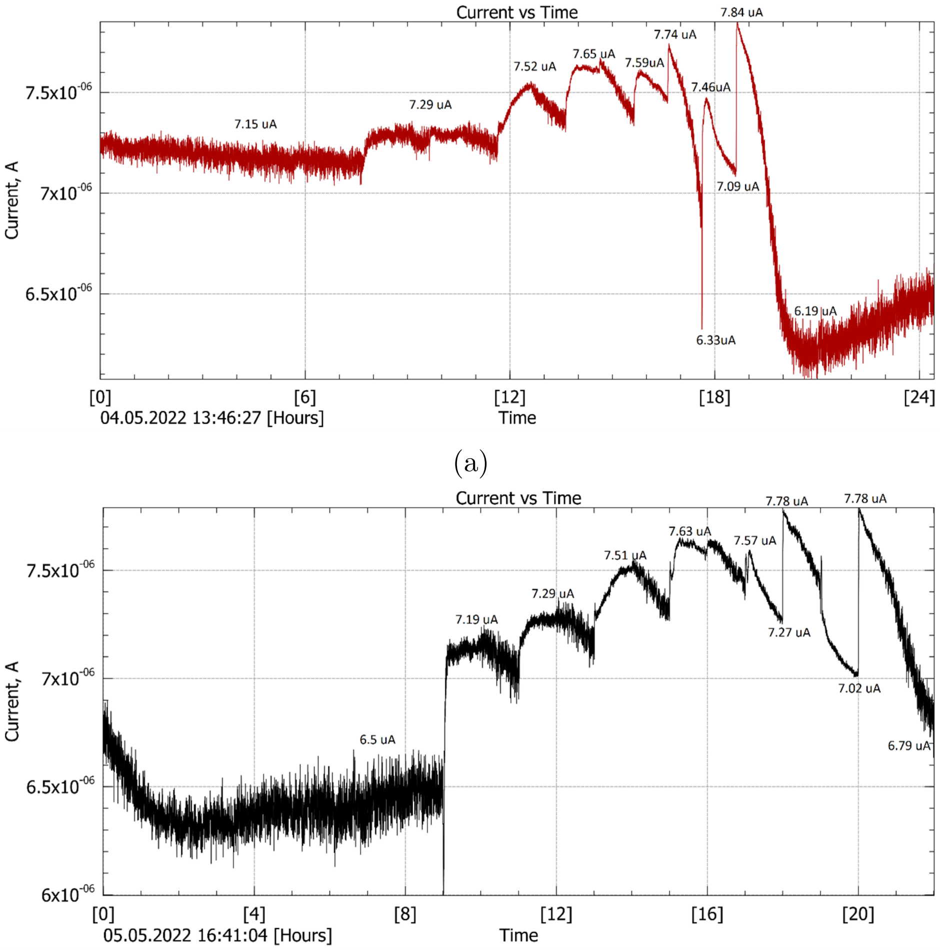

(a)

(b)

Figure 3.3: Impact of Joule heating on signal quality: current-induced deterioration in InAs NWs

presented certain challenges when it came to managing the effects of Joule heating. As we exposed the NWs to varying levels of relative humidity (RH) and NO_2, we observed a decrease in their resistance. This decrease in resistance under a constant voltage scenario led to an increase in the current flowing through the NWs. Consequently, the increased current resulted in a significant rise in Joule heating within the nanowires. This heating effect was found to be detrimental to the sensitivity of the NWs, possibly due to heat-induced structural or compositional changes, as noted in our previous observations and supported by the literature [88].

The impact of Joule heating on signal quality and integrity of InAs NWs is visually represented in Figure 3.3. The figure illustrates the correlation between increased current and deterioration in signal quality, highlighting the challenges faced in maintaining the sensitivity and stability of the NWs under the constant voltage measurement method.

New Circuit Design with Constant Current Source

Following the initial experiments using a constant voltage approach, we transitioned to a circuit configuration using a constant current source. This change was prompted by the need to mitigate heating-induced changes in current, a critical factor in the accurate measurement of nanowire resistance. It is well documented that nanostructures and nanowires can experience significant self-heating at very low power levels [89]. Although the heating effects are less pronounced in substrate-supported nanowires, such as those in our study, compared to suspended ones [90], they are still significant enough to warrant careful consideration. To circumvent potential damage from self-heating, we maintained a stable current of 2 µA across the source and drain contacts of the nanowires throughout our experiments.

The redesigned circuit for dual NW resistance measurement is comprised of six primary components, each playing a pivotal role in ensuring accurate and stable readings. These components include:

- Two LM334-based constant current sources: Chosen for their precision in maintaining a stable current, essential for minimizing self-heating in the NWs [91],
- The AD8656 amplifier, with its high input impedance and low noise, ensures minimal disturbance to the NW's delicate signal [92],
- The ADS1220 ADC was chosen for its high-resolution capabilities, allowing for precise digital representation of the NW's analog signals [93],
- The Arduino UNO microcontroller unit (MCU) [94]: Selected for ease of use, flexibility, and wide community support. It effectively coordinates data acquisition and control functions in the circuit, interfacing seamlessly with other components like the ADC and temperature sensor,
- The SHT33-dis ambient temperature sensor [95]: Incorporated to accurately monitor the ambient temperature. This is crucial as the ambient temperature

influences the current output of the LM334 current sensors. By tracking these temperature variations, we can more precisely determine the actual current flowing through the NWs, enhancing the accuracy of our resistance measurements,

- A personal computer (PC) for data acquisition and analysis.

This setup, as illustrated in Figure 3.4, ensures precise control over the current flowing through the NWs and allows accurate measurement of their resistance. In the circuit (see Figure 3.4a), the resistor labeled "NW" directly represents the nanowires under study.

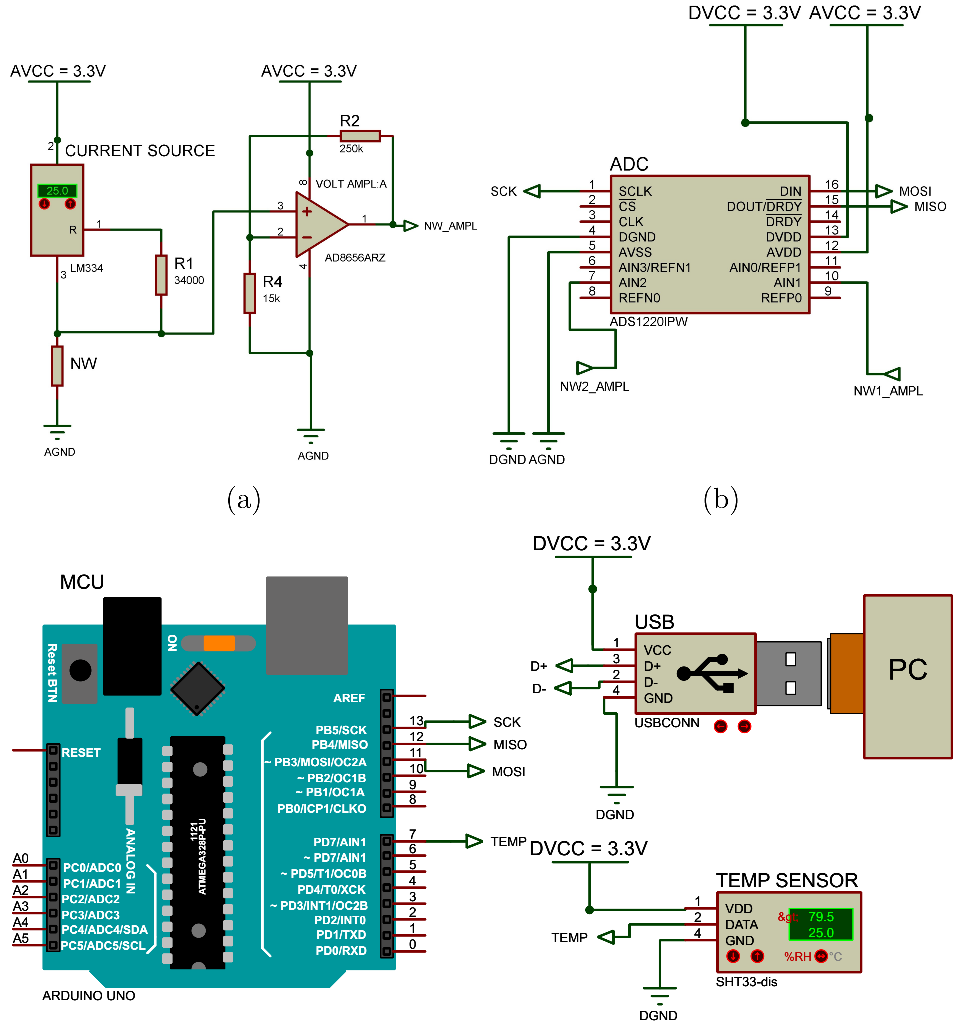

(a) (b)

(c)

Figure 3.4: Schematic block diagram of the NW resistance measurement circuit: **(a)** **(x2)** NWs resistance voltage conversion, representing two identical circuits in the actual setup (only one is depicted for clarity), **(b)** analog-to-digital conversion, **(c)** data processing and data transmission.

In Figure 3.4a the CURRENT SOURCEs are configured to provide a consistent current to the NWs. This current, set at 2uA, is determined by resistor R1 [91]. As the current traverses the NWs, it generates a voltage in line with Ohm's law. The voltage from each NW is then amplified by the VOLT AMPL, with a gain factor of 16.5. Consequently, when the resistance of the NWs is at its peak value of 100k, the resultant voltage is approximately 3.3V. This value represents the maximum input voltage for the ADC (Figure 3.4b), ensuring optimal resolution for current measurements. The ADC is connected to the MCU via the serial peripheral interface (SPI), through which it transmits information on the voltage drop observed across the NWs. The data is then subject to further processing by the MCU (Figure 3.4c). To account for the temperature drift of the CURRENT SOURCE, a temperature compensation mechanism was integrated into the circuit design. This mechanism comprises a TEMP SENSOR that is capable of measuring the temperature around the CURRENT SOURCE circuit and transmitting this information to the MCU for processing. By taking into account the data obtained from the ADC and the TEMP SENSOR, the MCU is able to compute the true value of the resistance of the NWs, thus correcting for any temperature-induced variations in the CURRENT SOURCE output. In real time, the PC retrieves data on the resistance of the NWs via a USB interface connected to the MCU. This information is then visualized and concurrently saved to text files, facilitating subsequent analysis.

Description of the Data Acquisition Algorithm

The algorithm for data acquisition in the MCU can be broken down into several key components. Each component plays a crucial role in the overall functionality of the system. The following is a brief description of these main components:

- **Sensor Initialization:** The code begins with the inclusion of the necessary libraries and the definition of pin configurations. It initializes the TEMP SENSOR , which is responsible for measuring temperature and humidity. The initialization process checks whether the sensor is connected and functioning correctly.

- **Configuration of ADC:** The ADC is set with specific parameters such as data rate, programmable gain amplifier (PGA) settings, and conversion mode. This ADC is crucial for converting the analog signals from the sensors into digital values that the Arduino can process.

- **Interrupt Handler:** An interrupt handler function `drdyInterruptHndlr` is defined to handle the data ready (DRDY) signal from the ADS1220. This interrupt-driven approach ensures timely reading of data when it becomes available.

- **Main Loop:** The `loop` function contains the core logic for data acquisition. It periodically reads temperature and humidity data from the TEMP SENSOR and processes the values from the ADC. The loop handles the timing and sequencing of these readings.

- **Data Processing:** Within the main loop, the code reads the values, calculates the voltage and then converts these values to resistance measurements for the nanowires. This process involves filtering and averaging to improve the accuracy of the measurements.

- **Function Definitions:** Several functions are defined to perform specific calculations, such as converting ADC data to millivolts, calculating the current and voltage based on temperature, and converting these values to resistance for both channels of the nanowires.

- **Sending Data to PC:** The code includes the functionality to send the processed data to a connected PC for further analysis or display. Using the `Serial.print` and `Serial.println` functions, it outputs temperature, humidity, and resistance values through the serial port of the MCU. These data are formatted as a comma separated string, making them easy to parse and interpret on the receiving end. Serial communication is initiated in the `setup` function with `Serial.begin(9600)`, setting the baud rate for data transmission. This feature allows for real-time monitoring and logging of sensor data on a PC.

This algorithm effectively integrates sensor readings with ADC processing to provide real-time monitoring and data acquisition for the NWs' resistance measurements. The code can be found in the appendix A.3

Electrical Setup in the Climatic Chamber

Figure 3.5 provides a detailed photographic view of the experimental electrical setup used in this study that illustrates the location of the main electrical components.

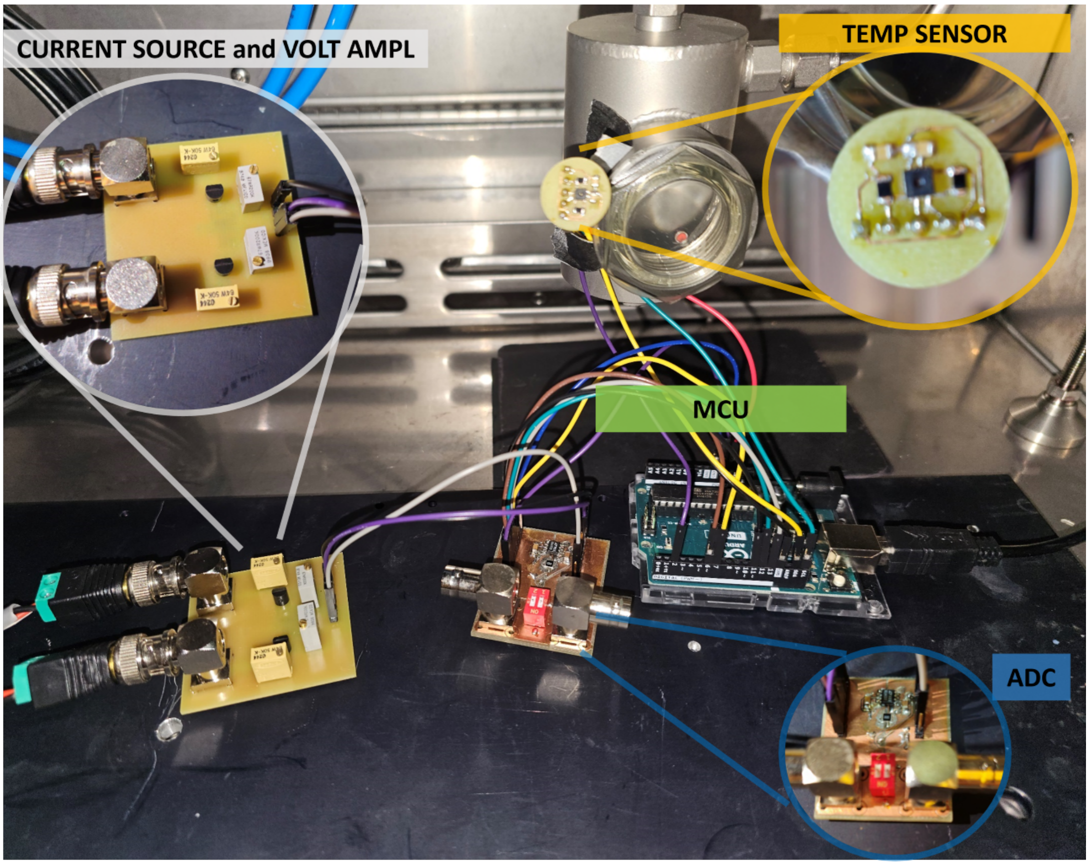

Figure 3.5: Photographic depiction of the electrical setup.

Effectively demonstrates the intricate integration of critical components, including the current source, the voltage amplifier (VOLT AMPL), the NW, the ADC, the MCU and the temperature sensor (TEMP SENSOR), all located within a climatic chamber. The arrangement is meticulously designed to facilitate precise control over environmental conditions, which is crucial for the accuracy and reliability of the experimental measurements. This setup forms the backbone of the experimental apparatus, enabling systematic investigation of nanowire properties under various controlled conditions, a key aspect of this research.

3.3.3 Preparation for the Experiments

The preparation phase of the experiment involving DIP entailed a series of methodical steps, crucial to the integrity of the NWs and the success of the experimental procedures. The following summarizes these preparatory actions:

1. **Antistatic Measures:** The initial step involved wearing an antistatic bracelet. This was necessary to eliminate the risk of electrostatic discharge, which could damage the nanowires.
2. **DIP Package Insertion:** The DIP package containing the nanowires was then carefully inserted into a specially designed motherboard.
3. **Connection to Electrical System:** Subsequently, wires from the board were connected to the pins of the electrical system in the gas chamber. This step was performed with precision to ensure proper electrical connectivity.
4. **Gas Chamber Assembly:** The assembly of the gas chamber involved attaching its bottom part and securing it with bolts. A plastic gasket was placed between the lower and upper parts of the chamber to prevent any leakages, ensuring an airtight seal.
5. **System Powering:** The final step in preparation was to supply a 3.3V voltage to the board. Following this, the gas setup was initiated for the commencement of experimental activities.

The essential parts of the installation are shown in Figure 3.6. These steps were meticulously followed to prepare the experimental setup, ensuring the structural integrity of the nanowires and the operational readiness of the experimental apparatus.

3.3.4 Gas Sensing Experimental Setup

The experimental gas detection setup depicted in Figure 3.7 is designed to evaluate the response of NWs under controlled conditions.

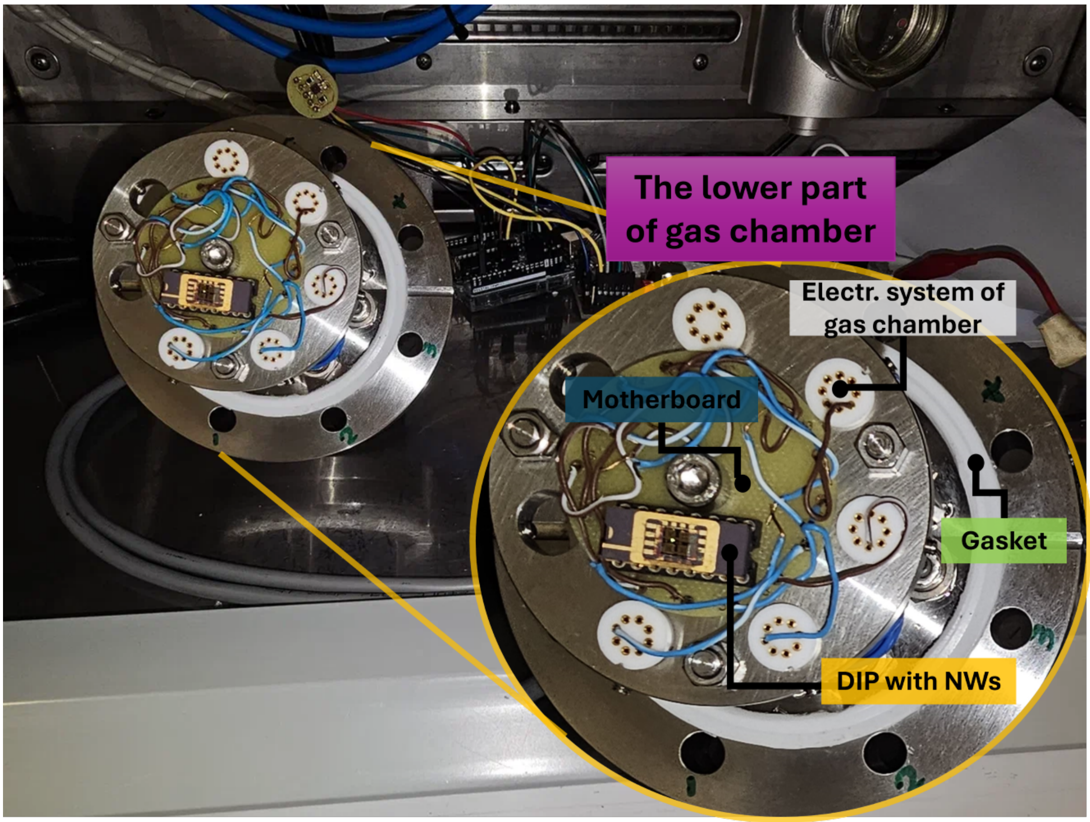

Figure 3.6: DIP with NWs installed in the gas chamber

The experimental setup for gas detection, as illustrated in Figure 3.7, is an assembly composed of principal components, each of which plays an integral role in the detection experiments. At the heart of the system lies the test chamber and the gas flow system, depicted in Figure 3.7a. This central unit is a 1000 cm^3 chamber made of stainless steel, equipped with a gas inlet and outlet to facilitate the introduction and removal of gases. The chamber receives its gas supply from certified bottles containing air and nitrogen dioxide (NO_2), with the flow rates of these gases meticulously regulated and mixed using mass flow meters. The flow rate is kept constant at 100 sccm. The gas flow was purposely maintained at a low level to prevent exerting mechanical pressure on the delicate NWs. However, this approach has a downside: it can take a considerable amount of time (up to 10 minutes) to fully replace the gas concentration within the chamber, which ultimately affects the recovery time of the sensor response. In addition, a bubbler system has been incorporated into the gas line to introduce humidity, a key feature to create various environmental conditions and calibrate the sensors.

The signal transduction process is captured in Figure 3.7b, which charts the resis-

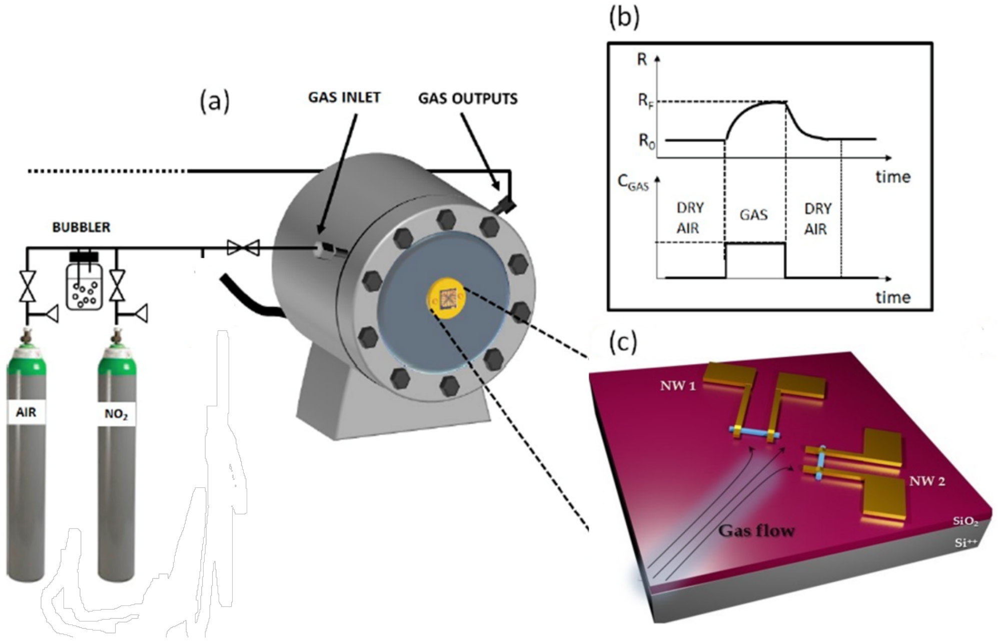

Figure 3.7: Schematic representation of the gas sensing experimental setup. (a) Test chamber with gas input system, (b) Signal transduction of NW resistance, (c) 3D model of NW arrangement on a substrate.

tance variations of the nanowires over time, correlating these fluctuations with the levels of gas concentration inside the chamber. This diagram represents a typical test cycle, showcasing the rise in sensor resistance when exposed to the target gas and its subsequent return to the baseline state upon the reintroduction of dry air. Furthermore, the arrangement of nanowires on the substrate is presented in a magnified 3D model in Figure 3.7c, showing two distinct nanowires, labeled $NW1$ and $NW2$, which are mounted on a silicon substrate with a silicon dioxide overlay (SiO_2) acting as an insulator, together located inside the gas chamber. These nanowires are connected to the electrical setup via BNC cables and are precisely positioned to ensure a uniform distribution of the gas flow over the sensor elements. The strategic placement of $NW1$ and $NW2$ is crucial, as it allows a detailed examination of the gas-sensing properties of the nanowires when subjected to various test gases.

Taken together, these components create an elaborate setup that allows for the comprehensive analysis of nanowire sensor responses, shedding light on their performance and stability in detecting different gas concentrations.

The combined features of this setup allow for a comprehensive analysis of the sensor response to varying concentrations of gases, providing insights into the performance and reliability of the nanowire sensors under study.

3.4 Results

3.4.1 Sensitivity and performance of the Nanowires in RH detection

We evaluated the sensor responses to variations in atmospheric humidity levels ranging from 10% to 70% RH in increments of 10%. Each test round consisted of a 1-hour exposure period during which the NWs were subjected to a specific and consistent level of the concentration of humidity, proceeded by a 1-hour the period of recuperation during which the samples were permitted to return to their initial resistance in a dry air environment. Measurements were taken every five seconds. The initial resistance of the NWs typically fell within the range of 12 kΩ to 25 kΩ. The findings of this study are presented in Figure 3.8, which summarizes the performance of both devices. Both devices exhibited a remarkable response to exposure to humidity, with normalized resistance plotted against time.

During each sensing cycle, we noticed a rise in the device's resistance when it was exposed to humidity, which was then followed by a decrease in resistance back to the initial value during the recovery phase (by flushing with dry air). Furthermore, it was observed that the highest resistance value in each sensing cycle rose with the RH value. Interestingly, our results demonstrated that the NWs were sensitive to RH, even at low concentrations of 10%. Before reaching a relative humidity (RH) of 30%, both nanowires exhibited nearly identical resistance responses. However, as the RH exceeded 40%, a distinct deviation was observed. Specifically, the relative response of $NW1$ began to amplify compared to that of $NW2$. By the culmination of the test at an RH of 70%, the differential in relative response had increased approximately 1.4 times. Concurrently, it is noteworthy that the noise associated with the $NW1$ also intensified. An in-depth analysis of the resistance noise will be undertaken in the discussion section.

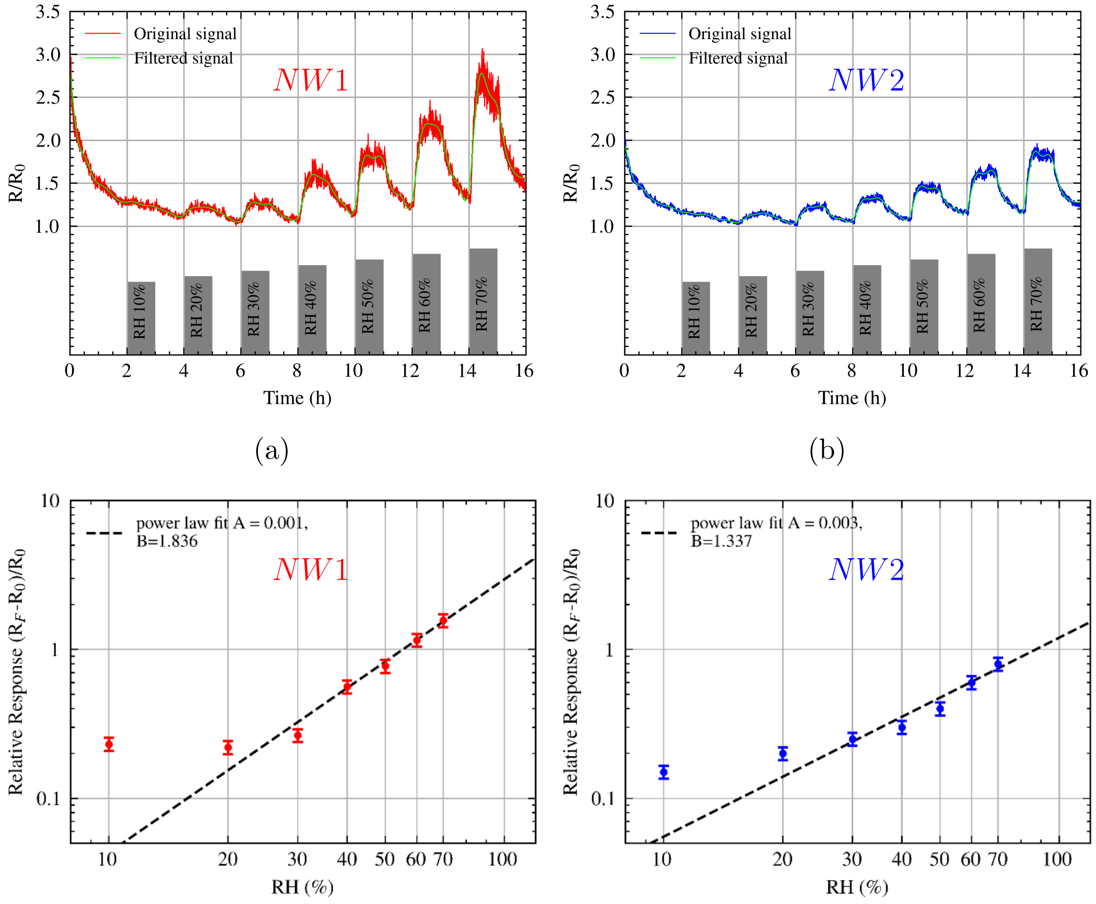

(a) (b)

(c) (d)

Figure 3.8: Variation in the normalized resistances of NWs in response to changes in relative humidity from 10% to 70%. The figures show the variations for $NW1$ (a) and $NW2$ (b), along with their respective calibration curves for $NW1$ (c) and $NW2$ (d). For both signals, a 5th-order digital Butterworth filter was applied with a cutoff frequency of 1/400 Hz. This filter attenuates fluctuations in signals with a period shorter than 400 seconds.

3.4.2 Sensitivity and Performance of the Nanowires in NO_2 Detection

In Figure 3.9, we present the results of the sensing tests with NO_2 for both devices, with concentrations ranging from 2-9 ppm in 1 ppm increments.

To carry out the sensing experiments for NO_2, a procedure was implemented involving a 2-hour exposure phase where the sensors were subjected to a steady and defined concentration of NO_2, succeeded by a 2-hour recovery phase for the samples to revert to their original resistance in dry air. Both devices demonstrated a noticeable sensitivity to NO_2, even at minimal tested concentrations. Notably,

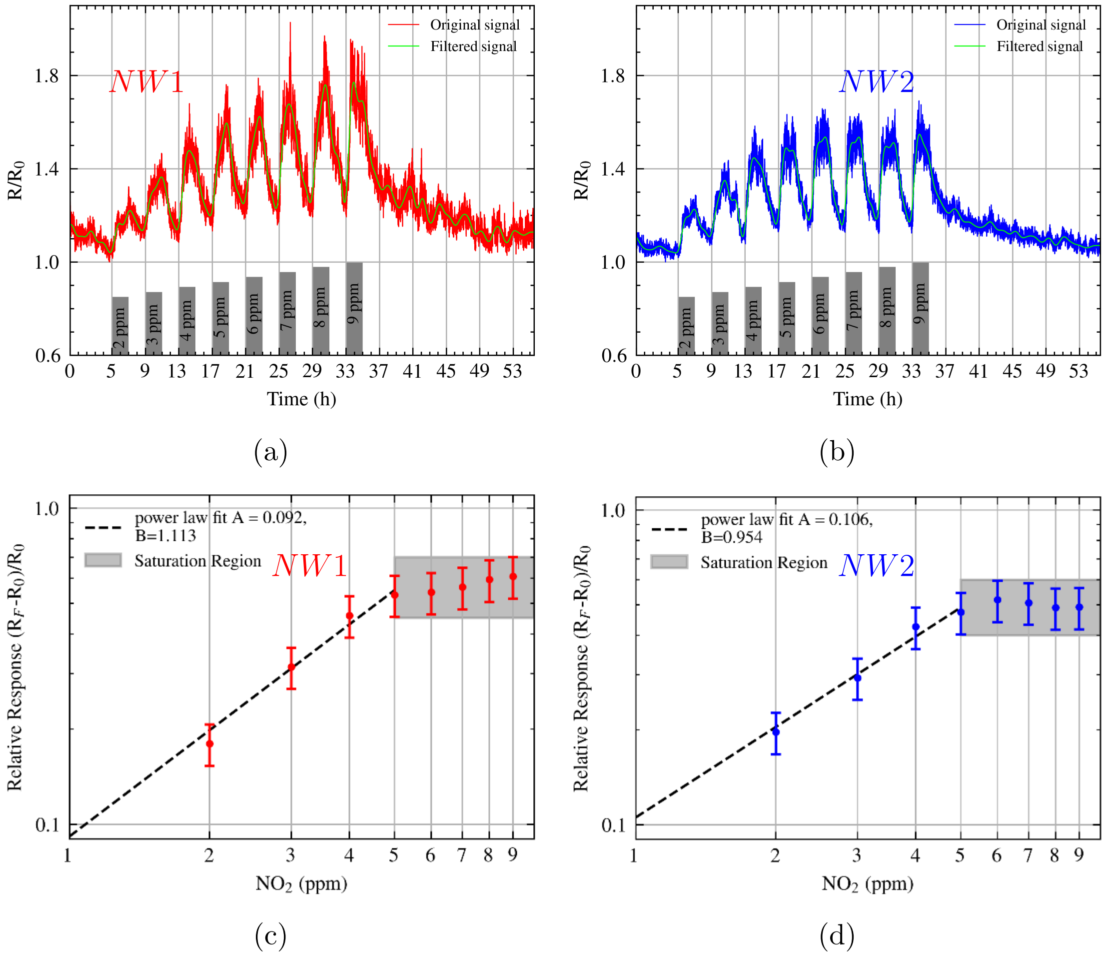

(a) (b)

(c) (d)

Figure 3.9: Dynamic response of normalized NW resistances to changes in NO_2 from 2 to 9 ppm. The figures show the variations for $NW1$ (a) and $NW2$ (b), along with their respective calibration curves for $NW1$ (c) and $NW2$ (d). For both signals, a 5th-order digital Butterworth filter was applied with a cutoff frequency of 1/900 Hz. This filter attenuates fluctuations in the signals with a period of less than 900 seconds.

$NW1$ showed a greater response to NO_2 compared to $NW2$, especially when the concentration surpassed 4 ppm. At levels above 5 ppm, both $NW1$ and $NW2$ exhibited saturation in response. It is significant to mention that the exposure cycle to NO_2 was double the duration of the RH testing cycle, yet a stable steady-state response was not observed in the NO_2 tests. This lack of a stable response might stem from the specific characteristics of NO_2 and its interaction with the NWs, leading to a more intricate dynamic response compared to RH. Consequently, the recovery period was extended to 2 hours to ensure complete reversal of the NWs to their baseline resistance in dry air. In each testing cycle, a temporary resistance increase was noticed when the device encountered humidity and NO_2, followed by a reduction to baseline resistance during the recovery phase, which involved the circulation of dry air. In contrast to metal oxide nanowires, which require high operating temperatures or UV desorption at ambient conditions for gas molecule removal [62, 64], our NWs were capable of releasing NO_2 molecules solely via air flushing under similar conditions. Moreover, minor variations in the response of the nanowires were observed, which could be attributed to differences in their geometric properties.

3.4.3 Noise Analysis of Nanowires Response

The noise analysis of NWs response was carried out by the research group of The Scuola Normale Superiore of Pisa.

Comparative Analysis of NWs Responses to Environmental Stimuli

In our investigation of the responses of nanowire-based sensors to environmental stimuli, we observed distinct behaviors in the resistance and conductance measurements when exposed to RH and NO_2. Here, we present a comparative analysis that integrates both the resistance and conductance responses to these analytes. As shown in Figures 3.10a and 3.10b, both $NW1$ and $NW2$ exhibit periodic resistance fluctuations with exposure to RH and NO_2, reflecting dynamic adsorption and desorption processes. In particular, the curves depicting the approximation of standard deviation versus resistance values exhibit pronounced nonlinearity, especially for $NW1$ under NO_2 exposure, as illustrated in Figure 3.10c. On the contrary, the conductance measurements, which are the inverse of resistance, display a more linear relationship with the predicted values of our model, as demonstrated in Figure 3.10d. Therefore, for analysis of the dynamics of gas reactions with each injection, the transition from resistance representation to conductance is advantageous because of the linear behavior observed in the standard deviation approximation curves. This linearity in conductance under varying conditions underscores its potential as a reliable metric for gas-sensing applications.

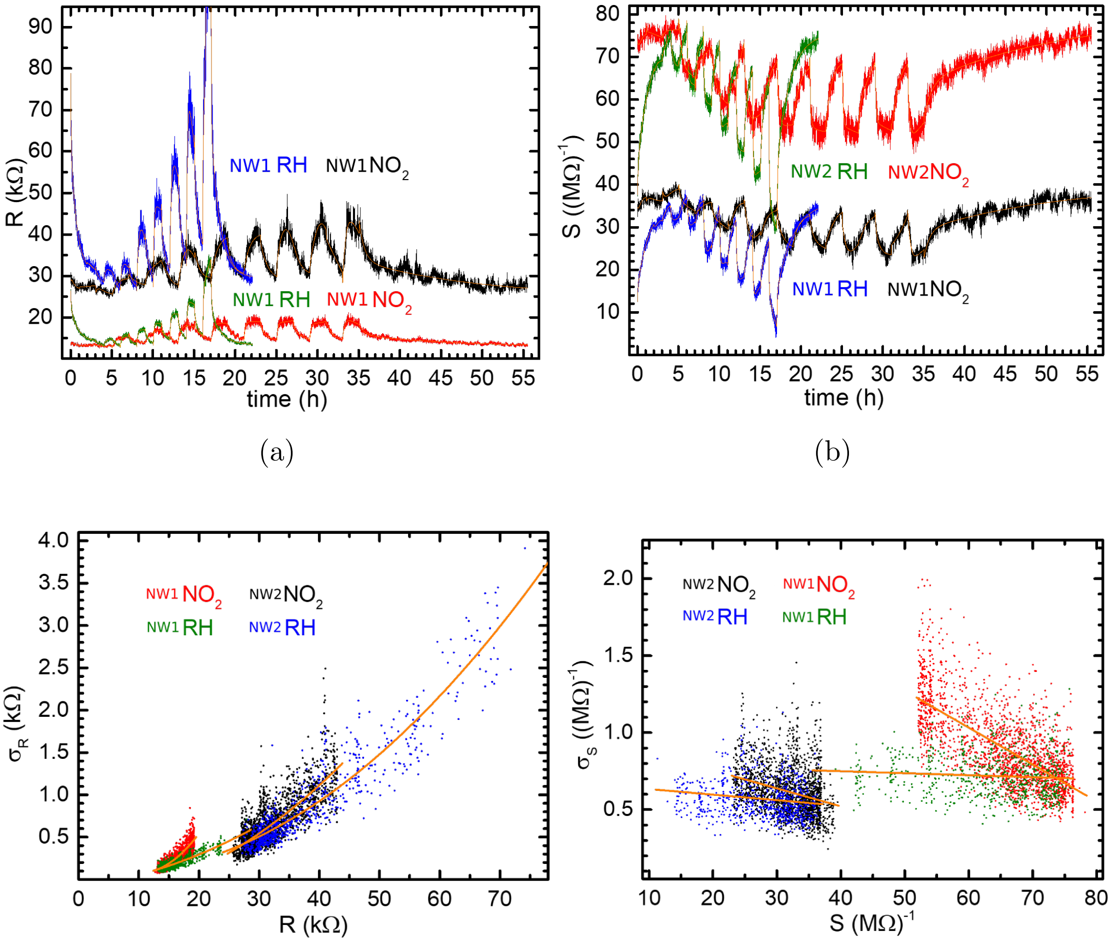

(a) (b)

(c) (d)

Figure 3.10: Comparative analysis of resistance and conductance in NW sensors. (a) - Resistance (R) and (b) - Conductance S as a function of time; in orange, biexponential fit for each period of filling or emptying the chamber. (c) Resistance standard deviation (σ_R) of the fit residuals, calculated every 20 points in 40-point windows (corresponding to 3.3 min) within each filling or emptying period, as a function of the (fitted) value of the resistance; orange lines are a guide for the eyes, obtained by parabolic fits. (d) - Conductance standard deviation (σ_S) of the fit residuals, calculated every 20 points in 40-point windows (corresponding to 3.3 min) within each filling or emptying period, as a function of the (fitted) value of the conductance; orange lines are derived from linear fits.

.

Correlation Analysis of Sensor Signals

In the following subsection, we analyze the autocorrelation (AC) and cross-correlation (CC) of the sensor signals from $NW1$ and $NW2$, focusing on their conductance response to NO_2 and RH. Figure 3.11 provides a visual representation of this correlation analysis through a series of subfigures, each elucidating different aspects of the sensor responses.

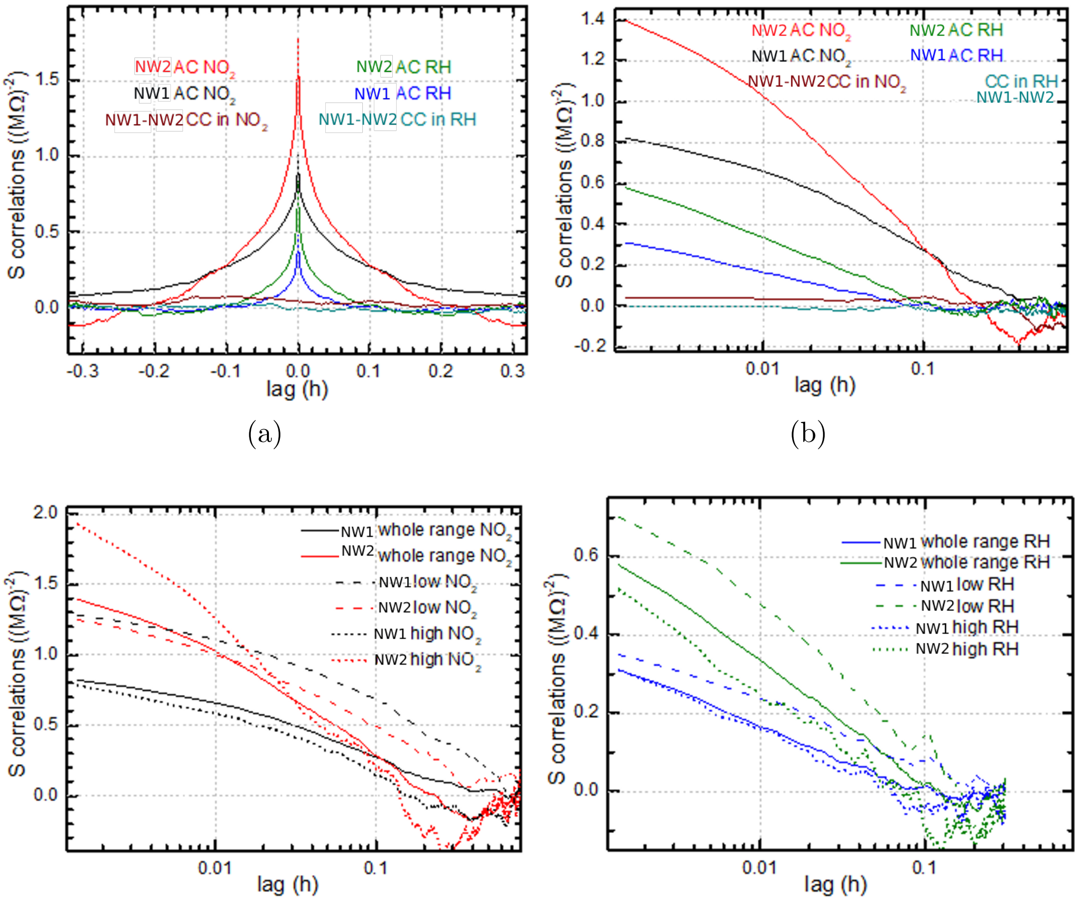

(a) (b)

(c) (d)

Figure 3.11: Comprehensive correlation analysis of $NW1$ and $NW2$ sensor signals for NO_2 and RH; (a) Full scale AC and CC for RH and NO_2; (b) Detailed analysis at short time lags; the AC and CC curves are shown for the different devices and situations;they have been calculated within each filling/emptying period and then mediated;(c) Response to NO_2 exposure; low NO_2 corresponds to times above 37.27 hours, high NO_2 corresponds to times 13.5-15, 17.5-19, 21.5-23, 25.5-27, 29.5-31, 33.5-35 h ;(d) Response to RH exposure;low RH corresponds to times above 17.79 h, high RH to times 10.57-11.04, 12.58-13.05, 14.58-15.06 h.

Figure 3.11a illustrates the comparative conductance analysis, where both $NW1$ and $NW2$ demonstrate a robust AC for NO_2, indicative of their sensitivity to this gas. In particular, AC is more pronounced for $NW2$, suggesting a higher stability or a more consistent response to NO_2 concentrations. This characteristic is paramount in ensuring reliable sensor performance, particularly for applications that require precise detection of pollutant levels over short periods.

In contrast, as seen in Figure 3.11b, the AC for RH is lower, implying that the immediate response of the sensors to changes in humidity is moderate. This difference in AC between NO_2 and RH is crucial for applications where the distinct detection of either parameter is necessary. For instance, in environments where both NO_2 and RH are present, the higher AC for NO_2 implies that $NW1$ and $NW2$ can more reliably report changes in NO_2 concentrations without significant interference from RH fluctuations.

In the case of NO_2, evident from Figure 3.11c, there is a notable disparity between $NW1$ and $NW2$ in their conductance correlation, particularly at higher NO_2 concentrations. This discrepancy could be indicative of intrinsic differences between the NWs, such as variations in surface properties or differential sensitivity to NO_2, which merits further investigation.

In contrast, as shown in Figure 3.11d, the conductance correlations for exposure to RH decrease more rapidly than for NO_2, and the distinction between low and high RH is less stark. The faster decay rate suggests a more transient impact of humidity on conductance, implying a less persistent effect compared to NO_2. Such observations are critical for understanding the temporal dynamics of nanowire-based sensor responses and can guide the optimization of sensor calibration protocols for environmental monitoring applications.

In summary, the comprehensive correlation analysis underscores the nuanced response of $NW1$ and $NW2$ to NO_2 and RH, as visualized in the subfigures of Figure 3.11. The superior AC for NO_2 across both $NW1$ and $NW2$ implies a strong suitability for NO_2 sensing applications, while the distinct CC patterns suggest potential for spatial distribution analysis of NO_2 levels. The temporal decay in AC for both NO_2 and RH emphasizes the importance of monitoring time lags when interpreting sensor data, and the concentration-dependent differences in the conductance response highlight the need for careful calibration and analysis in varied environmental conditions.

Chapter 4

Agricultural Enhancement Data Acquisition System for Root Temperature Analysis in Basil Growth

4.1 Introduction

In this section, we investigate the creation of a new electrical system designed for advanced control of greenhouse environments. This project highlights the growing area of precision agriculture, and our main focus is on growing basil hydroponically. The key reason for this work is to overcome the shortcomings of existing greenhouse monitoring systems. These systems often only record air temperature [96, 97], ignoring the possibility of noticeable temperature differences in various parts of a greenhouse. A crucial aspect of this project is monitoring the temperature of the root zone temperature (RZT) of basil plants, which addresses this critical gap in existing greenhouse monitoring systems. Additionally, the use of LoRaWAN (Long Range Wide Area Network) in our system plays a crucial role. This technology allows us to transmit data from multiple sensors in the greenhouse efficiently and reliably [98, 99]. With LoRaWAN, we can collect detailed information on RZT from different areas within a greenhouse. This capability is vital to ensure uniform growth conditions and identify areas that require specific attention, thus enhancing the overall effectiveness of our precision agriculture practices. The idea of the project is a joint proposal of the project is a joint proposal of Antares Vision Ltd.

and Humans Garden agricultural organization.

4.2 The Importance of Root Zone Temperature Measurement in Plant Growth

RZT significantly influences plant growth and development, particularly in controlled environments such as hydroponic systems. Although air temperature has been a traditional focus in agriculture, recent studies highlight the importance of RZT in influencing plant physiology. In hydroponic systems, RZT affects the uptake of nutrients, photosynthesis, transpiration, and overall plant health [100, 101]. Plant growth is intricately related to their root environment. Higher root temperatures can accelerate metabolic processes, leading to increased nutrient uptake, improved transpiration, and faster growth. On the contrary, lower root temperatures may slow down these processes, potentially stunting plant development [102, 103]. For example, heating the root zones in tomatoes and spinach has shown positive effects on their growth, due to increased metabolism [104].

Basil (*Ocimum basilicum* L.), a plant native to tropical and subtropical regions, thrives at high temperatures and under light conditions [105, 106]. In hydroponic cultivation, control over RZT is crucial. A study carried out with various types of basil varieties in hydroponic setups found that water temperatures of 27.5 °C and 31 °C resulted in better growth compared to 23 °C, indicating the importance of maintaining optimal RZT for basil [107].

This research also revealed significant interactions between cultivar types and water temperature on growth parameters such as leaf number and dry weight of the roots, underlining the need to tailor RZT for specific basil varieties [107]. For example, cultivars like 'Cinnamon' and 'Sweet Thai' showed better leaf production at higher water temperatures, emphasizing the need for precise management of RZT in hydroponic basil cultivation.

Hydroponic systems offer an advantage in precisely controlling environmental variables such as water temperature, directly influencing RZT [108]. By optimizing RZT, hydroponic growers can not only enhance plant growth, but also potentially conserve energy and mitigate adverse climatic effects on agriculture [109].

Measurement of root temperature is vital for plant growth, especially in hydroponic systems. Understanding and controlling RZT can lead to significant improvements in plant health and yield, as demonstrated in the case of basil. With the advancement of hydroponic technologies, the precise control of these environmental factors becomes increasingly feasible, opening new avenues for efficient and sustainable agricultural practices.

4.3 Comparison of Temperature Measurement Methods in Hydroponics

The selected requirements for temperature measurement in hydroponics are driven by the essential needs of the system. High precision ($\pm 0.5°C$) is vital for optimal nutrient uptake and plant growth, as small temperature deviations can significantly affect plant health. A broad operating temperature range (20-40 degrees Celsius) accommodates the diverse temperature needs of the plants. Resilience in diverse pH environments is critical due to fluctuations in the pH levels of nutrient solutions and plant secretions.

Figure 4.1: The greenhouse for basil was set at Humans Garden. On the top one may see the bottom part of the movable rolling bench with the roots. On the bottom there is a stationary tray with the slots which supply the roots with water and nutrients.

Ultimately, facilitation of movement within a greenhouse is crucial, given the necessity to maneuver rolling benches and the various dimensions and configurations of hydroponic systems (Figure 4.1).

Thermocouples align well with these requirements (Table 4.1).

Method	Advantages	Disadvantages
Thermocouples and Thermistors [110]	- High precision - Wide temperature range - Durable in harsh environments	- Requires complex electronics - Susceptible to noise
Infrared Thermometers [111]	- Non-contact measurement - Compact and easy to use - Versatile	- Only measures surface temperature - Affected by environment - Can be expensive
Liquid Crystal Temperature Strips [112]	- Visual readout - Reusable - Sensitive to small changes	- Cannot be used in moisturized environment - Affected by external conditions - Interpretation required

Table 4.1: Comparison of temperature measurement methods in hydroponics

Their precision and wide temperature range are suitable for the sensitive balance required in hydroponics. Although thermocouples and thermistors require complex electronics and are susceptible to noise interference, these complexities can be effectively managed by employing specialized digital integrated circuits. This approach not only streamlines their operation but also enhances their practicality for application in hydroponic systems.

4.4 Scheme Components Selection

4.4.1 Selection of Thermocouple Sensor

For precise temperature monitoring in a hydroponic greenhouse, the SparkFun DS18B20 waterproof digital temperature sensor is identified as the most suitable choice. This sensor is chosen for its unique combination of features that meet the demanding conditions of hydroponic environments [113].

The DS18B20 sensor is a programmable digital temperature sensor known for its precision and versatility. It operates within a temperature range of -55°C to

+125°C and offers an accuracy of ±0.5°C, which is ideal for the precise control required in hydroponics;. Its digital output eliminates the issues of signal degradation over long distances, a common challenge in expansive greenhouse settings. Another distinguishing feature of the DS18B20 is its waterproof design, which makes it highly suitable for humid and wet conditions that often occur in hydroponic systems. The sensor is encased in a stainless steel tube, providing robust protection, ensuring longevity under a variety of environmental conditions, and fitting in the slot of the stationary tray (Figure 4.1), including those with various pH levels due to fertilizers and nutrient solutions. (Figure 4.2)

Figure 4.2: The SparkFun Waterproof DS18B20 Digital Temperature Sensor with a waterproof case.

The sensor's 1-Wire interface simplifies connectivity, requiring only one digital pin for communication, which is a significant advantage in setups where multiple sensors are needed. This feature, combined with its ability to measure temperatures accurately in harsh environments, makes the DS18B20 an optimal choice for hydroponics applications where precise and reliable temperature monitoring is critical.

Given these attributes, the SparkFun DS18B20 waterproof digital temperature sensor presents itself as an ideal candidate for effective temperature monitoring in a hydroponic greenhouse, aligning seamlessly with the requirements of high precision, operational resilience, and adaptability.

4.4.2 Selection of the Battery Supply System

For an autonomous hydroponic greenhouse system that requires high mobility, the power supply is a critical component. The selection of 18650 lithium-ion rechargeable batteries is made on the basis of their high energy density, allowing considerable energy storage relative to their size, which is crucial for portability [114]. The versatility of these batteries for use on a multitude of devices makes them ideal for a scalable hydroponics setup. Their durability, with proper care lasting several years, aligns with the long-term sustainability goals of autonomous hydroponic systems. The nominal voltage of around 3.7V and capacity ranging from 1800mAh to 3500mAh are well-suited to the power demands of portable temperature sensors such as the DS18B20 [113, 114].

Moreover, these batteries have the capability to undergo multiple charge-discharge cycles without experiencing a notable decrease in capacity, guaranteeing steady performance.

4.4.3 Selection of Microcontroller Board

Arduino MKR WAN 1310 is chosen as the microcontroller for our hydroponic greenhouse system due to its LoRa connectivity, low power consumption, and battery operability [115]. Equipped with the Arm Cortex-M0+ 32-bit SAMD21 microcontroller and the Murata CMWX1ZZABZ module, it offers a balance between performance and power efficiency.

LoRaWAN allows MKR WAN 1310 to communicate efficiently over long distances in remote areas, making it ideal for expansive greenhouse environments. The board can connect to various networks, including The Things Network, providing flexibility in network management.

Technical specifications such as operating voltage of 3.3V, support for a single cell Li-Po battery, and minimum power consumption of 104uA make the MKR WAN 1310 particularly suited for battery-powered operations, allowing the hydroponic system to remain autonomous and mobile.

4.5 Designing the Electrical Framework and Housing design

4.5.1 Detailed PCB Layout and Design of the Temperature Sensors Board and Battery Voltage Measurement

The PCB designed for integration with the MKR1310 [115], hereafter in this chapter referred to as the 'MCU', functions as a foundational interface for the system. The board is meticulously engineered to incorporate two critical subsystems:

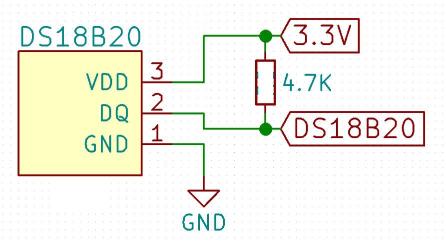

Figure 4.3: Pull-up resistor circuit for DS18B20 sensor

1. A specialized pull-up resistor circuit is established for the DS18B20 temperature sensor, ensuring reliable communication with the MCU and consequently precise temperature readings [113]. Refer to Figure 4.3 for the circuit layout.
2. A voltage divider circuit is integrated to accommodate the battery voltage, which may exceed the MCU's ADC input threshold of 3.3V [114, 115] . This inclusion is crucial to maintain the voltage input to the MCU within safe operating limits, protecting the system from overvoltage damage [115]. Figure 4.4 illustrates this protective circuit.

The integration of these subsystems is indicative of the role of the PCB in facilitating accurate data collection and enhancing the durability of the system. In the progression from design to implementation, a specialized PCB was developed to house the DS18B20 temperature sensor's pull-up resistor configuration alongside the MCU's voltage divider circuit. The PCB fabrication employed a precision milling machine to ensure precision in the board construction. Subsequent to the milling process, the components were soldered, culminating in a durable and effective integration of both subsystems.

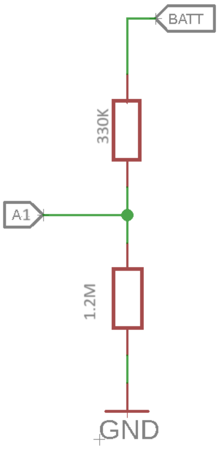

Figure 4.4: Voltage divider circuit for MCU's protection

The following figures illustrate the design and physical realization of the PCB. Figure 4.5a displays the 3D model, while Figure 4.5b provides a visual of the actual PCB post-assembly.

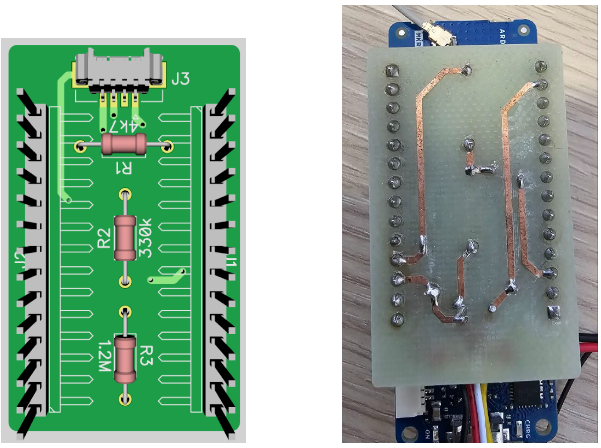

(a) 3D model of the PCB

(b) Photo of the actual PCB

Figure 4.5: Design and realization of the PCB

4.5.2 Electrical Interconnections and Wiring

The data acquisition system for greenhouse monitoring has been meticulously engineered, with component selection customized to meet the unique demands of such environments.

The core of the temperature monitoring functionality is the DS18B20 sensor. This digital probe, encapsulated to withstand wet conditions, is integral for assessing the moisture-rich root zones typical in greenhouses. It transmits temperature readings from 9 to 12 bits through a 1-Wire interface, a design that maintains accuracy irrespective of wire length.

The system is powered by a dual Li-ion battery configuration. This choice was driven by the necessity for mobility within the greenhouse, where fixed power sources could hinder operational flexibility.

Wireless data transfer is facilitated via an MCU equipped with a LoRaWAN module. LoRaWAN was selected for its long-range communication capabilities, vital for sprawling greenhouse structures. This technology supports multiple devices on a single network, enhancing the system's scalability. The limited data requirements, focusing on temperature and battery status, negate the need for higher bandwidth solutions like 3G or 4G, which would additionally incur greater costs.

The layout of the system, shown in Figure 4.6, illustrates the strategic integration of components. The DS18B20 RZT sensors interface with the MCU via a custom PCB (Figure 4.5b). A solar panel feeds into the battery charger, which in turn connects to the Li-ion batteries, thus streamlining the energy conversion and storage process. The MCU derives its power from this charger. An adhesive-mounted pentaband antenna, connected to the LoRaWAN module, ensures optimal communication with the central LoRaWAN gateway.

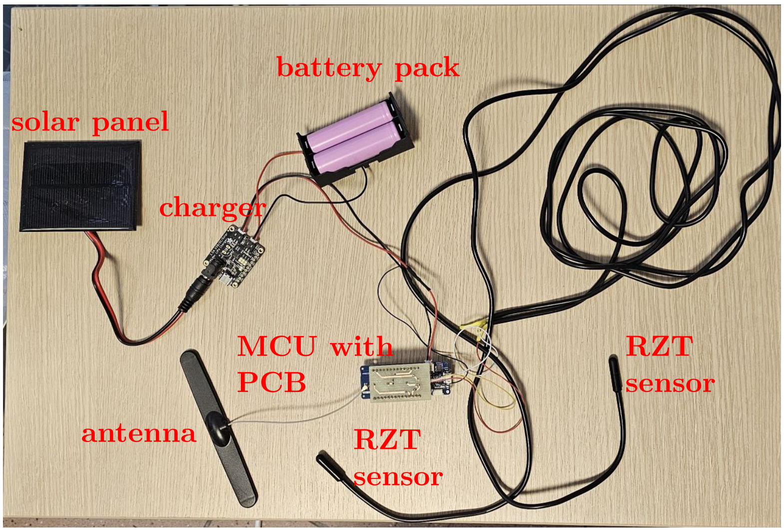

Figure 4.6: Photo of the system components, highlighting the MCU, RZT sensors, solar panel setup, and the LoRaWAN antenna integration

4.5.3 Development of the 3D Model of the Setup

A detailed 3D model of the hydroponic monitoring system was constructed using SolidWorks to serve as a visual aid and to facilitate understanding of the system's design. This model provides a comprehensive visualization of the system's components and their configuration, highlighting the integration of the solar panel, charger, battery, and the robust RZT sensor, all designed for the demanding conditions of hydroponic agriculture.

Figure 4.7a presents the system from a perspective that emphasizes the placement of the solar panel,which is located to maximize sunlight above the plants, and the battery charger that powers the system. In addition to the blue box, the MCU with PCB will be located. All electronics will be encapsulated in a waterproof case to protect from the humid environment of the hydroponic greenhouse and water.

Figure 4.7b offers a different point of view, showing the proximity of the RZT sensor (shown in red) within the slot of the stationary tray, where nutrients and water pass and the roots of plants are located. By situating the sensor here, the system can capture the most relevant temperature data, which is essential for the careful regulation of the hydroponic environment.

The figures collectively illustrate the system's practicality, its suitability for hydroponic applications, and the ease with which it can be adapted to different greenhouse layouts. This 3D model serves as an instrumental blueprint for visualizing the operational setup within a real-world context.

4.6 Development of Firmware and Integration of Data Transmission Systems: Bridging LoRaWAN with AWS

4.6.1 Firmware Design and Sensor Integration

The chosen MCU is engineered to meet the demands of IoT applications, featuring an integrated LoRaWAN module. This integration promotes efficient design, eliminating the need for additional components, and streamlining the design process.

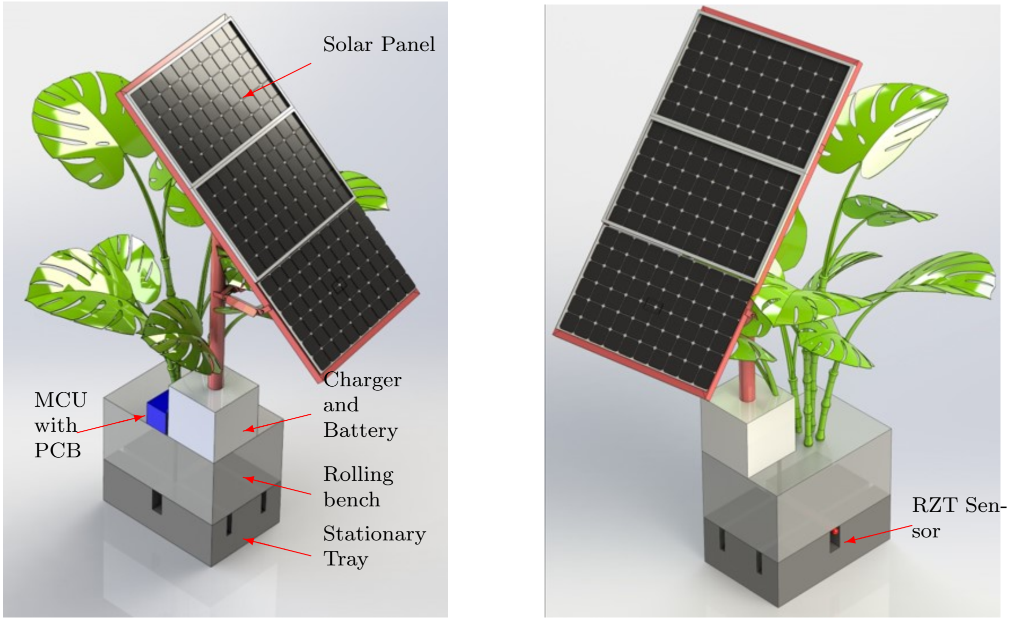

(a) 3D model of the system: first view

(b) 3D model of the system: second view

Figure 4.7: 3D model of the system displaying the location of the developed system in the greenhouse environment

Its compatibility with the extensive Arduino library ecosystem is another significant benefit, offering developers a wealth of existing resources to accelerate the development cycle.

Within our greenhouse data acquisition system, the MCU's built-in LoRa connectivity is essential for long-range communication required in the spacious greenhouse environment. The design accommodates easy battery connection, ensuring continuous operation.

Firmware development was conducted using Visual Studio Code and PlatformIO, providing a complete platform for efficient programming, testing, and debugging. This suite improved development efficiency, vital for integrating RZT DS18B20 sensors and optimizing power usage. The MCU's functionality was crucial for precise data collection and energy efficiency, aligning with the project's objectives. The algorithm defined in Algorithm 1 encapsulates the essential stages of data acquisition and transmission for the greenhouse monitoring system. Cayenne Low Power Payload (CayenneLPP) is utilized to efficiently encode sensor data, which is crucial for low-bandwidth LoRaWAN communication [116]. Entering sleep mode is a critical power saving strategy that minimizes energy consumption during pe-

Algorithm 1 Data Acquisition and Transmission Process

```
Initialize system peripherals and LoRaWAN module
Attach wake-up interrupt for Real-Time Clock alarm
Initialize temperature sensors
Connect to LoRaWAN network using Over-The-Air Activation
Configure system for data transmission
loop
    Acquire temperature data from sensors
    Read battery voltage through analog input
    Package data for transmission using CayenneLPP format
    Transmit data packet over LoRaWAN
    Enter sleep mode to conserve energy
end loop
```

riods of inactivity. This is particularly important for battery-operated systems in remote locations. Temperature data acquisition is executed by reading from sensors specifically calibrated for the hydroponic environment's conditions. The Real-Time Clock (RTC) is instrumental in timing events, allowing for periodic data collection and transmission, thereby maintaining a current overview of the greenhouse's environmental conditions. The full firmware code can be found in Appendix A.4.

4.6.2 Selection of The Things Network Stack for LoRaWAN Integration

After the development of the MCU firmware, the subsequent critical step was integration with a competent LoRaWAN platform, for which TTN Stack was selected. This decision was based on regional compatibility, cost considerations, data transmission requirements, scalability, and community support.

TTN's compatibility with European LoRaWAN frequencies ensures seamless communication in line with regional standards. Its open-source, cost-effective framework supports the financial constraints of the research. With the firmware's data transmission interval set at one minute, TTN's infrastructure aptly supports this frequency, avoiding network overload.

The scalability of the TTN allows for potential future enhancements of the firmware and system. Additionally, the TTN community provides a valuable repository of knowledge and support, contributing to the firmware's successful real-world application. The integration into TTN Stack thus reflects a strategic alignment with the firmware's design and research objectives.

4.6.3 Transmission of Data to The Things Network Stack

The phase following firmware refinement involved transmitting data to TTN Stack. The data payload included two temperature readings and battery voltage, encoded using the CayenneLPP format, optimized for the low-bandwidth LoRaWAN protocol.

The TTN console provides a transparent view of the data traffic (Figure 4.8), allowing for real-time monitoring. The console displays each device's data with unique identifiers, such as eui-a8610a3339306210 for the device in question.

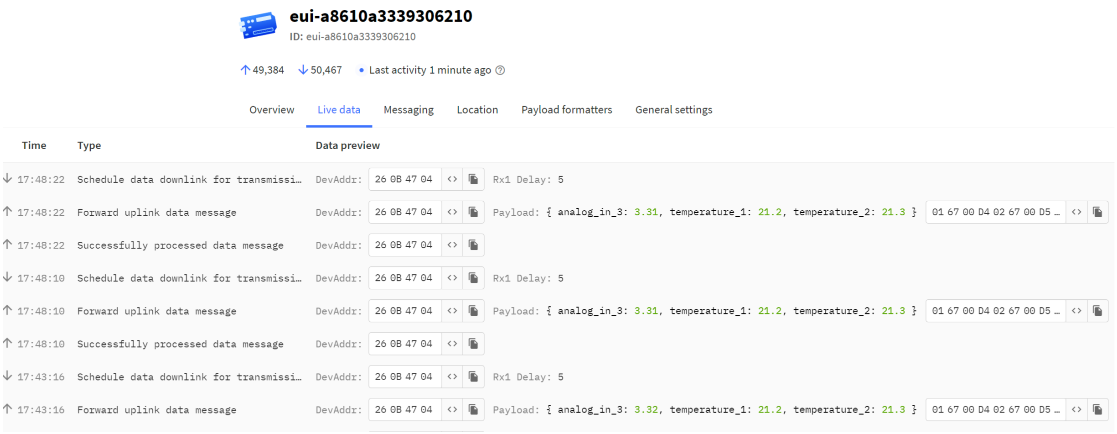

eui-a8610a3339306210
ID: eui-a8610a3339306210

↑ 49,384 ↓ 50,467 • Last activity 1 minute ago

Time	Type	Data preview
↓ 17:48:22	Schedule data downlink for transmissi…	DevAddr: 26 0B 47 04 Rx1 Delay: 5
↑ 17:48:22	Forward uplink data message	DevAddr: 26 0B 47 04 Payload: { analog_in_3: 3.31, temperature_1: 21.2, temperature_2: 21.3 } 01 67 00 D4 02 67 00 D5 …
↑ 17:48:22	Successfully processed data message	DevAddr: 26 0B 47 04
↓ 17:48:10	Schedule data downlink for transmissi…	DevAddr: 26 0B 47 04 Rx1 Delay: 5
↑ 17:48:10	Forward uplink data message	DevAddr: 26 0B 47 04 Payload: { analog_in_3: 3.31, temperature_1: 21.2, temperature_2: 21.3 } 01 67 00 D4 02 67 00 D5 …
↑ 17:48:10	Successfully processed data message	DevAddr: 26 0B 47 04
↓ 17:43:16	Schedule data downlink for transmissi…	DevAddr: 26 0B 47 04 Rx1 Delay: 5
↑ 17:43:16	Forward uplink data message	DevAddr: 26 0B 47 04 Payload: { analog_in_3: 3.32, temperature_1: 21.2, temperature_2: 21.3 } 01 67 00 D4 02 67 00 D5 …

Figure 4.8: The Things Network console showing live data transmission.

Key aspects of the data packets include:

- **Device Address (DevAddr)**: A unique network identifier for the device.
- **Payload**: Contains the actual data in binary format, arranged according to CayenneLPP standards.

The instant data visualization of the console is crucial for monitoring system performance and rapidly detecting irregularities, thereby maintaining the system's dependability and data accuracy.

4.6.4 Integration with Amazon Web Services IoT

The selection of AWS IoT for cloud integration was made after careful consideration of its extensive features and integration capabilities within the AWS suite. AWS IoT offers a secure, scalable, and reliable infrastructure, which is critical for the project's cloud-based operations. Its compatibility with other AWS services facilitates efficient data handling and analytics. The global infrastructure of AWS ensures reliable performance and minimal latency, which is vital for real-time data analysis. The strong security measures and flexibility of the platform in various IoT applications further affirmed its choice for this research.

The connection between TTN and AWS IoT was systematically structured. Initially, Application ID and Access Key from TTN were obtained, facilitating an authenticated link. Concurrently, a 'thing' in AWS IoT Core was created to represent the TTN data source.

Critical to this setup were the AWS IoT rules formulated to process incoming TTN messages and to direct them appropriately. This setup enabled data routing to services like AWS DynamoDB for storage or triggering AWS Lambda functions for data processing.

The integration was operationalized through the TTN dashboard, linking to AWS using the necessary credentials. This ensured secure and timely data flow from TTN to AWS IoT.

Following this, AWS Timestream was incorporated for conducting real-time analytics with Grafana (Figure 4.9), providing advanced data visualization. DynamoDB served as the primary data storage, with AWS S3 used for periodic data backups. Throughout this process, ongoing validation was prioritized to maintain data integrity and optimize data transmission. This approach reinforced the system's reliability, making it well-suited for the project's requirements.

The integration also lays the foundation for utilizing machine learning within AWS, leveraging Amazon SageMaker to analyze temperature data and predict environmental changes in the greenhouse. This capability is vital for proactive management and optimizing plant growth conditions.

Figure 4.9: Grafana dashboard showing battery and temperature sensor readings

4.6.5 Complete Network Architecture

As depicted in Figure 4.10, the LoRaWAN network architecture for this study is designed to facilitate data transmission from the nodes to the TTN. Nodes collect vital parameters such as battery voltage and temperature readings, transmitting this information via LoRaWAN gateway to the TTN using the TCP/IP protocol.

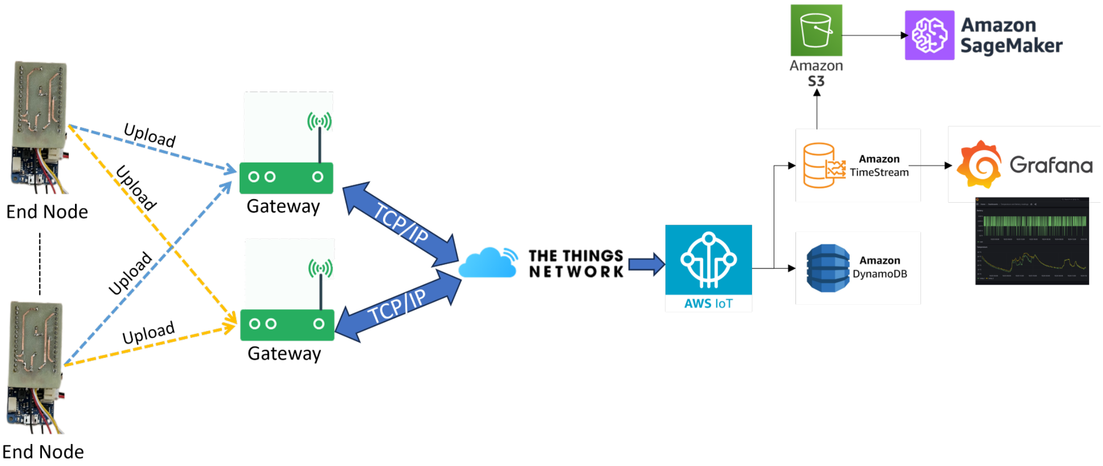

Figure 4.10: Overview of the system architecture showing data flow from LoRaWAN nodes to AWS IoT services.

Post-reception, TTN forwards the data to various AWS IoT services for processing and storage. AWS DynamoDB manages the incoming data, while AWS Timestream archives time-series data. Visualization of this data is conducted through Grafana, offering insightful real-time analysis. The integration of Amazon S3 provides a robust solution for long-term data storage, and Amazon SageMaker offers advanced machine learning capabilities to process and analyze the data further. This comprehensive setup ensures efficient data handling from collection to actionable insights.

4.6.6 Future Perspective

This chapter has detailed the initial efforts towards creating the system that will be able to predict the dependence between RZT and plant growth. Through our collaboration with Orobix Srl, we have begun to lay the groundwork for applying machine learning to predict plant growth responses to RZT variations. At this stage, our collaborative aim is to prepare for the application of machine learning by first gathering essential data through field testing. The anticipated field tests mark a significant step towards our objective of developing a model that can accurately forecast plant growth based on RZT, laying a foundation for future advancements in agricultural practices through predictive modeling. This study paves the way for advancements in agricultural technology, with substantial potential for sustainable and efficient farming methods. Key areas for future exploration include crop diversification, extensive field studies, enhanced sensing with additional environmental sensors, machine learning interpretation for data analysis, and economic feasibility assessment. The developed sensor underwent testing in lab facilities before being delivered to Orobix. At Orobix, a robust 3D-printed case was constructed to protect the sensor for external use. This versatile device can now be deployed not only in greenhouses, but also in open-air facilities such as vineyards, assisted by solar panels.

Chapter 5

Conclusions

Data acquisition system for sensing food spoilage

In the development of a specialized device to monitor the spoilage of protein-rich foods, this study has successfully integrated the novel sensor geometry with advanced material technology. The use of cellulose as a sensitive layer for PEGS sensors marks a significant departure from conventional methods in which paper serves only as a substrate for a sensitive layer, which presents an eco-friendly and cost-effective alternative. This shift not only addresses environmental concerns, but also opens up new avenues in the field of sensor technology.

The experimental findings in this chapter strongly support the theoretical models formulated earlier. In particular, the enhanced resistance response of the newly designed PEGS sensors under high humidity conditions, as predicted by the conformal mapping techniques, was empirically validated. This alignment between theoretical predictions and experimental results underlines the accuracy of the model and the effectiveness of geometric optimization in sensor design. The observed differences in performance between the original and optimized sensor designs highlight the critical role of geometric parameters in determining sensor responsiveness, especially in environments with high moisture content.

Integration of NFC technology in this project represents a significant advancement in the application of PEGS sensors. The use of NFC for both data communication and power supply not only aligns with modern IoT trends but also enhances the system's sustainability by eliminating the need for batteries.

A crucial aspect of this research lies in its application to real-world scenarios, particularly in the detection of food spoilage. The experimental results demonstrate the sensor's ability to distinguish between simple environmental changes, such as humidity, and the specific conditions associated with food spoilage. This distinction is important in validating the practical utility of the sensor. The correlation between changes in sensor resistance and microbiological indicators of spoilage, such as CFU growth, further reinforces the sensor's potential in real-time monitoring of food quality.

However, it is important to recognize the limitations of this study. While promising, research has been limited to certain conditions and a specific type of food product. Extending these findings across a diverse range of food products and spoilage conditions remains an area for future exploration. In addition, integrating these sensors with consumer-friendly technologies, such as mobile applications, could significantly enhance their practicality in daily use.

Comparative Analysis of Individual InAs Nanowires for Environmental Safety

This chapter presented a comprehensive analysis of InAs nanowires in their role as environmental sensors, with a particular focus on detecting RH and NO_2. Our extensive experimentation and analysis have yielded several significant insights into the capabilities and behaviors of these nanowire-based sensing devices.

We have observed that both NWs exhibit remarkable sensitivity to changes in environmental conditions, specifically concentrations of RH and NO_2. This sensitivity is characterized by an increase in resistance in response to higher concentrations of these analytes, demonstrating their potential as effective sensors for environmental monitoring. Interestingly, the study revealed differential response behaviors between the two NWs, particularly noticeable beyond certain concentration thresholds. The observed differences in response can be ascribed to the inherent variations in their physical and chemical characteristics, highlighting the complexity and uniqueness of sensors based on nanowires.

The implications of these findings are far-reaching for the development of nanowire-based sensors in environmental monitoring. The distinct sensitivity and response patterns of the NWs to different analytes suggest the potential to develop a complex of nanowire sensors, each fine-tuned for specific environmental factors.

Future research should explore the synthesis of nanowires with tailored properties to enhance specificity and sensitivity to particular gases. Investigating the long-term stability and durability of InAs NWs under various environmental conditions will be critical. Integrating these sensors into a network for distributed real-time environmental monitoring and developing advanced data analysis algorithms to interpret sensor signals more accurately will be key areas to focus on, particularly in environments with fluctuating conditions and multiple analytes.

Agricultural Enhancement Data Acquisition System for Root Temperature Analysis in Basil Growth

In this chapter, we describe the development of the system to monitor the root zone temperature (RZT) of basil plants in hydroponic cultivation. Integration of precision agriculture techniques, especially incorporation of LoRaWAN technology and advanced sensor systems, was central to this endeavor.

The focus of the system on RZT addressed a significant gap in existing greenhouse monitoring techniques. Furthermore, the implementation of LoRaWAN facilitated efficient and reliable data transmission over long distances within the greenhouse, improving precision agriculture practices.

The design process involved a careful selection of components, including the RZT sensor, autonomous power supply, control system, and wireless interface. This selection resulted in a robust and effective system capable of accurate data collection and transmission. Integration of data transmission to the TTN stack and subsequent linkage to AWS IoT services marked a substantial achievement, providing a platform for advanced data analysis and visualization.

The implications of this monitoring system are multifaceted. Not only can it enhance plant growth through optimal RZT control, it also demonstrates scalability and adaptability for different agricultural contexts. The energy efficient design is aligned with sustainable agriculture practices, focusing on technological contributions to energy conservation. This research advances agricultural technology, particularly in precision agriculture, demonstrating the potential of IoT and sensor technologies in greenhouse environments.

Potential areas for future investigation encompass expanding the application of this system to other crops, conducting long-term field studies, integrating additional environmental sensors, implementing machine learning for data analysis, and conducting an economic analysis for commercial viability. This research paves the way for further innovations in agricultural technology, with significant implications for sustainable and efficient agricultural practices.

Appendix A

Firmware Full Code

Listing A.1: Firmware Code for PEGS Sensors Experiment

```
#include "mbed.h"

// Initializing Timer and Analog Inputs
Timer t;
AnalogIn Sens[6] = {A0, A1, A2, A3, A4, A5};
AnalogIn adc_vref(ADC_VREF);

// Defining variables for sensor values
float Vout[6] = {0.0f};
float Res_PEGS[6] = {0.0f}; // Updated variable name
float Res1[6] = {5.2419f, 5.213f, 5.244f,
5.268f, 5.1879f, 5.067f};
float filter_val[6] = {0.0f};

// Constants and Buffer Initialization
uint16_t Max_res = 0xFFFF;
Serial pc(USBTX, USBRX); // Serial communication setup
const uint8_t iter = 20;
unsigned short buf[6][iter] = {0};
unsigned short max_buf[6], min_buf[6] = {0};
```

```
unsigned int sum_buf[6] = {0};
float pseumed[6] = {0.0f};
float vref = 0.0f;
uint16_t vref12 = 0;

int main() {
    t.start();
    while (1) {
        // Check to perform ADC reading every 10 minutes
        if (!(t.read_ms() % 600000)) {
            // Read and calibrate reference voltage
            vref12 = adc_vref.read_u16() >> 4;
            vref = (3.0f * (*VREFINT_CAL_ADDR) / vref12);

            // Calculate resistance values
            for (u_int8_t ch = 0; ch < 6; ch++) {
                Vout[ch] = (filter_val[ch] / Max_res)
                * vref;
                Res_PEGS[ch] = Res1[ch] * Vout[ch] /
                (vref - Vout[ch]);
            }

            // Print resistance values for debugging
            for (u_int8_t i = 0; i < 6; i++) {
                printf("%f, ", Res_PEGS[i]);
            }
            printf("%f\n", vref);

            // ADC reading and filtering
            for (u_int8_t i = 0; i < 20; i++) {
                for (u_int8_t p = 0; p < 6; p++) {
                    for (u_int8_t j = 0; j < iter; j++) {
```

```
                        buf[p][j] = Sens[p].read_u16();
                        max_buf[p] =
                        max(max_buf[p], buf[p][j]);
                        min_buf[p] =
                        min(min_buf[p], buf[p][j]);
                        sum_buf[p] += buf[p][j];
                        wait_us(100); // Short
                        //delay for ADC stabilization
                    }
                    // Calculate pseudomedian value
                    pseumed[p] = (sum_buf[p] - min_buf[p]
                    - max_buf[p]) / (iter - 2);
                    sum_buf[p] = 0;
                    min_buf[p] = 0;
                    max_buf[p] = 0;
                }

                // Apply low-pass filter to smooth
               // the sensor readings
                for (u_int8_t k = 0; k < 6; k++) {
                    filter_val[k] +=
                    (pseumed[k] - filter_val[k]) * 0.05f;
                }
            }
        }
    }
}
```

Listing A.2: Attiny85 to M24LR64-Y NFC Module Communication

```
#include "M24LR.h"
#include <Wire.h>

M24LR m24lr(0x53);   // Initialize
M24LR with user memory address 0x53.



void setup() {
    char msg[10];
  sprintf(msg,"%hu\r\n",analogRead(A0)); //Send the
  //information  about the voltage on PEGS sensor
  m24lr.NDEF(msg);   // Write NDEF text message.

  m24lr.write_byte(32, 0xA0);   // Write byte to memory.
  delay(50);   // Delay for I2C bus to settle.

  byte data[4] = {0x30, 0x31, 0x32, 0x33};
  m24lr.write_page(7, data, 4); // Write 4 bytes to
  a page in memory.
  delay(50); // Delay for I2C bus to settle.
}

void loop() {
  // EEPROM has limited write endurance. So it is better
  //not to use infinite cycle
}
```

Listing A.3: Arduino code for measuring resistance of nanowires

```
#include "Protocentral_ADS1220.h"
#include <SPI.h>
#include "Seeed_SHT35.h"

// Define pins for different Arduino boards
#ifdef ARDUINO_SAMD_VARIANT_COMPLIANCE
#define SDAPIN 20
#define SCLPIN 21
#define RSTPIN 7
#define SERIAL SerialUSB
#else
#define SDAPIN A4
#define SCLPIN A5
#define SERIAL Serial
#endif

// Constants for temperature measurements
#define TEMP1 2
#define TEMP2 4
#define Rset1 33750
#define Rset2 33780
#define Kgain1 10
#define Kgain2 10

// Variables for storing sensor data
bool flag = 1;
float temp1, hum1;
float temp2, hum2;

// Initialize sensor
SHT35 sensor(SCLPIN);
```

```
// Reference voltage and full scale settings
#define VREF 3.301
#define VFSR VREF
#define R1 402000
#define FULL_SCALE (((long int)1 << 23) - 1)

// Pin assignments for ADS1220
#define ADS1220_CS_PIN 7
#define ADS1220_DRDY_PIN 6

// Create an instance of the ADS1220
Protocentral_ADS1220 pc_ads1220;
int32_t adc_data;
volatile bool drdyIntrFlag = false;

// Function prototypes
float convertToMilliV(int32_t i32data);
int32_t convertToRes1(int32_t i32data, float temp);
int32_t convertToRes2(int32_t i32data, float temp);
float Vres(float temp);

// ADC channels for nanowire measurements
const uint8_t adc_ch[2] = {MUX_SE_CH0, MUX_SE_CH3};
const uint8_t iter = 3;
int32_t buf[2][iter] = {0};
int32_t max_buf[2] = {0};
int32_t min_buf[2] = {FULL_SCALE};
int32_t sum_buf[2] = {0};
int32_t pseumed[2] = {0};
float filter_val[2] = {0.0f};
```

```
// Interrupt handler for data ready signal
void drdyInterruptHndlr() {
    drdyIntrFlag = true;
}

// Setup function for the Arduino
void setup() {
    Serial.begin(9600);

    if (!sensor.init()) {
        SERIAL.println("Sensor initialized successfully.");
    } else {
        SERIAL.println("Sensor initialization failed!");
    }

    pc_ads1220.begin(ADS1220_CS_PIN, ADS1220_DRDY_PIN);
    pc_ads1220.set_data_rate(DR_20SPS);
    pc_ads1220.PGA_OFF();
    pc_ads1220.writeRegister(CONFIG_REG2_ADDRESS, 0xE0);
    // External voltage reference, 50 Hz filtering
    pc_ads1220.set_conv_mode_continuous(); // Continuous
    //conversion mode

    pinMode(TEMP1, OUTPUT);
    pinMode(TEMP2, OUTPUT);
    digitalWrite(TEMP1, flag);
    delay(1000);
}

// Main loop for the Arduino
void loop() {
    if (!(millis() % 5000)) {
```

```
        if (flag) {
            if (NO_ERROR !=
            sensor.read_meas_data_single_shot(
            HIGH_REP_WITH_STRCH, &temp1, &hum1)) {
                SERIAL.println("Reading␣temperature
␣␣␣␣␣␣␣␣␣␣␣␣␣␣␣␣and␣humidity␣failed.");
            }
        }

        SERIAL.print(temp1);
        SERIAL.print(',');
        SERIAL.print(hum1);
        SERIAL.print(',');

        // Reading and processing data from nanowires
        for (int8_t p = 0; p < 2; p++) {
            for (int8_t j = 0; j < 3; j++) {
                buf[p][j] =
                pc_ads1220.
                Read_SingleShot_SingleEnded_WaitForData(
                adc_ch[p]);
                if (max_buf[p] <= buf[p][j])
                    max_buf[p] = buf[p][j];
                if (min_buf[p] >= buf[p][j])
                    min_buf[p] = buf[p][j];
                sum_buf[p] += buf[p][j];
            }

            pseumed[p] = sum_buf[p] - min_buf[p] -
            max_buf[p];
            sum_buf[p] = 0;
            min_buf[p] = FULL_SCALE;
```

```
            max_buf[p] = 0;
        }

        // Print the processed data
        Serial.print(convertToMilliV(pseumed[0]));
        Serial.print(',');
        Serial.print(convertToMilliV(pseumed[1]));
        Serial.print(',');
        Serial.print(convertToRes1(pseumed[0], temp1));
        Serial.print(',');
        Serial.print(convertToRes2(pseumed[1], temp1));
        Serial.println(',');
    }
}

// Function definitions
// Convert ADC value to millivolts
float convertToMilliV(int32_t i32data) {
    return (float)((i32data * VFSR * 1000) / FULL_SCALE);
}

// Calculate current based on temperature for channel 1
double Icur1(float temp) {
    float Vres1(float temp);
    return (Vres1(temp) * 1.071) / Rset1;
}

// Calculate voltage based on temperature for channel 1
float Vres1(float temp) {
    return 0.2105 * temp + 57.945;
}
```

```
// Convert ADC value to resistance for channel 1
int32_t convertToRes1(int32_t i32data, float temp) {
    double Icur1(float temp);
    return (int32_t)((((i32data * VFSR * 1000) /
    FULL_SCALE))/(Icur1(temp) * Kgain1));
}

// Calculate current based on temperature for channel 2
double Icur2(float temp) {
    float Vres2(float temp);
    return (Vres2(temp) * 1.071) / Rset2;
}

// Calculate voltage based on temperature for channel 2
float Vres2(float temp) {
    return 0.1682 * temp + 59.027;
}

// Convert ADC value to resistance for channel 2
int32_t convertToRes2(int32_t i32data, float temp) {
    double Icur2(float temp);
    return (int32_t)((((i32data * VFSR * 1000) /
    FULL_SCALE)) / (Icur2(temp) * Kgain2));
}
```

Listing A.4: Arduino firmware for data acquisition and LoRaWAN transmission.

```
#include <MKRWAN.h>
#include <CayenneLPP.h>
#include <OneWire.h>
#include <DallasTemperature.h>
#include <ArduinoLowPower.h>
#include "arduino_secrets.h"

// OneWire settings
const int oneWirePin = 4;
OneWire oneWire(oneWirePin);
DallasTemperature sensors(&oneWire);

// Device address arrays
DeviceAddress insideThermometer, outsideThermometer;

// Analog pin settings
const int analogPin = A1;
float analogValue;

// LoRaWAN and CayenneLPP
LoRaModem modem;
CayenneLPP lpp(51);
const unsigned long sleepTime = 60000; // Sleep for
1 minute
bool isConnected = false;

void sendData();
void goToSleep();
void alarmEvent();
void reboot();
```

```
void setup() {
  Serial.begin(115200);
  analogReference(AR_DEFAULT);
  analogReadResolution(12);
  LowPower.attachInterruptWakeup(RTC_ALARM_WAKEUP,
  alarmEvent, CHANGE);

  // Address retrieval for temperature sensors
  sensors.begin();
  sensors.setResolution(insideThermometer, 12);
  sensors.setResolution(outsideThermometer, 12);

  // LoRaWAN initialization and connection
  if (!modem.begin(EU868)) {
    Serial.println("Failed to start module");
    delay(1000);
    reboot();
  }
  isConnected = modem.joinOTAA(appEui, appKey);
  modem.minPollInterval(60);
  modem.setADR(true);
  Serial.end();
  USBDevice.detach();
}

void loop() {
  sendData();
  goToSleep();
}

void sendData() {
```

```
  sensors.requestTemperatures();
  float temp1 = sensors.getTempC(insideThermometer);
  float temp2 = sensors.getTempC(outsideThermometer);
  analogValue = float(analogRead(analogPin)) *
  0.00103232064f;

  lpp.reset();
  lpp.addTemperature(1, temp1);
  lpp.addTemperature(2, temp2);
  lpp.addAnalogInput(3, analogValue);

  modem.beginPacket();
  modem.write(lpp.getBuffer(), lpp.getSize());
  int err = modem.endPacket(true);
}

void goToSleep() {
  LowPower.sleep(sleepTime);
}

void alarmEvent() {
  // RTC alarm wake interrupt callback
}

void reboot() {
  NVIC_SystemReset();
  while(1);
}
```

References

[1] E. Musaev, M. Soprani, E. Sardini, C. de Angelis, E. Cantu, M. Serpelloni, and C. Baratto, “Development of the data acquisition system for sensing food spoilage,” in *Modelling and Characterization of Novel Functional Materials for Green Energy, Sensing, and Catalysis Applications.* Warsaw, Poland: European Materials Research Society (E-MRS), 2022, presented at the European Materials Research Society (E-MRS) Spring Meeting, Session on Modelling and Characterization of Novel Functional Materials for Green Energy, Sensing, and Catalysis Applications. (Cited on page xv.)

[2] E. Musaev, V. Demontis, F. Rossella, V. Zannier, L. Sorba, and C. Baratto, “Comparative analysis of inas adjacent nanowire sensors for humidity and no2 detection,” in *2023 IEEE Nanotechnology Materials and Devices Conference (NMDC)*, 2023, pp. 461–462. (Cited on page xvi.)

[3] M. Anas, F. Liao, K. K. Verma, M. A. Sarwar, A. Mahmood, Z.-L. Chen, Q. Li, X.-P. Zeng, Y. Liu, and Y.-R. Li, “Fate of nitrogen in agriculture and environment: agronomic, eco-physiological and molecular approaches to improve nitrogen use efficiency,” *Biological Research*, vol. 53, no. 1, p. 47, 12 2020. (Cited on page 2.)

[4] A. Barros-Rodríguez, P. Rangseekaew, K. Lasudee, W. Pathom-aree, and M. Manzanera, “Impacts of Agriculture on the Environment and Soil Microbial Biodiversity,” *Plants*, vol. 10, no. 11, p. 2325, 10 2021. (Cited on page 2.)

[5] G. A. Duncan, R. Gates, and M. D. Montross, “Measuring relative humidity in agricultural environments,” *Agricultural Engineering Extension*

Publications-Uknowledge, 2005. (Cited on page 2.)

[6] P. Zhang, J. Zhang, and M. Chen, "Economic impacts of climate change on agriculture: The importance of additional climatic variables other than temperature and precipitation," *Journal of Environmental Economics and Management*, vol. 83, pp. 8–31, 5 2017. (Cited on page 2.)

[7] J. Wei, "Distributed capacitance of planar electrodes in optic and acoustic surface wave devices," *IEEE Journal of Quantum Electronics*, vol. 13, no. 4, pp. 152–158, 1977. (Cited on pages 2, 9, and 12.)

[8] G. Barandun, M. Soprani, S. Naficy, M. Grell, M. Kasimatis, K. L. Chiu, A. Ponzoni, and F. Güder, "Cellulose Fibers Enable Near-Zero-Cost Electrical Sensing of Water-Soluble Gases," *ACS Sensors*, vol. 4, no. 6, pp. 1662–1669, 6 2019. (Cited on pages 2, 10, and 18.)

[9] A. Shruti, N. Bage, and P. Kar, "Nanomaterials based sensors for analysis of food safety," *Food Chemistry*, vol. 433, p. 137284, 2 2024. (Cited on pages 6 and 7.)

[10] H. Zhang, X. Wei, M. B. Chan-Park, and M. Wang, "Colorimetric Sensors Based on Multifunctional Polymers for Highly Sensitive Detection of Food Spoilage," *ACS Food Science & Technology*, vol. 2, no. 4, pp. 703–711, 4 2022. (Cited on pages 6 and 7.)

[11] X. Jia, P. Ma, K. Tarwa, and Q. Wang, "Machine vision-based colorimetric sensor systems for food applications," *Journal of Agriculture and Food Research*, vol. 11, p. 100503, 3 2023. (Cited on pages 6 and 7.)

[12] G. Liu, M. Lu, X. Huang, T. Li, and D. Xu, "Application of Gold-Nanoparticle Colorimetric Sensing to Rapid Food Safety Screening," *Sensors*, vol. 18, no. 12, p. 4166, 11 2018. (Cited on pages 6, 7, and 42.)

[13] S. Wang, X. Liu, M. Yang, Y. Zhang, K. Xiang, and R. Tang, "Review of Time Temperature Indicators as Quality Monitors in Food Packaging," *Packaging Technology and Science*, vol. 28, no. 10, pp. 839–867, 10 2015. (Cited on pages 6 and 7.)

[14] P. Müller and M. Schmid, "Intelligent Packaging in the Food Sector: A Brief Overview," *Foods*, vol. 8, no. 1, p. 16, 1 2019. (Cited on pages 6, 7, and 8.)

[15] V. Adiani, S. Gupta, and P. S. Variyar, "A simple time temperature indicator for real time microbial assessment in minimally processed fruits," *Journal of Food Engineering*, vol. 311, p. 110731, 12 2021. (Cited on pages 6 and 7.)

[16] R. V. Saini, P. Vaid, N. K. Saini, S. S. Siwal, V. K. Gupta, V. K. Thakur, and A. K. Saini, "Recent Advancements in the Technologies Detecting Food Spoiling Agents," *Journal of Functional Biomaterials*, vol. 12, no. 4, p. 67, 11 2021. (Cited on pages 6 and 8.)

[17] F. Mustafa and S. Andreescu, "Chemical and Biological Sensors for Food-Quality Monitoring and Smart Packaging," *Foods*, vol. 7, no. 10, p. 168, 10 2018. (Cited on pages 6 and 8.)

[18] E. Istif, H. Mirzajani, Ç. Dağ, F. Mirlou, E. Y. Ozuaciksoz, C. Cakır, H. C. Koydemir, I. Yilgor, E. Yilgor, and L. Beker, "Miniaturized wireless sensor enables real-time monitoring of food spoilage," *Nature Food*, vol. 4, no. 5, pp. 427–436, 5 2023. (Cited on pages 6 and 8.)

[19] S. Matindoust, G. Farzi, M. B. Nejad, and M. H. Shahrokhabadi, "Polymer-based gas sensors to detect meat spoilage: A review," *Reactive and Functional Polymers*, vol. 165, p. 104962, 8 2021. (Cited on pages 6 and 8.)

[20] T. Pavase, H. Lin, Q. ul-ain Shaikh, S. Hussain, Z. Li, I. Ahmed, L. Lv, L. Sun, S. B. H. Shah, and M. T. Kalhoro, "Recent advances of conjugated polymer (cp) nanocomposite-based chemical sensors and their applications in food spoilage detection: A comprehensive review," *Sensors and Actuators B: Chemical*, 2018. (Cited on page 6.)

[21] E. Cantù, M. Soprani, A. Ponzoni, E. Sardini, and M. Serpelloni, "Preliminary Analysis on Cellulose-based Gas Sensor by Means of Aerosol Jet Printing and Photonic Sintering," in *Proceedings of the 13th International Joint Conference on Biomedical Engineering Systems and Technologies*. SCITEPRESS - Science and Technology Publications, 2020, pp. 200–206. (Cited on pages 8 and 19.)

[22] M. Borghetti, E. Cantu, A. Ponzoni, E. Sardini, and M. Serpelloni, "Aerosol Jet Printed and Photonic Cured Paper-Based Ammonia Sensor for Food Smart Packaging," *IEEE Transactions on Instrumentation and Measurement*, vol. 71, pp. 1–10, 2022. (Cited on pages 8 and 19.)

[23] C. L. Sciences. Grade 1 chr cellulose chromatography papers. Available online: https://www.cytivalifesciences.com/en/us/shop/lab-filtration/cellulose-filter-papers/chromatography-papers/grade-1-chr-cellulose-chromatography-papers-p-04830 (accessed on 17 October 2023). (Cited on pages 8 and 19.)

[24] L. Gegeckienė, I. Venytė, J. Karpavičė, T. Tambo, K. Vaitasius, and D. Pauliukaitis, "Near field communication (nfc) technology in the packaging industry," in *GRID 2022: 11th international symposium on graphic engineering and design, Novi Sad, 3-5 November 2022: proceedings.* University of Novi Sad, 2022, pp. 495–501. (Cited on pages 9 and 33.)

[25] S. C. Mukhopadhyay, B. George, J. K. Roy, and T. Islam, Eds., *Interdigital Sensors.* Cham: Springer International Publishing, 2021, vol. 36. (Cited on page 10.)

[26] N. Afsarimanesh, A. Nag, M. E. E. Alahi, T. Han, and S. C. Mukhopadhyay, "Interdigital sensors: Biomedical, environmental and industrial applications," *Sensors and Actuators A: Physical*, vol. 305, p. 111923, 4 2020. (Cited on page 10.)

[27] G. Alcantara and C. Andrade, "A short review of gas sensors based on interdigital electrode," in *2015 12th IEEE International Conference on Electronic Measurement & Instruments (ICEMI).* IEEE, 7 2015, pp. 1616–1621. (Cited on page 10.)

[28] R. Igreja and C. J. Dias, "Analytical evaluation of the interdigital electrodes capacitance for a multi-layered structure," *Sensors and Actuators, A: Physical*, vol. 112, no. 2-3, pp. 291–301, 5 2004. (Cited on pages 10, 11, and 12.)

[29] S. Boutros and A. A. Hanna, "Dielectric properties of moist cellulose," *Journal of Polymer Science: Polymer Chemistry Edition*, vol. 16, no. 1, pp.

89–94, 1978. [Online]. Available: https://onlinelibrary.wiley.com/doi/abs/10.1002/pol.1978.170160109 (Cited on page 13.)

[30] W. Olthuis, W. Streekstra, and P. Bergveld, "Theoretical and experimental determination of cell constants of planar-interdigitated electrolyte conductivity sensors," *Sensors and Actuators B: Chemical*, vol. 24, no. 1-3, pp. 252–256, 3 1995. (Cited on page 15.)

[31] H. Engan, "Excitation of elastic surface waves by spatial harmonics of interdigital transducers," *IEEE Transactions on Electron Devices*, vol. 16, no. 12, pp. 1014–1017, 12 1969. (Cited on page 15.)

[32] Y. Lu, W. Shi, J. Qin, and B. Lin, "Fabrication and Characterization of Paper-Based Microfluidics Prepared in Nitrocellulose Membrane By Wax Printing," *Analytical Chemistry*, vol. 82, no. 1, pp. 329–335, 1 2010. (Cited on page 18.)

[33] W. Dungchai, O. Chailapakul, and C. S. Henry, "Use of multiple colorimetric indicators for paper-based microfluidic devices," *Analytica Chimica Acta*, vol. 674, no. 2, pp. 227–233, 8 2010. (Cited on page 18.)

[34] D. A. Bruzewicz, M. Reches, and G. M. Whitesides, "Low-Cost Printing of Poly(dimethylsiloxane) Barriers To Define Microchannels in Paper," *Analytical Chemistry*, vol. 80, no. 9, pp. 3387–3392, 5 2008. (Cited on page 18.)

[35] H. Kirkham, "Current measurement methods for the smart grid," in *2009 IEEE Power & Energy Society General Meeting.* IEEE, 7 2009, pp. 1–7. (Cited on page 19.)

[36] K. Hoffmann, *Applying the wheatstone bridge circuit.* HBM Darmstadt, Germany, 1974. (Cited on page 19.)

[37] B. E. Boser and B. A. Wooley, "The design of sigma-delta modulation analog-to-digital converters," *IEEE Journal of solid-state circuits*, vol. 23, no. 6, pp. 1298–1308, 1988. (Cited on page 20.)

[38] R. Lent, "A sensor network to profile the electrical power consumption of computer networks," in *2010 IEEE Globecom Workshops*. IEEE, 2010, pp. 1433–1437. (Cited on page 21.)

[39] A. Baskys, "The course of microcontrollers oriented to practical skills," *Solid State Phenomena*, vol. 165, pp. 410–413, 2010. (Cited on page 21.)

[40] S. F. Barrett, *Embedded Systems Design with the Atmel AVR Microcontroller*. Morgan & Claypool Publishers, 2010. (Cited on page 21.)

[41] STM32. Stm32 32-bit arm cortex mcus. Available online: https://www.st.com/en/microcontrollers-microprocessors/stm32-32-bit-arm-cortex-mcus.html (accessed on 17 October 2023). (Cited on pages 21 and 22.)

[42] STM32. Stm32 ultra low power mcus. Available online: https://www.st.com/en/microcontrollers-microprocessors/stm32-ultra-low-power-mcus.html (accessed on 17 October 2023). (Cited on page 22.)

[43] STM32. Stm32 software development tools. Available online: https://www.st.com/en/development-tools/stm32-software-development-tools.html (accessed on 17 October 2023). (Cited on page 22.)

[44] Analog devices. Precision, 20 mhz, cmos, rail-to-rail input/output operational amplifiers. Available online: https://www.analog.com/media/en/technical-documentation/data-sheets/AD8615_8616_8618.pdf (accessed on 17 October 2023). (Cited on page 22.)

[45] STM32. Stm32 nucleo-64 development board with stm32l053r8 mcu, supports arduino and st morpho connectivity. Available online: https://www.st.com/en/evaluation-tools/nucleo-l053r8.html (accessed on 17 October 2023). (Cited on page 24.)

[46] STM32. Nfc card reader expansion board based on cr95hf/st25r95 for stm32 nucleo. Available online: https://www.st.com/en/ecosystems/x-nucleo-nfc03a1.html (accessed on 17 October 2023). (Cited on page 24.)

[47] Sensirion. ±2% digital humidity and temperature sensor. Available online: https://sensirion.com/products/catalog/SHT33-DIS/ (accessed on 17 October 2023). (Cited on page 25.)

[48] I. C. on Microbiological Specifications for Foods, Ed., *Sampling Plans for Fish and Shellfish*, 2nd ed. Toronto: University of Toronto Press, 1986, pp. 181–196. (Cited on page 31.)

[49] C. A. Schneider, W. S. Rasband, and K. W. Eliceiri, "Nih image to imagej: 25 years of image analysis," *Nature Methods*, vol. 9, no. 7, pp. 671–675, 2012. (Cited on page 31.)

[50] X. Zhang, X. Shan, and J. Wei, "Hybrid flexible smart temperature tag with nfc technology for smart packaging," in *2017 IEEE 19th Electronics Packaging Technology Conference (EPTC)*. IEEE, 2017, pp. 1–5. (Cited on page 33.)

[51] P. Escobedo, M. Bhattacharjee, F. Nikbakhtnasrabadi, and R. Dahiya, "Flexible strain sensor with nfc tag for food packaging," in *2020 IEEE international conference on Flexible and Printable Sensors and Systems (FLEPS)*. IEEE, 2020, pp. 1–4. (Cited on page 33.)

[52] D. Brunelli, C. Moser, L. Thiele, and L. Benini, "Design of a solar-harvesting circuit for batteryless embedded systems," *IEEE Transactions on Circuits and Systems I: Regular Papers*, vol. 56, no. 11, pp. 2519–2528, 2009. (Cited on page 33.)

[53] A. Gomez, A. Tretter, P. A. Hager, P. Sanmugarajah, L. Benini, and L. Thiele, "Dataflow driven partitioning of machine learning applications for optimal energy use in batteryless systems," *ACM Transactions on Embedded Computing Systems*, vol. 21, no. 5, pp. 1–29, 2022. (Cited on page 33.)

[54] G. T. Le, T. V. Tran, H.-S. Lee, and W.-Y. Chung, "Long-range batteryless rf sensor for monitoring the freshness of packaged vegetables," *Sensors and Actuators A: Physical*, vol. 237, pp. 20–28, 2016. (Cited on page 33.)

[55] STM32. Dynamic nfc tag expansion board based on m24sr for stm32 nucleo. Available online: https://www.st.com/en/ecosystems/x-nucleo-nfc01a1.html (accessed on 17 October 2023). (Cited on page 34.)

[56] J. Du, D. Liang, H. Tang, and X. P. Gao, "InAs Nanowire Transistors as Gas Sensor and the Response Mechanism," *Nano Letters*, vol. 9, no. 12, pp. 4348–4351, 12 2009. (Cited on pages 38 and 40.)

[57] Y. Zhao, W. Zhang, B. Yang, J. Liu, X. Chen, X. Wang, and C. Yang, "Gas-sensing enhancement methods for hydrothermal synthesized sno2-based sensors," *Nanotechnology*, vol. 28, no. 45, p. 452002, 2017. (Cited on page 39.)

[58] X.-T. Yin, W.-D. Zhou, J. Li, Q. Wang, F.-Y. Wu, D. Dastan, D. Wang, H. Garmestani, X.-M. Wang, and Ştefan Ţălu, "A highly sensitivity and selectivity pt-sno2 nanoparticles for sensing applications at extremely low level hydrogen gas detection," *Journal of Alloys and Compounds*, vol. 805, pp. 229–236, 2019. [Online]. Available: https://www.sciencedirect.com/science/article/pii/S0925838819325782 (Cited on page 40.)

[59] E. Pickering, A. Bo, H. Zhan, X. Liao, H. H. Tan, and Y. Gu, "In situ mechanical resonance behaviour of pristine and defective zinc blende gaas nanowires," *Nanoscale*, vol. 10, no. 5, pp. 2588–2595, 2018. (Cited on page 40.)

[60] Y. Xie, P. Wan, M. Jiang, Y. Liu, D. Shi, and C. Kan, "Performance enhancement of a self-biased n-zno microwire/p-gan heterojunction ultraviolet photodetector incorporating ag nanowires," *CrystEngComm*, vol. 24, no. 44, pp. 7727–7738, 2022. (Cited on page 40.)

[61] D. Ciuculescu, F. Dumestre, M. Comesana-Hermo, B. Chaudret, M. Spasova, M. Farle, and C. Amiens, "Single-crystalline co nanowires: synthesis, thermal stability, and carbon coating," *Chemistry of Materials*, vol. 21, no. 17, pp. 3987–3995, 2009. (Cited on page 40.)

[62] C. Baratto, V. Golovanova, G. Faglia, H. Hakola, T. Niemi, N. Tkachenko, B. Nazarchurk, and V. Golovanov, “On the alignment of ZnO nanowires by Langmuir – Blodgett technique for sensing application,” *Applied Surface Science*, vol. 528, p. 146959, 10 2020. (Cited on pages 40 and 58.)

[63] E. Comini, C. Baratto, G. Faglia, M. Ferroni, A. Vomiero, and G. Sberveglieri, “Quasi-one dimensional metal oxide semiconductors: Preparation, characterization and application as chemical sensors,” *Progress in Materials Science*, vol. 54, no. 1, pp. 1–67, 1 2009. (Cited on page 40.)

[64] C. Baratto, “Growth and properties of ZnO nanorods by RF-sputtering for detection of toxic gases,” *RSC Advances*, vol. 8, no. 56, pp. 32 038–32 043, 2018. (Cited on pages 40 and 58.)

[65] N. Bârsan, “Transduction in Semiconducting Metal Oxide Based Gas Sensors - Implications of the Conduction Mechanism,” *Procedia Engineering*, vol. 25, pp. 100–103, 2011. (Cited on page 40.)

[66] Y. Zhang, A. Kolmakov, S. Chretien, H. Metiu, and M. Moskovits, “Control of Catalytic Reactions at the Surface of a Metal Oxide Nanowire by Manipulating Electron Density Inside It,” *Nano Letters*, vol. 4, no. 3, pp. 403–407, 3 2004. (Cited on page 40.)

[67] M. Donarelli, M. Ferroni, A. Ponzoni, F. Rigoni, D. Zappa, C. Baratto, G. Faglia, E. Comini, and G. Sberveglieri, “Single Metal Oxide Nanowire devices for Ammonia and Other Gases Detection in Humid Atmosphere,” *Procedia Engineering*, vol. 168, pp. 1052–1055, 2016. (Cited on page 40.)

[68] A. Kolmakov, “Some recent trends in the fabrication, functionalisation and characterisation of metal oxide nanowire gas sensors,” *International Journal of Nanotechnology*, vol. 5, no. 4/5, p. 450, 2008. (Cited on page 40.)

[69] F. Hernández-Ramírez, A. Tarancón, O. Casals, J. Arbiol, A. Romano-Rodríguez, and J. R. Morante, “High response and stability in CO and humidity measures using a single SnO2 nanowire,” *Sensors and Actuators B: Chemical*, vol. 121, no. 1, pp. 3–17, 2007. [Online]. Available: https:

//www.sciencedirect.com/science/article/pii/S0925400506006198 (Cited on page 40.)

[70] G. Meng, F. Zhuge, K. Nagashima, A. Nakao, M. Kanai, Y. He, M. Boudot, T. Takahashi, K. Uchida, and T. Yanagida, "Nanoscale Thermal Management of Single SnO_2 Nanowire: pico-Joule Energy Consumed Molecule Sensor," *ACS Sensors*, vol. 1, no. 8, pp. 997–1002, 8 2016. (Cited on page 40.)

[71] D. Zhang, Z. Liu, C. Li, T. Tang, X. Liu, S. Han, B. Lei, and C. Zhou, "Detection of NO_2 down to ppb Levels Using Individual and Multiple In_2O_3 Nanowire Devices," *Nano Letters*, vol. 4, no. 10, pp. 1919–1924, 10 2004. (Cited on page 40.)

[72] C. Baratto, R. Kumar, G. Faglia, K. Vojisavljević, and B. Malič, "p-Type copper aluminum oxide thin films for gas-sensing applications," *Sensors and Actuators B: Chemical*, vol. 209, pp. 287–296, 3 2015. (Cited on page 40.)

[73] D. Lynall, A. C. Tseng, S. V. Nair, I. G. Savelyev, M. Blumin, S. Wang, Z. M. Wang, and H. E. Ruda, "Nonlinear Chemical Sensitivity Enhancement of Nanowires in the Ultralow Concentration Regime," *ACS Nano*, vol. 14, no. 1, pp. 964–973, 1 2020. (Cited on page 40.)

[74] P. Offermans, M. Crego-Calama, and S. H. Brongersma, "Gas Detection with Vertical InAs Nanowire Arrays," *Nano Letters*, vol. 10, no. 7, pp. 2412–2415, 7 2010. (Cited on page 40.)

[75] X. Zhang, M. Fu, X. Li, T. Shi, Z. Ning, X. Wang, T. Yang, and Q. Chen, "Study on the response of InAs nanowire transistors to H2O and NO2," *Sensors and Actuators B: Chemical*, vol. 209, pp. 456–461, 3 2015. (Cited on page 40.)

[76] A. R. Ullah, H. J. Joyce, H. H. Tan, C. Jagadish, and A. P. Micolich, "The influence of atmosphere on the performance of pure-phase WZ and ZB InAs nanowire transistors," *Nanotechnology*, vol. 28, no. 45, p. 454001, 11 2017. (Cited on page 40.)

[77] Y. Zhou, Y. Wang, Y. Wang, X. Li, and Y. Guo, “The impact of carrier gas on room-temperature trace nitrogen dioxide sensing of ZnO nanowire-integrated film under UV illumination,” *Ceramics International*, vol. 46, no. 10, pp. 16 056–16 061, 7 2020. (Cited on page 40.)

[78] V. Demontis, M. Rocci, M. Donarelli, R. Maiti, V. Zannier, F. Beltram, L. Sorba, S. Roddaro, F. Rossella, and C. Baratto, “Conductometric Sensing with Individual InAs Nanowires,” *Sensors*, vol. 19, no. 13, p. 2994, 7 2019. (Cited on pages 40 and 45.)

[79] F. Floris, L. Fornasari, A. Marini, V. Bellani, F. Banfi, S. Roddaro, D. Ercolani, M. Rocci, F. Beltram, M. Cecchini *et al.*, “Self-assembled inas nanowires as optical reflectors,” *Nanomaterials*, vol. 7, no. 11, p. 400, 2017. (Cited on page 41.)

[80] D. Kriegner, C. Panse, B. Mandl, K. A. Dick, M. Keplinger, J. M. Persson, P. Caroff, D. Ercolani, L. Sorba, F. Bechstedt, J. Stangl, and G. Bauer, “Unit cell structure of crystal polytypes in inas and insb nanowires,” *Nano Letters*, vol. 11, no. 4, pp. 1483–1489, 2011, pMID: 21434674. (Cited on page 41.)

[81] C. Thelander, K. A. Dick, M. Borgström, L. E. Fröberg, P. Caroff, H. Nilsson, and L. Samuelson, “The electrical and structural properties of n-type inas nanowires grown from metal–organic precursors,” *Nanotechnology*, vol. 21, no. 20, p. 205703, 2010. (Cited on pages 41 and 42.)

[82] A. Davydok, S. Breuer, A. Biermanns, L. Geelhaar, and U. Pietsch, “Lattice parameter accommodation between gaas (111) nanowires and si (111) substrate after growth via au-assisted molecular beam epitaxy,” *Nanoscale research letters*, vol. 7, pp. 1–7, 2012. (Cited on page 42.)

[83] J. Lieb, V. Demontis, D. Prete, D. Ercolani, V. Zannier, L. Sorba, S. Ono, F. Beltram, B. Sacépé, and F. Rossella, “Ionic-Liquid Gating of InAs Nanowire-Based Field-Effect Transistors,” *Advanced Functional Materials*, vol. 29, no. 3, p. 1804378, 1 2019. (Cited on page 42.)

[84] L. E. Jensen, M. T. Björk, S. Jeppesen, A. I. Persson, B. J. Ohlsson, and L. Samuelson, "Role of surface diffusion in chemical beam epitaxy of inas nanowires," *Nano Letters*, vol. 4, no. 10, pp. 1961–1964, 2004. (Cited on page 43.)

[85] D. B. Suyatin, C. Thelander, M. T. Björk, I. Maximov, and L. Samuelson, "Sulfur passivation for ohmic contact formation to inas nanowires," *Nanotechnology*, vol. 18, no. 10, p. 105307, feb 2007. [Online]. Available: https://dx.doi.org/10.1088/0957-4484/18/10/105307 (Cited on page 43.)

[86] X. Chen, R. Li, K. Qi, and G.-Q. Lu, "Tensile behaviors and ratcheting effects of partially sintered chip-attachment films of a nanoscale silver paste," *Journal of Electronic Materials*, vol. 37, pp. 1574–1579, 2008. (Cited on pages 43 and 44.)

[87] Y. Cheng, J. Zhang, C. Fang, W. Qiu, H. Chen, H. Liu, and Y. Wei, "Preparation of low volatile organic compounds silver paste containing ternary conductive fillers and optimization of their performances," *Molecules*, vol. 27, no. 22, 2022. [Online]. Available: https://www.mdpi.com/1420-3049/27/22/8030 (Cited on page 44.)

[88] C. Zhang, M. Neklyudova, L. Fang, Q. Xu, H. Wang, F. D. Tichelaar, and H. W. Zandbergen, "In situ electrical characterization of tapered inas nanowires in a transmission electron microscope with ohmic contacts," *Nanotechnology*, vol. 26, no. 15, p. 155703, mar 2015. [Online]. Available: https://dx.doi.org/10.1088/0957-4484/26/15/155703 (Cited on pages 45 and 46.)

[89] J. D. Prades, R. Jimenez-Diaz, F. Hernandez-Ramirez, S. Barth, A. Cirera, A. Romano-Rodriguez, S. Mathur, and J. R. Morante, "Ultralow power consumption gas sensors based on self-heated individual nanowires," *Applied Physics Letters*, vol. 93, no. 12, 9 2008. (Cited on page 47.)

[90] K. Chikkadi, M. Muoth, V. Maiwald, C. Roman, and C. Hierold, "Ultra-low power operation of self-heated, suspended carbon nanotube gas sensors," *Applied Physics Letters*, vol. 103, no. 22, 11 2013. (Cited on page 47.)

[91] Available online: https://www.ti.com/lit/ds/symlink/lm334.pdf (accessed on 17 October 2023). (Cited on pages 47 and 49.)

[92] Available online: https://www.analog.com/media/en/technical-documentation/data-sheets/AD8655_8656.pdf (accessed on 17 October 2023). (Cited on page 47.)

[93] Available online: https://www.ti.com/lit/ds/symlink/ads1220.pdf (accessed on 17 October 2023). (Cited on page 47.)

[94] Available online: https://docs.arduino.cc/hardware/uno-rev3 (accessed on 17 October 2023). (Cited on page 47.)

[95] Available online: https://sensirion.com/media/documents/051DF50B/639C8101/Sensirion_Humidity_and_Temperature_Sensors_Datasheet_SHT33.pdf (accessed on 17 October 2023). (Cited on page 47.)

[96] M. El Ghoumari, H.-J. Tantau, and J. Serrano, "Non-linear constrained mpc: Real-time implementation of greenhouse air temperature control," *Computers and electronics in agriculture*, vol. 49, no. 3, pp. 345–356, 2005. (Cited on page 62.)

[97] P. M. Ferreira, E. Faria, and A. Ruano, "Neural network models in greenhouse air temperature prediction," *Neurocomputing*, vol. 43, no. 1-4, pp. 51–75, 2002. (Cited on page 62.)

[98] A. Grunwald, M. Schaarschmidt, and C. Westerkamp, "Lorawan in a rural context: Use cases and opportunities for agricultural businesses," in *Mobile Communication - Technologies and Applications; 24. ITG-Symposium*, 2019, pp. 1–6. (Cited on page 62.)

[99] A. B. Schreck. The Application of LoRaWAN as an Internet of Things Tool to Promote Data Collection in Agriculture. [Online]. Available: https://hammer.purdue.edu/articles/thesis/The_Application_of_LoRaWAN_as_an_Internet_of_Things_Tool_to_Promote_Data_Collection_in_Agriculture/22693036 (Cited on page 62.)

[100] A. Van Der Zanden, "Environmental factors affecting plant growth," *Oregon State University: Corvallis, OR, USA*, 2008. (Cited on page 63.)

[101] Y. Kawasaki, S. Matsuo, Y. Kanayama, and K. Kanahama, "Effect of root-zone heating on root growth and activity, nutrient uptake, and fruit yield of tomato at low air temperatures," *Journal of the Japanese Society for Horticultural Science*, vol. 83, no. 4, pp. 295–301, 2014. (Cited on page 63.)

[102] J. Moorby and C. Graves, "Root and air temperature effects on growth and yield of tomatoes and lettuce," in *Symposium on Research on Recirculating Water Culture 98*, 1979, pp. 29–44. (Cited on page 63.)

[103] Q. Yan, Z. Duan, J. Mao, X. Li, and F. Dong, "Effects of root-zone temperature and n, p, and k supplies on nutrient uptake of cucumber (cucumis sativus l.) seedlings in hydroponics," *Soil Science and Plant Nutrition*, vol. 58, no. 6, pp. 707–717, 2012. (Cited on page 63.)

[104] R. Wang, M. Isozaki, Y. Iwasaki, and Y. Muramatsu, "Root-zone temperature effects on spinach biomass production using a nutrient film technique system," *HortScience*, vol. 57, no. 4, pp. 532 – 540, 2022. [Online]. Available: https://journals.ashs.org/hortsci/view/journals/hortsci/57/4/article-p532.xml (Cited on page 63.)

[105] C. Currey, "Managing basil production throughout the year," *Produce Grower*, 2020. [Online]. Available: https://www.producegrower.com/article/hydroponic-production-primer-managing-basilproduction-throughout-the-year (Cited on page 63.)

[106] G. Raimondi, F. Orsini, A. Maggio, S. De Pascale, and G. Barbieri, "Yield and quality of hydroponically grown sweet basil cultivars," in *Acta Horticulturae*, vol. 723. International Society for Horticultural Science (ISHS), Leuven, Belgium, 2006, pp. 357–360. [Online]. Available: https://doi.org/10.17660/ActaHortic.2006.723.48 (Cited on page 63.)

[107] T. Hendrickson, B. L. Dunn, C. Goad, B. Hu, and H. Singh, "Effects of elevated water temperature on growth of basil using nutrient film

technique," *HortScience*, vol. 57, no. 8, pp. 925 – 932, 2022. [Online]. Available: https://journals.ashs.org/hortsci/view/journals/hortsci/57/8/article-p925.xml (Cited on page 63.)

[108] A. Shrestha and B. Dunn, "Hydroponics," Oklahoma Cooperative Extension Service, Tech. Rep., 2010. (Cited on page 63.)

[109] P. Sambo, C. Nicoletto, A. Giro, Y. Pii, F. Valentinuzzi, T. Mimmo, P. Lugli, G. Orzes, F. Mazzetto, S. Astolfi, R. Terzano, and S. Cesco, "Hydroponic solutions for soilless production systems: Issues and opportunities in a smart agriculture perspective," *Frontiers in Plant Science*, vol. 10, 2019. [Online]. Available: https://www.frontiersin.org/articles/10.3389/fpls.2019.00923 (Cited on page 63.)

[110] H. Lee. (2019) Advantages and disadvantages of using thermocouples. [Online]. Available: https://sciencing.com/advantages-disadvantages-using-thermocouples-6153729.html (Cited on page 65.)

[111] H. Soffar. (2017) Infrared thermometers (ir thermometers) features, types, cons and pros. [Online]. Available: https://www.online-sciences.com/technology/infrared-thermometers-ir-thermometers-features-types-cons-and-pros/ (Cited on page 65.)

[112] I. Lamprecht, E. Schmolz, L. Blanco, and C. Romero, "Flower ovens: thermal investigations on heat producing plants," *Thermochimica Acta*, vol. 391, no. 1, pp. 107–118, 2002, calorimetry and More. A Collection of Invited Papers in Honor of Gunther W.H. Hohne and Michael J. Richardson. [Online]. Available: https://www.sciencedirect.com/science/article/pii/S0040603102001685 (Cited on page 65.)

[113] Programmable resolution 1-wire digital thermometer. [Online]. Available: https://www.analog.com/media/en/technical-documentation/data-sheets/ds18b20.pdf (Cited on pages 65, 67, and 68.)

[114] Redway Battery. (2023) The comprehensive guide to 18650 rechargeable batteries. Accessed: November 17, 2023. [Online]. Available: https://www.redwaybattery.com/empowering-devices-with-lithium-

ion-batteries-a-comprehensive-guide-to-18650-rechargeables/ (Cited on pages 67 and 68.)

[115] Arduino. (2023) Mkr wan 1310. Accessed: November 17, 2023. [Online]. Available: https://docs.arduino.cc/hardware/mkr-wan-1310 (Cited on pages 67 and 68.)

[116] T. Stack. (2023) The cayennelpp class description. [Online]. Available: https://www.thethingsnetwork.org/docs/devices/arduino/api/cayennelpp/ (Cited on page 72.)

MODULO DI EMBARGO DELLA TESI
(da compilare solo se si richiede un periodo di segretazione della tesi)

Il/La sottoscritto/a………Egit Musaev…………………………… Nato/a il…10/12/1991…………
a (indicare anche l'eventuale paese estero)……………Federazione Russa………………………………..
provincia di (ovvero sigla del paese estero)…RU………………………………………………….
Dottorato di Ricerca in … Ingegneria dell'informazione…………………………………….
…………………………………………………………..…………………………………………

DICHIARA

- che il contenuto della tesi **non può essere immediatamente consultabile per il seguente motivo**

Sottomissione di un articolo in collaborazione con altri ricercatori in corso.
La motivazione deve essere dettagliata e controfirmata obbligatoriamente dal Primo Supervisore di tesi
(Brevetto, segreto industriale, motivi di priorità nella ricerca, motivi editoriali, altro)

- che il testo completo della tesi potrà essere reso consultabile dopo:

x 6 mesi dalla data di conseguimento titolo

- che sarà comunque consultabile immediatamente l'abstract della tesi, che viene caricato in Esse3, profilo studente.

Luogo e Data

Brescia , 16/02/2024

Firma del Dichiarante

Controfirma del Primo Supervisore di tesi
per la motivazione di embargo e il periodo.

Camilla Baratto